Master's Thesis
Astrophysical Sciences

The Final Parsec Problem in Massive Early-Type Galaxies

Alexander Rawlings

January 8, 2021

Supervisors: Prof. Peter H. Johansson
M.Sc. Matias Mannerkoski

Censors: Prof. Peter H. Johansson
Dr. Shihong Liao

UNIVERSITY OF HELSINKI
Particle Physics and Astrophysical Sciences

PL. 64 (Gustaf Hällströmin katu 2)
FI-00014 University of Helsinki
Finland

“Home is behind, the world ahead.”
—J.R.R. Tolkien

HELSINGIN YLIOPISTO — HELSINGFORS UNIVERSITET — UNIVERSITY OF HELSINKI

Tiedekunta — Fakultet — Faculty	Koulutusohjelma — Utbildningsprogram — Education programme
Faculty of Science	Particle Physics and Astrophysical Sciences

Tekijä — Författare — Author
Alexander Rawlings

Työn nimi — Arbetets titel — Title

The Final Parsec Problem in Massive Early-Type Galaxies

Opintosuunta — Studieinriktning — Study track
Astrophysical Sciences

Työn laji — Arbetets art — Level	Aika — Datum — Month and year	Sivumäärä — Sidoantal — Number of pages
Master's Thesis	January 8, 2021	116 pages

Tiivistelmä — Referat — Abstract

This thesis presents the results from seventeen collisionless merger simulations of massive early-type galaxies in an effort to understand the coalescence of supermassive black holes (SMBHs) in the context of the Final Parsec Problem. A review of the properties of massive early-type galaxies and their SMBHs is presented alongside a discussion on SMBH binary coalescence to motivate the initial conditions used in the simulations. The effects of varying SMBH mass and stellar density profiles in the progenitor initial conditions on SMBH coalescence was investigated. Differing mass resolutions between the stellar particles and the SMBHs for each physical realisation were also tested. The simulations were performed on the supercomputers Puhti and Mahti at CSC, the Finnish IT Centre for Science.

SMBH coalescence was found to only occur in mergers involving SMBH binaries of equal mass, with the most rapid coalescence observed in galaxies with a steep density profile. In particular, the eccentricity of the SMBH binary was observed to be crucial for coalescence: all simulations that coalesced displayed an orbital eccentricity in excess of $e = 0.7$ for the majority of the time for which the binary was bound. Simulations of higher mass resolution were found to have an increased number of stellar particles able to positively interact with the SMBH binary to remove orbital energy and angular momentum, driving the binary to coalescence. The gravitational wave emission from an equal mass SMBH binary in the final stages before merging was calculated to be within the detection limits required for measurement by pulsar timing arrays.

Mergers between galaxies of unequal mass SMBHs were unable to undergo coalescence irrespective of mass resolution or progenitor density profile, despite the binary in some of these simulations displaying a high orbital eccentricity. It was determined that the stellar particles interacting with the SMBH binary were unable to remove the required orbital energy and angular momentum to bring the SMBHs to within the separation required for efficient gravitational wave emission.

A trend between increasing mass resolution and increasing number of stellar particles able to remove energy from the SMBH binary was observed across all the simulation suites. This observation is of paramount importance, as three-body interactions are essential in removing orbital energy and angular momentum from the SMBH binary, thus overcoming the Final Parsec Problem. As such, it is concluded that the Final Parsec Problem is a numerical artefact arising from insufficient mass resolution between the stellar particles and the SMBHs rather than a physical phenomenon.

Avainsanat — Nyckelord — Keywords
black hole physics – galaxies: interactions – galaxies: kinematics and dynamics

Säilytyspaikka — Förvaringsställe — Where deposited

Muita tietoja — övriga uppgifter — Additional information

Acknowledgements

I would first like to thank my supervisors, Prof. Peter Johansson and Matias Mannerkoski, for their guidance and patience throughout the course of the thesis. My gratitude I extend also to the entire Helsinki Theoretical Astrophysics Research Group for their support. Für ihre Ermutigung möchte ich meiner Freundin Elisa und ihren Eltern danken. Finally, to my family back in Australia: Mum, Dad, Cate, and Emma, thank you for your unwavering belief in me.

Contents

1. Introduction

1.1 Gravity and Galaxies

Profound ideas often hail from humble beginnings. Such is the story of gravity, which after famously announcing itself to the scientific community with a well-placed apple in the 17$^{\text{th}}$ century, has come to be recognised as a fundamental constituent of the physical universe. Up until the beginning of the 20$^{\text{th}}$ century, gravity was solely understood in the Newtonian sense: an attractive, long-range force F_{g} acting between two particles such that:

$$F_{\text{g}} = \frac{GM_1M_2}{r^2}, \tag{1.1}$$

where the particle masses M_1 and M_2 are separated by a radial distance r, and G is a constant. For systems where the constituent masses are not exceptionally compact and have relative velocities much smaller than the speed of light c, the Newtonian understanding of gravity captures the dynamical evolution of the system remarkably well. Newtonian gravity provides the framework to begin modelling the large-scale interactions between massive stellar systems hypothesised to be 'Island Universes' by Immanuel Kant (1724-1804). These 'Island Universes', or galaxies, were later confirmed to lie far beyond the Milky Way by Edwin Hubble in 1923. With improved observational capabilities during the 20$^{\text{th}}$ century, galaxies were shown to be vastly complicated structures containing large amounts of matter that is not visible (Kapteyn, 1922; Zwicky, 1933; Rubin & Ford, 1970). This non-luminous matter, termed dark matter (DM), is believed to comprise more than 84% of the total matter in the present universe (Planck Collaboration et al., 2018). Today, galaxies are understood to be immense, gravitationally-bound structures containing both stars and gas, and are confined by the gravity of the DM halo within which they reside (e.g. Mo et al., 2010). Galaxies are not static objects: they are constantly evolving and interacting to both disrupt one another and form anew. The dynamical disruption caused by the interaction of two galaxies is called galactic merging.

The presence of a single massive compact body is prevalent in the centre of nearly all massive galaxies, including the Milky Way (Kormendy, 1988; Kormendy & Richstone, 1995; Genzel et al., 1997; Ghez et al., 1998; Gebhardt et al., 2000). Such bodies are predicted from the theory of General Relativity, which revolutionised the treatment of gravity to incorporate the response of spacetime to the matter content within it (e.g. Carroll, 2004). The body in the central regions of massive galaxies is generally regarded to be a type of black hole with a mass between $10^6\,\mathrm{M}_\odot$–$10^{10}\,\mathrm{M}_\odot$, termed a supermassive black hole (SMBH). The formation of SMBHs is currently not well understood (Begelman et al., 2006; Kulier et al., 2015; Regan et al., 2017). As the host galaxies undergo merger events, the central SMBHs of both galaxies are expected to interact gravitationally. Interactions between compact bodies at very small separations produce a rippling effect through the fabric of spacetime: a gravitational wave (GW). Gravitational wave physics promises to fundamentally transform the ability of the scientific community to understand the most violent and cataclysmic releases of energy in the known universe, and is an imperative direction of ongoing and future research. The first GW detection occurred in 2015 between two stellar mass black holes, validating the observational methods by which we may probe such events (Abbott et al., 2016). The frequency of the emitted GW signal is related to the masses of the inspiralling compact bodies, with the GW signal from SMBH interactions yet to be detected (Burke-Spolaor et al., 2019; Goulding et al., 2019). To this end, the measurements from both current observations, such as pulsar timing arrays, and future missions, such as the Laser Interferometer Space Antenna (LISA), will play a critical role in the unravelling of the intricacies of black hole evolution.

1.2 Merging Supermassive Black Holes

Naïvely, one may consider the eventual coalescence of the SMBHs in an interacting galaxy merger to be inevitable owing to the gravitational influence exerted by each SMBH. However, as discussed by Begelman et al. (1980), many complex phenomena are required for this to occur: SMBH merging is not trivial. Owing to both the complicated nature and long timescales of millions of particles interacting within a galactic setting, it is to numerical modelling that astrophysicists have turned to better understand the fate of a SMBH binary. Numerical modelling forms a primary basis from which the expected gravitational wave signal from a merging SMBH can be calculated, which is the prime target for upcoming missions such as LISA (Amaro-

Seoane et al., 2017). As a result of the extreme range in physical scales encountered in galaxy mergers, it has previously been difficult to accurately capture both the large-scale dynamics, such as the evolution of the outer DM halo, and the small-scale dynamics of the SMBH binary (e.g. Rantala et al., 2017). This has rendered many simulations incapable of modelling the extreme range of physical scales required for SMBH binary dynamics with a single, self-consistent prescription. Additionally, the computational demand of galactic simulations prevents the representation of individual stars and DM particles; simulation particles are used to represent the motion of some hundreds of thousands of physical particles. Combined, the two difficulties have resulted in a number of SMBH binary simulations stalling, i.e. the SMBHs orbit each other perpetually for a duration longer than the age of the universe at a separation of approximately one parsec (Milosavljević & Merritt, 2001; Merritt, 2006). At one parsec, the GW emission is typically exceptionally weak, and thus not a viable mechanism for reducing the SMBH binary orbit to sub-parsec separations. The stalling of a SMBH binary at parsec separations is termed the 'Final Parsec Problem' (Milosavljević & Merritt, 2001). There is a lack of observed SMBH binary systems in physical galaxies (e.g. Kormendy & Ho, 2013), indicating one of two potential causes. The first, that there is an observational bias towards single SMBH systems. Alternatively, the complex physics in galactic merger simulations has yet to be accurately captured, and requires further model development.

1.3 Aim of the Thesis

The aim of this thesis is to determine if the Final Parsec Problem is a physical phenomenon in the merging of massive early-type galaxies, or a numerical manifestation arising from poor mass resolution between the SMBHs and the stellar and DM particles. To investigate the Final Parsec Problem, a number of different physical progenitor properties are simulated at varying mass resolutions with the KETJU code developed by the Helsinki Theoretical Extragalactic Astrophysics Research Group.

This thesis consists of six chapters, of which this introductory chapter is the first. In Chapter 2, a background to the merging of supermassive black holes in collisionless galactic systems is presented. In Chapter 3, the computational methods used in the KETJU code are discussed. Chapter 4 presents the motivation for the physical parameters used in the merger progenitors. In Chapter 5, the analysis of the simulation results is given. The thesis conclusions and remarks for future research are given in Chapter 6.

2. Background Theory

This chapter details the theoretical framework within which the Final Parsec Problem is to be investigated. As this work focuses on supermassive black hole coalescence in a controlled galactic setting, the environmental properties of the simulation must be understood. An overview of the photometric and kinematic properties of early-type galaxies is presented, along with scaling relations between the host galaxy and its central supermassive black hole. The conditions and mechanisms of galaxy mergers, and in particular the merging of the central supermassive black holes, is then discussed. A review of the Final Parsec Problem in the literature is then presented, followed by a brief discussion on two important numerical techniques used in the modelling of black hole dynamics: algorithmic regularisation and Post-Newtonian corrections.

2.1 Massive Elliptical Galaxies

Galaxy classification schemes generally belong to one of two categories: those classification schemes based upon the visual morphology of a galaxy (e.g. Hubble, 1926; de Vaucouleurs, 1959; Graham, 2019), and those schemes based upon kinematics (e.g. Emsellem et al., 2007; Cappellari et al., 2011; van de Sande et al., 2017). In this work, the simulated galaxies are chosen from the morphological classification.

In the morphological classification scheme, galaxies are historically categorised as either early-type galaxies (ETGs), or late-type galaxies (LTGs), though there is no evidence to imply an evolution between the two classes (e.g. Carroll & Ostlie, 2017). Nearly all massive galaxies regardless of morphology are thought to have a supermassive black hole (SMBH) at their centres (e.g. Mo et al., 2010). The separation between ETGs and LTGs is visualised by the fork in the Hubble tuning fork diagram (Jeans, 1928; Hubble, 1936), shown in Fig. 2.1. ETGs may be categorised as either elliptical (E) or lenticular (S0) galaxies. Elliptical galaxies appear as rounded ellipsoids (see Table 2.1 for ellipsoid types) and are described as a bulge-

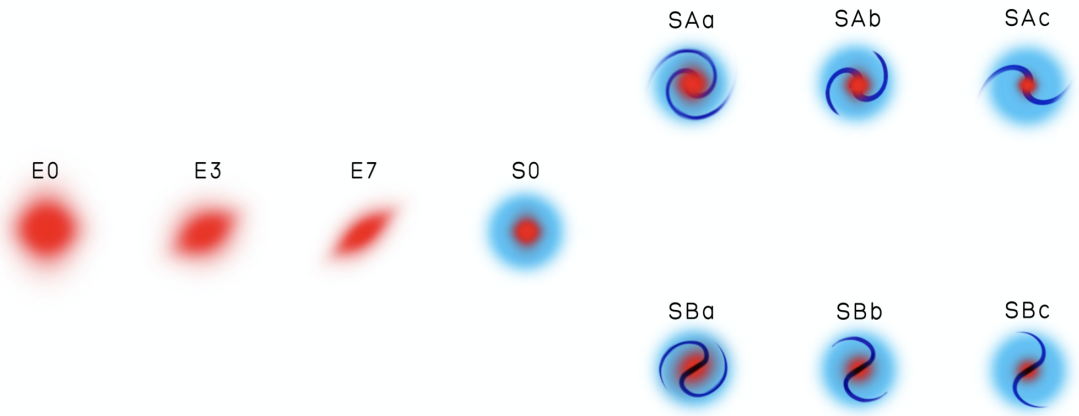

Figure 2.1: The Hubble tuning fork diagram used as the basis of morphological galaxy classification. Elliptical (E) and lenticular (S0) galaxies, collectively early-type galaxies, are to the left of the fork. Spiral galaxies are divided in barred (SB) and unbarred (SA), with later-type spirals presenting spiral arms less tightly wound to the central bulge. Figure reproduced from Graham (2019) (their Fig. 1).

System	Ellipsoid Axes Relation
Triaxial	$\alpha > \beta > \gamma$
Oblate	$\alpha = \beta > \gamma$
Prolate	$\alpha > \beta = \gamma$
Spheroid	$\alpha = \beta = \gamma$

Table 2.1: Relation of the three axes of an ellipsoid system.

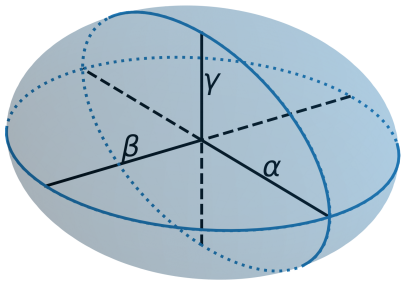

Figure 2.2: Spheroid with axes indicated as in Table 2.1.

only system containing the stellar mass and with very little cold gas, enveloping dark matter halo.

Elliptical galaxies may be further subdivided into one of eight classes indicated by an integer X in the range of 0 to 7, where the integer X is ten times the ellipticity ε rounded to the nearest integer at the radius which encloses half the galactic light (see §2.1.2). The ellipticity ε is defined as:

$$\varepsilon = 1 - \frac{b}{a}, \tag{2.1}$$

in which a and b are the apparent semimajor and semiminor axis of the projected galaxy respectively (e.g. Mo et al., 2010). Critically, two identical elliptical galaxies may be classified into two different subclasses as a result of inclination effects resulting from the observer position with respect to the galaxy. Lenticular galaxies are

composed of both a bulge and an external disc that has no apparent substructure. LTGs consist of spiral galaxies, which may be of the barred (SB) and unbarred (SA) kind. Within each of SA and SB galaxies, further division is assigned by a suffix a, b, or c, dependent on the bulge-to-disc mass ratio, and the degree to which the spiral arms are wound about the nucleus (see Fig. 2.1). Further discussion of disc galaxies, whilst an extensive topic, is not given here as the morphological-type to be investigated is the elliptical galaxy.

2.1.1 General Properties

Elliptical galaxies, regardless of Hubble subclass type, may be stratified by the stellar mass within the system. Three primary classes emerge: cD ellipticals, normal ellipticals, and dwarf ellipticals.

Elliptical galaxies of the cD class are exceptionally massive, typically with stellar mass in excess of $10^{12}\,\mathrm{M}_\odot$ (e.g. Mo et al., 2010) and half the total light (the effective radius, see §2.1.2) contained within ∼80 kpc (Kormendy, 1980; Schombert, 1986). The mass-to-light ratio Υ of cD galaxies increases dramatically at large radii to values in excess of $100\,\mathrm{M}_\odot/\mathrm{L}_\odot$ (Forman et al., 1985), implying the existence of a dark matter (DM) halo enveloping the stellar mass (e.g. Mathews, 1978; Gebhardt & Thomas, 2009). In the V-band, cD galaxies have an absolute magnitude of ~ -22 to -25 (Schombert, 1986), with a low surface brightness core embedded within a luminosity profile that radially decreases to a diffuse envelope. Such galaxies are usually found in the centres of dense galaxy clusters.

Normal elliptical galaxies have a typical stellar mass range of $10^{10}\,\mathrm{M}_\odot$ to $10^{12}\,\mathrm{M}_\odot$ (e.g. Lintott et al., 2008), and consequently have a lower absolute magnitude of -15 to -23 in the B band compared to cD ellipticals (Carroll & Ostlie, 2017). The mass-to-light ratio of normal elliptical galaxies increases with radius. Normal elliptical galaxies typically have a luminous mass distribution that is centrally condensed, though the maximum radial extent of such galaxies may extend up to 200 kpc.

Finally, dwarf ellipticals are the least massive of the three elliptical classes, with stellar masses ranging from $10^{7}\,\mathrm{M}_\odot$ to $10^{9}\,\mathrm{M}_\odot$ and absolute B-magnitude in the range of -13 to -19 (e.g. Carroll & Ostlie, 2017). The radial extent of dwarf ellipticals are not observed to extend beyond 10 kpc.

Elliptical galaxies, in particular cD ellipticals, have very little cold gas or dust from which to sustain star formation, and thus appear as red in $B-V$ photometric colour (Roberts & Haynes, 1994). The lack of cold gas and dust within the central

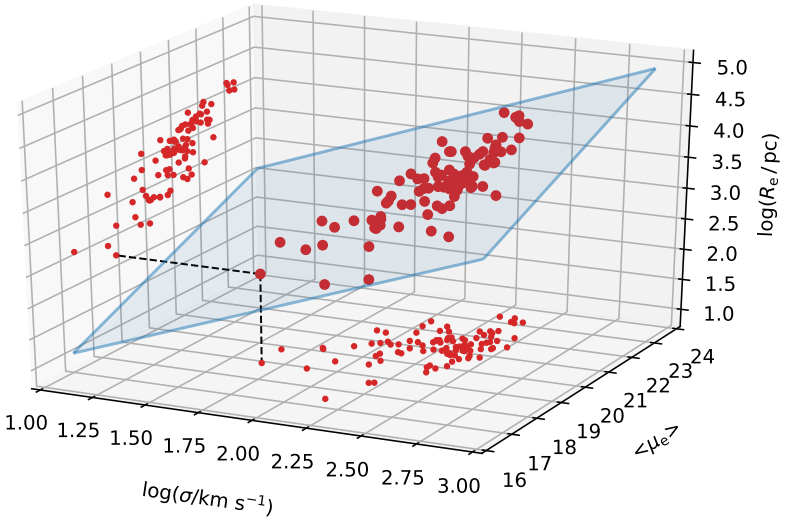

Figure 2.3: Correlation of the effective radius R_e, the mean surface brightness $\langle \mu_e \rangle$ within $1\,R_e$ in mag arcsec^{-2}, and the velocity dispersion σ_0 in the Fundamental Plane. Elliptical galaxies are found to lie within a thin plane in the parameter space, constraining formation and evolution history. Figure produced with data from Mármol-Queraltó et al. (2009); Annibali et al. (2010); Koleva et al. (2011) as presented in Samir et al. (2016).

regions of a massive (i.e., cD type) elliptical galaxy allows for the system to be modelled as a collisionless system of stellar particles with a power-law density profile, $\rho \sim r^{-\gamma}$ (e.g. Gebhardt et al., 1996). The red colouring of massive ellipticals implies that the galaxy is dominated by old, metal-rich stars; a slight radial-colour gradient indicates that stars at large radii are younger, and thus appear more blue than central stars (Peletier et al., 1990). Elliptical galaxies that are more luminous are also found to be redder compared to less luminous ellipticals (Sandage & Visvanathan, 1978).

Scaling relations between the central velocity dispersion σ_0, effective radius R_e, and the average surface brightness within one effective radius $\langle I \rangle_e$ place tight constraints on elliptical galaxy properties, particularly in the context of formation by merger events (see §2.2) (e.g. Mo et al., 2010). One such scaling relation is the Faber-Jackson relation, which is written:

$$L \propto \sigma_0^{\beta}, \qquad \beta \sim 4, \tag{2.2}$$

where $L \propto \langle I \rangle_e R_e^2$ (Faber & Jackson, 1976). From Eq. (2.2), those elliptical galaxies

with higher central velocity dispersions are found to be more luminous, and hence more massive, than ellipticals with lower central velocity dispersions.

Similarly, defining the diameter D_n within which the average integrated surface brightness obtains a given value $\langle I \rangle_n$, the relation:

$$D_n \propto \sigma_0^a \langle I \rangle_{\rm e}^{b+1/\xi} \tag{2.3}$$

is observed. Eq. (2.3) may be reduced to $D_n \propto \sigma_0^a$ if it assumed that $\langle I \rangle_n = 20.75$ mag arcsec^{-2} as in Dressler et al. (1987). Together, the Faber-Jackson and $D_n - \sigma$ relation are found to be projections of a three-dimensional plane to which elliptical galaxies are constrained (e.g. Mo et al., 2010). The plane, termed the Fundamental Plane, takes the form:

$$\log R_{\rm e} = a \log(\sigma_0) + b \log\left(\langle I \rangle_{\rm e}\right) + C, \tag{2.4}$$

where C is some constant, and is shown in Fig. 2.3. The coefficient a is dependent on the photometric band the galaxy is observed in, whereas the photometric dependence of the coefficient b is weaker. Using the 9000 galaxies from the Sloan Digital Sky Survey (SDSS) with data in the r-band, Bernardi et al. (2003) constrained $a = 1.49 \pm 0.05$ and $b = -0.75 \pm 0.01$, which is consistent with earlier work by Pahre et al. (1998).

2.1.2 Photometric Properties

The surface brightness I of a galaxy (or any extended astrophysical object) is a measure of the energy received per unit area from a unit solid angle within a unit time (e.g. Mo et al., 2010). Many attempts at modelling the radial distribution of the surface brightness of elliptical galaxies were made especially during the 20$^{\rm th}$ century, most notably by de Vaucouleurs (1948). A generalisation of the de Vaucouleurs (1948) profile is the Sérsic (1963) profile, defined as:

$$I(r) = I_{\rm e} \exp\left[-\beta_n \left\{\left(\frac{r}{R_{\rm e}}\right)^{1/n} - 1\right\}\right], \tag{2.5}$$

where $R_{\rm e}$ is the radius within which half of the total light is contained, termed the effective radius. $I_{\rm e}$ is the surface brightness at 1 $R_{\rm e}$, and $\beta_n \simeq 2n - 0.324$ for $n \gtrsim 1$. In the case $n = 4$, Eq. (2.5) reduces to the de Vaucouleurs (1948) profile. The central cusp slope of elliptical galaxies is defined as:

$$\gamma \equiv \frac{{\rm d} \log I}{{\rm d} \log r}. \tag{2.6}$$

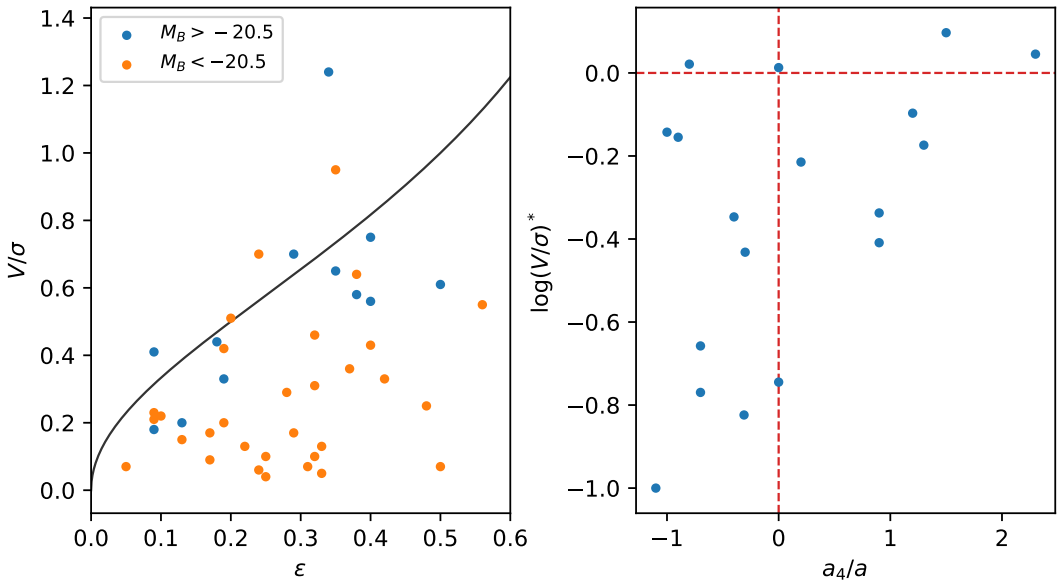

Figure 2.4: *Left:* Ratio of ordered velocity V to central velocity dispersion σ as a function of ellipticity ε. Bright galaxies (orange points) lie significantly below the V/σ ratio expected for an ETG that is flattened by rotation (black line), whereas faint ETGs display a V/σ consistent with rotational flattening. Figure produced with data from Davies et al. (1983). *Right:* $(V/\sigma)^*$ parameter (see text for details) plotted as a function of the mean galaxy boxiness a_4/a. Discy ($a_4 > 0$) galaxies have $(V/\sigma)^* \lesssim 1$, whereas boxy galaxies have $(V/\sigma)^* \sim 0.1$. Figure produced with data from Kormendy & Bender (1996).

Many elliptical galaxies, through high spatial resolution imaging from the Hubble Space Telescope (HST), have been found to possess centrally cored regions, i.e. a density profile that displays a deficiency in the central ($r \lesssim 100\,\mathrm{pc}$) region (Ferrarese et al., 1994). Consequently, elliptical galaxies are sometimes referred to as 'cored' if the central density is $\gamma < 0.3$ and 'cusped' if $\gamma \gtrsim 0.3$ (e.g. Mo et al., 2010). Modelling suggests that core-scouring may occur as a result of binary SMBH merging during galactic mergers, whereby stars are ejected via three-body interactions with the binary (e.g. Rantala et al., 2018).

Central to the photometric analysis of ETGs is the modelling of ETGs as a sequence of isophotes. Isophotes are contours of constant surface brightness (e.g. Mo et al., 2010), with the deviation from an elliptical shape quantified as a Fourier series of the form:

$$\Delta(\theta) = a_0 + \sum_{n=1}^{\infty} \left(a_n \cos(n\theta)\right), \tag{2.7}$$

where a_0 is the contour radius which represents a circular isophote, as in Bender & Möllenhoff (1987). The second non-zero term ($a_2 \cos 2\theta$) indicates the degree of

ellipticity, and the third non-zero term ($a_4 \cos 4\theta$) indicates the degree of boxiness of the isophote, with $a_4 < 0$ tending to visually-boxy isophotes, and $a_4 > 0$ to visually-discy isophotes (e.g. Carroll & Ostlie, 2017). Bright (B-band absolute magnitude $\mathcal{M}_B \leq -20.5$) ETGs are typically found to be boxy, whereas faint ($-20.5 \leq \mathcal{M}_B \leq -18$) ETGs are typically discy. The boxiness of an isophote also correlates with the kinematics of the ETG, readily seen in the ratio of ordered line-of-sight velocity V to the central velocity dispersion σ (see §2.1.3). For an oblate elliptical galaxy flattened by rotation, the ratio V/σ is related to ellipticity ε by:

$$\frac{V}{\sigma} \approx \sqrt{\frac{\varepsilon}{1-\varepsilon}}, \tag{2.8}$$

as in Kormendy (1982), and is shown as the solid line in the left panel of Fig. 2.4. Bright ETGs (orange points in Fig. 2.4a) lie below the relation of Eq. (2.8), indicating these galaxies to be predominantly pressure supported. Conversely, faint ETGs (blue points in Fig. 2.4a) follow the relation of Eq. (2.8), indicating these galaxies are rotationally supported (Bender, 1988; Kormendy & Djorgovski, 1989). A similar trend is observed between the $(V/\sigma)^*$ parameter, defined as the ratio of V/σ to the value determined from Eq. (2.8), and the ratio of Fourier coefficients a_4/a_0 in Eq. (2.7). Boxy isophotes have $(V/\sigma)^* \sim 0.1$, and discy galaxies have $(V/\sigma)^* \lesssim 1.0$, as in the right panel of Fig. 2.4. It is hypothesised that boxy-isophotes seen in elliptical galaxies may be a relic of past merger events (Carroll & Ostlie, 2017).

2.1.3 Kinematic Properties

From observations of galaxies, three dimensional quantities such as rotation velocity and velocity dispersion are unable to be recovered due to projection effects. Instead, the observed quantities are projections of the corresponding three-dimensional physical quantities, resulting in line-of-sight (LOS) kinematics. In modelling galactic properties, especially in isolated merger simulations, a spatially invariant mass-to-light ratio is often assumed, namely $\Upsilon(\boldsymbol{x}) = \Upsilon$. If the particles of a system are evolving under the influence of a smooth potential field, the particles have a distribution in coordinate space and velocity space (e.g. Mo et al., 2010). Combined, the six-dimensional space is called phase space; the system is characterised at any time t by the phase space distribution function $f(\boldsymbol{x}, \boldsymbol{v}, t)$. The three-dimensional mass distribution $\rho(\boldsymbol{x}, t)$ is found from integrating the phase space distribution function over velocity space:

$$\rho(\boldsymbol{x}, t) = m \int f(\boldsymbol{x}, \boldsymbol{v}, t)\, \mathrm{d}^3\boldsymbol{v}, \tag{2.9}$$

where m is a constant particle mass. The projected mass surface density may be computed from $\rho(\boldsymbol{x}, t)$ as:

$$\Sigma(x, y, t) = \int \rho(\boldsymbol{x}, t)\, \mathrm{d}z, \tag{2.10}$$

which yields for the line-of-sight velocity distribution (LOSVD):

$$\mathcal{L}(x, y, v_z, t) = \frac{1}{\Sigma(x, y, t)} \iiint f(\boldsymbol{x}, \boldsymbol{v}, t)\, \mathrm{d}v_x \mathrm{d}v_y \mathrm{d}z, \tag{2.11}$$

as in Mo et al. (2010). The LOSVD, whilst close to a Gaussian, deviates slightly, and thus requires a more general functional form in order to be modelled (van der Marel & Franx, 1993). Thus, the LOSVD is typically parametrised using a Gauss-Hermite series of the form:

$$\mathcal{L}(v) = \frac{\alpha(w)}{\sigma} \left[1 + \sum_{j=3}^{N} h_j H_j(w) \right], \tag{2.12}$$

where

$$\alpha(w) \equiv \frac{1}{\sqrt{2\pi}} e^{-w^2/2}, \quad w \equiv \frac{v - V}{\sigma}. \tag{2.13}$$

Here v is the LOS velocity, V is the mean and σ is the dispersion of the best-fit Gaussian profile, and H_j is the Hermite polynomial of degree j (e.g. van der Marel & Franx, 1993). The first five Hermite polynomials are:

$$H_0(w) = 1, \tag{2.14}$$

$$H_1(w) = \sqrt{2} w, \tag{2.15}$$

$$H_2(w) = \frac{1}{\sqrt{2}} (2w^2 - 1), \tag{2.16}$$

$$H_3(w) = \frac{1}{\sqrt{6}} \left(2\sqrt{2} w^3 - 3\sqrt{2} w \right), \tag{2.17}$$

$$H_4(w) = \frac{1}{2\sqrt{6}} \left(4w^4 - 12w^2 + 3 \right). \tag{2.18}$$

The Gauss-Hermite moments h_j are defined from the Hermite polynomial of degree j by:

$$h_j = \frac{2}{\pi} \frac{\gamma_0}{\gamma} \int_{-\infty}^{\infty} \mathcal{L}_0(v) \alpha(w) H_j(w)\, \mathrm{d}v, \tag{2.19}$$

where $\mathcal{L}_0(v)$ is the true LOSVD, γ_0 is the ratio of equivalent width of the absorption lines of the galaxy to the template spectrum, γ is the data line strength estimate, and $\alpha(w)$ is given by Eq. (2.13) (van der Marel & Franx, 1993). The Gauss-Hermite moments are used to measure the deviation of the LOSVD from the best-fit Gaussian profile. In practice, the best-fit profile is modelled with $h_0 = 1$ and $h_1 = h_2 = 0$, hence the summation in Eq. (2.12) beginning at $j = 3$. The primary contribution to

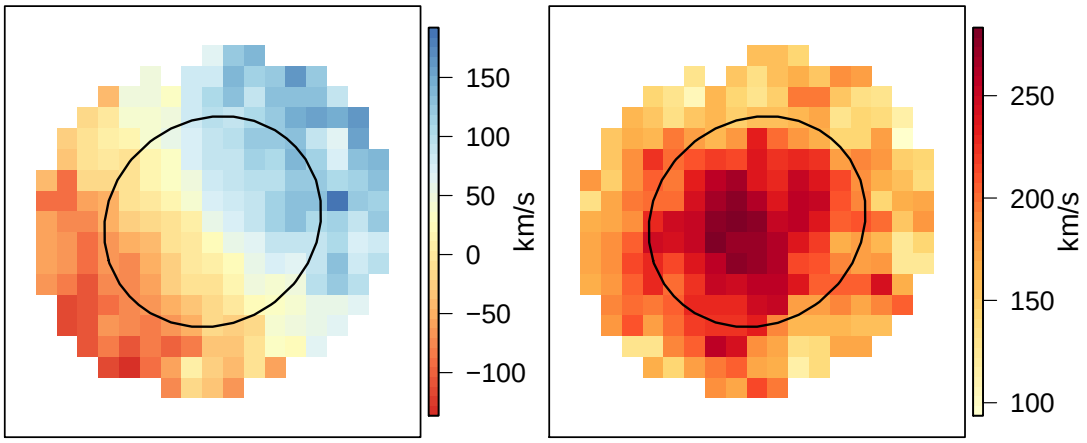

Figure 2.5: Kinematic integral field unit maps of an elliptical galaxy as part of the SAMI galaxy survey (Bryant et al., 2015), adapted from Rawlings et al. (2020). *Left:* Rotational velocity (red: receeding, blue: approaching) in units of $\mathrm{km\,s^{-1}}$, demonstrating the radially increasing rotational velocity. *Right:* Velocity dispersion in units of $\mathrm{km\,s^{-1}}$, with peak velocity dispersion occurring at the galactic centre. The black ellipse indicates $1\,R_\mathrm{e}$ in both plots.

the measurement of the deviation is made by h_3 and h_4, which provide a measure of the asymmetric and symmetric deviations of the LOSVD from the best-fit Gaussian profile, respectively (van der Marel & Franx, 1993).

Since the work of Bertola & Capaccioli (1975), it has been widely shown that elliptical galaxies (and the bulges of disc galaxies) are not solely supported by velocity dispersion, but also exhibit discernible rotation (e.g. Scorza & Bender, 1995; Emsellem et al., 2011). An example of a rotating elliptical galaxy, taken from the Sydney AAO Multi-object Integral Field (SAMI) galaxy survey of galaxies with redshift $0.004 \leq z \leq 0.095$ (Bryant et al., 2015), is presented in Fig. 2.5. Rotational velocity (left panel) typically increases with radius, whereas velocity dispersion (right panel) decreases with radius. The degree of rotation of ETGs still however remains well below that of LTGs, as seen in the V/σ distirbution in Fig. 2.6. To quantify the degree of rotation in ETGs, Emsellem et al. (2007) defined a luminosity-weighted spin parameter λ_R, such that:

$$\lambda_R \equiv \frac{\langle R|V|\rangle}{\langle R\sqrt{V^2+\sigma^2}\rangle}, \tag{2.20}$$

where R is the radial distance to the galactic centre (typically set to $1\,R_\mathrm{e}$), V is the stellar velocity, σ the stellar velocity dispersion, and $\langle\rangle$ denotes a luminosity-weighted sky average. Emsellem et al. (2007) define those ETGs with $\lambda_{R_\mathrm{e}} < 0.31\sqrt{\varepsilon_\mathrm{e}}$, where ε_e is the ellipticity of the galaxy at $1\,R_\mathrm{e}$, as slow rotators. Those ETGs with $\lambda_{R_\mathrm{e}} > 0.31\sqrt{\varepsilon_\mathrm{e}}$ are correspondingly termed fast rotators. The correlation be-

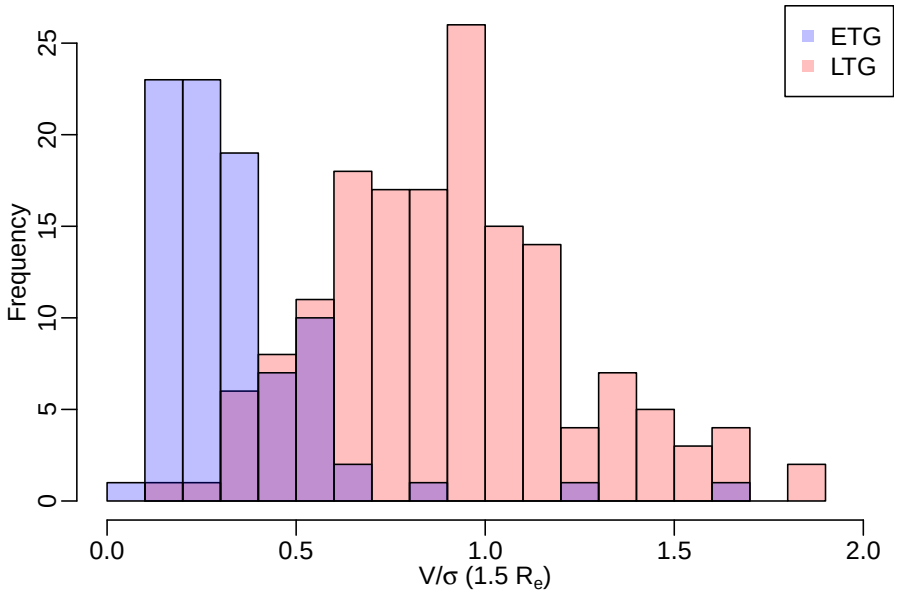

Figure 2.6: V/σ ratio at $1.5\,R_{\rm e}$ for a subset of galaxies with stellar kinematics out to $1.5\,R_{\rm e}$ as part of the SAMI galaxy survey. ETGs display a V/σ that peaks at ~ 0.2, whereas LTGs display a V/σ that peaks at a higher value of ~ 0.9.

tween the kinematics and isophotal properties are also apparent, with slow rotators typically displaying boxy isophotes, and fast rotators typically displaying disc-like isophotes (Davies et al., 1983). Radial variation in both ellipticity and spin λ_R may also be used to determine underlying structure not visible in integral field unit (IFU) observations of galaxies (Bellstedt et al., 2017; Rawlings et al., 2020).

2.1.4 Supermassive Black Holes

Supermassive black holes are believed to reside at the centre of nearly all massive galaxies, and have a mass range of $10^6\,\mathrm{M}_\odot \lesssim M_\bullet \lesssim 10^{10}\,\mathrm{M}_\odot$ (e.g. Mo et al., 2010). Observationally, SMBHs are searched for by measuring the radial variation in the mass-to-light ratio $\Upsilon(r)$ of a galaxy, whereby a SMBH would be observed as an increase in the mass-to-light ratio at very small radii from the galactic centre (e.g. Mo et al., 2010). Further evidence for the presence of a SMBH at the galactic centre is provided by the rising of the central velocity dispersion σ, and analysing the h_3 and h_4 kinematic components of the LOSVD of the galaxy. As investigated for M87 in van der Marel (1994), Gauss-Hermite moments about zero indicate no systematic deviation in the LOSVD that may be attributed to a system with radial anisotropy. A central SMBH is thus the most likely candidate for the observed velocity dispersions.

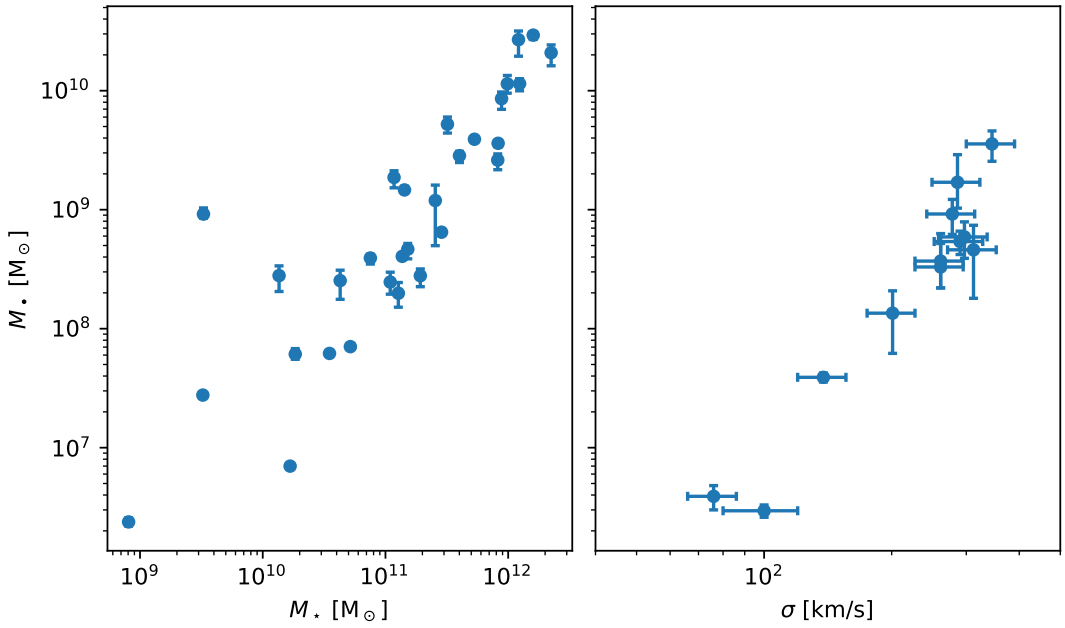

Figure 2.7: SMBH scaling relations. *Left:* Correlation of SMBH mass with the stellar bulge mass from Magorrian et al. (1998). *Right:* Correlation of SMBH mass with luminosity-weighted mean velocity dispersion within $1\,R_\mathrm{e}$ of the bulge from Ferrarese & Merritt (2000). Note the SMBHs used between the two samples differ.

A black hole is characterised by its Schwarzschild radius R_S, defined in standard units as:

$$R_\mathrm{S} = \frac{2GM_\bullet}{c^2}, \tag{2.21}$$

where G is the Newtonian gravitational constant and $M_\bullet$ is the black hole mass. The Schwarzschild radius defines the maximum radius at which the gravitational potential of the mass prevents photons from exiting the gravitational well of the mass. The radial extent to which the SMBH may significantly influence the dynamics of a system is given by:

$$r_\mathrm{h} = \frac{GM_\bullet}{\sigma_\star^2}, \tag{2.22}$$

where $\sigma_\star$ is the LOS velocity dispersion of stars within $1\,R_\mathrm{e}$ of the galactic centre, following Rantala et al. (2018). A spinning SMBH can drastically alter the surrounding spacetime, severely affecting the dynamics of neighbouring particles. In the present work, all SMBHs are modelled as non-rotating.

As one might infer from Eq. (2.22), tight relations between the physical and kinematic properties of the SMBH and the surrounding stellar environment are observed. The scaling relations are used to construct the model galaxies used in this work, with specific detail presented in §4. Most notable of these include the relation

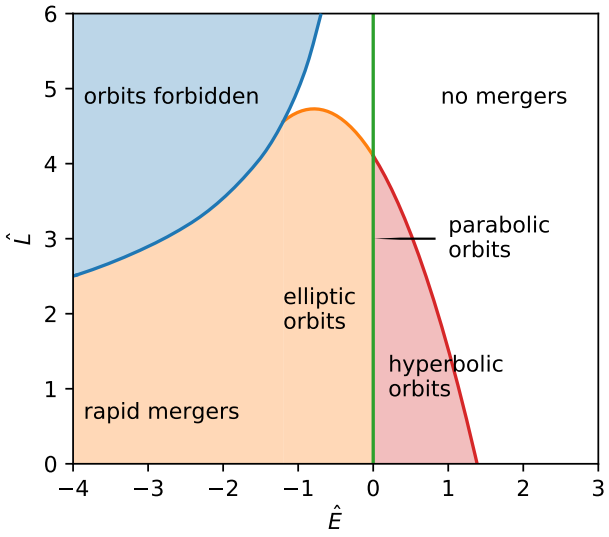

Figure 2.8: Merging criteria for two equal mass spherical galaxies. Merger progenitors with $\hat{L} \gtrsim 4$ or $\hat{E} \gtrsim 1$ do not merge within the Hubble time. Merging is most rapid for systems with low $\hat{L}$ and on bound orbits ($\hat{E} \leq 0$). Figure adapted from Mo et al. (2010).

between SMBH mass $M_\bullet$ and bulge luminosity (and hence bulge mass $M_\star$), such that:

$$M_\bullet \propto M_\star^\alpha, \tag{2.23}$$

as in Magorrian et al. (1998), Marconi & Hunt (2003), and Häring & Rix (2004). The relation is shown in the left panel of Fig. 2.7. Additionally, the SMBH mass $M_\bullet$ is observed to scale with the central stellar velocity dispersion $\sigma_\star$ of the galaxy as:

$$M_\bullet \propto \sigma_\star^\gamma, \tag{2.24}$$

as in Gebhardt et al. (2000) and Ferrarese & Merritt (2000). The relation is shown in the right panel of Fig. 2.7. Both the $M_\bullet - M_\star$ and $M_\bullet - \sigma$ relations indicate that the properties of the central SMBH are strongly correlated with the overall evolution of the galaxy itself.

2.2 Galaxy Mergers

2.2.1 Orbital Criteria

For two galaxies to merge, strict criteria on the orbital energy per unit mass $E_{\rm orb}$ and orbital angular momentum per unit mass L of both progenitors must be satisfied (Fig. 2.8). Assuming that each galaxy of mass M has median radius $r_{\rm med}$ and

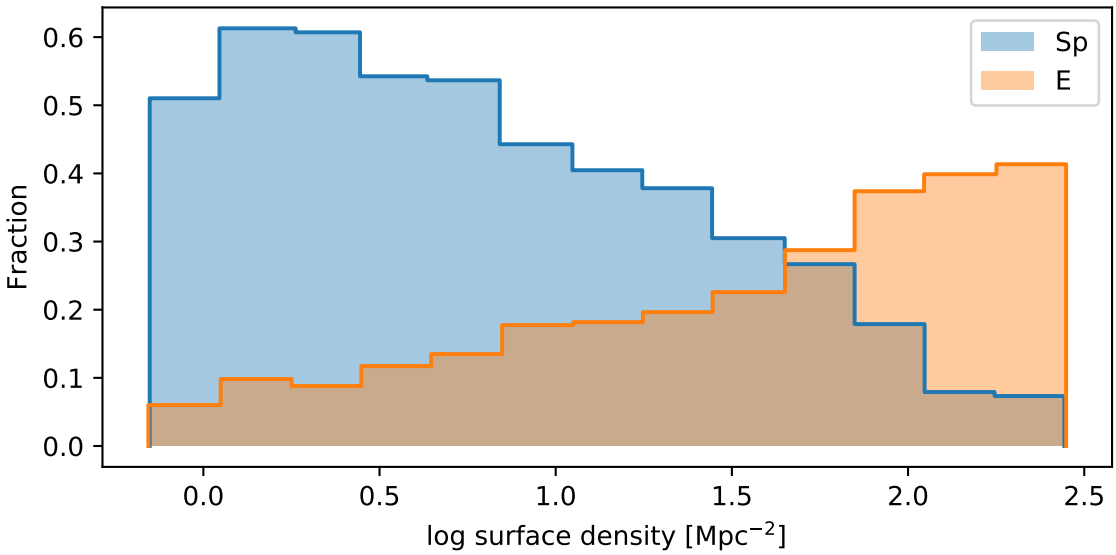

Figure 2.9: Morphology dependence on galactic environment for ellipticals and spirals. Spiral galaxies are found to populate low density environments, whereas elliptical galaxies are observed to populate high density environments. The environmental dependence is naturally explained by the merger history of galaxies of different morphologies. Lenticular galaxies are not shown in the plot. Figure produced using data from Dressler (1980).

internal mean-square velocity $\langle v^2 \rangle = aGM/r_{\rm med}$ (where a is of order unity), the dimensionless parameters $\hat{E}$ and $\hat{L}$ are defined as:

$$\hat{E} \equiv \frac{E_{\rm orb}}{\frac{1}{2}\langle v^2 \rangle} \qquad \text{and} \qquad \hat{L} \equiv \frac{L}{\langle v^2 \rangle^{1/2} r_{\rm med}}. \tag{2.25}$$

Elliptic orbits have $\hat{E} < 0$ and parabolic orbits have $\hat{E} = 0$: both orbits are bound. Conversely, hyperbolic orbits are unbound, and are characterised by $\hat{E} > 0$. The largest angular momentum $\hat{L}$ for bound orbits is given by a circular orbit (shown as the blue line in the upper left corner of Fig. 2.8). The maximum angular momentum with which a merger may occur for parabolic orbits within the Hubble time corresponds to $\hat{L} \sim 4$. In the case of zero angular momentum, a merger may still occur for orbital energies as high as $\hat{E} \sim 1.4$. Orbital configurations which lie within the orange and red regions in the $\hat{L}$-$\hat{E}$ parameter space of Fig. 2.8 are plausible (e.g. Binney & Tremaine, 2008; Mo et al., 2010). The above relations must hold irrespective of galaxy morphology or environment for a merger event involving two galaxies to occur.

2.2.2 Environmental Factors

Early-type galaxies are the predominant species of galaxy found in dense environments, such as a galaxy cluster (e.g. Hubble & Humason, 1931; Dressler, 1980). Galaxy clusters may have a surface density of galaxies in excess of $2 \times 10^2\,\mathrm{Mpc}^{-2}$, of which an average 40% of galaxy members are elliptical galaxies (Dressler, 1980). Additionally, a morphological gradient of the fraction of galaxies within a cluster exist, with ETGs typically located in the highest density regions, as shown in Fig. 2.9. Conversely, LTGs are typically found in the low density outskirts of galaxy clusters. Galaxies that are located in a dense environment have an increased likelihood of undergoing a merger event with another galaxy of a comparable mass, provided the relative velocities of the two galaxies are low enough for dynamical friction to be effective (§2.2.4) (e.g. Mo et al., 2010). Consequently, merger events are more common within less populous aggregations of galaxies, called groups, compared to high density clusters. If the mass ratio between merging bodies q is less than $3:1$, the event is termed a major merger, and a merger event with mass ratio larger than $3:1$ is termed a minor merger (e.g. Mo et al., 2010). For a merger to occur, the typical timescale for a merger event must be significantly less than the Hubble time t_{H}. The merger timescale is directly related to the major merger frequency R_{mm}, which is unique to each cluster or group. Recent observational measurements of the major merger frequency in the COSMOS field by Xu et al. (2012) indicate both a redshift and mass dependence of the major merger frequency:

$$R_{\mathrm{mm}} = 0.053 \left(\frac{M_\star}{10^{10.7}\,\mathrm{M}_\odot} \right)^{0.3} \frac{(1+z)^{2.2}}{1+\frac{z}{8}} \quad [\mathrm{Gyr}^{-1}], \tag{2.26}$$

implying that large galaxies ($\log(M_\star/\mathrm{M}_\odot) > 10.5$) have undergone multiple major events since redshift $z = 1$, as shown in Fig. 2.10. The minor merger frequency is statistically much higher than the major merger frequency, owing to the few numbers of galaxies within a group of comparable mass, and hence low q. Minor merger events are however more difficult to detect than major merger events, due to the reduced disruption of the larger body by the smaller body.

The merger scenario for elliptical galaxy formation details how an elliptical galaxy is formed during the merging of two massive galaxies of comparable mass (Barnes, 1988; Naab et al., 1999; Bendo & Barnes, 2000; Naab & Burkert, 2003; Johansson et al., 2009a). As elliptical galaxies are typically observed to contain only a single SMBH within the galactic centre, the progenitor SMBHs of the merging galaxies must coalesce. Three key mechanisms to reduce the orbital separation of the SMBHs to coalescence are expected to occur (Begelman et al., 1980), namely:

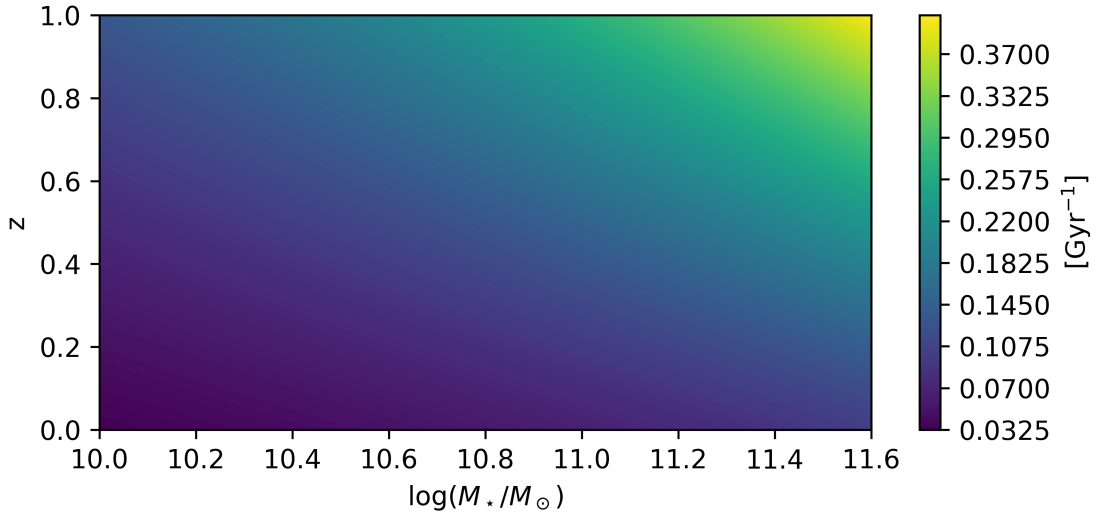

Figure 2.10: Major merger frequency $R_{\rm mm}$ of galaxies in cluster environments following the relation of Xu et al. (2012). Galaxies at high redshift and of large mass have a high major merger frequency than those galaxies of low redshift and mass.

1. Dynamical friction
2. Three-body interactions
3. Gravitational wave (GW) emission

The dominant mechanism of reducing the SMBH binary separation varies with time, dependent on which mechanism has the shortest timescale. Initially, dynamical friction is the most efficient process when the SMBH binary is at large separation, whereas GW emission dominates when the SMBH binary is at sub-parsec separation. The three mechanisms are discussed in depth in §2.2.4 - §2.2.6.

2.2.3 Timescales

During a merger event, the likelihood of a direct collision between two particles, such as stars, is incredibly low, owing to the collision time $t_{\rm direct}$ being much longer than both the relaxation time $t_{\rm relax}$ and the Hubble time $t_{\rm H}$. The time required for a particle to make one orbit of the system, defined as the crossing time $t_{\rm cross}$, is:

$$t_{\rm cross} = \frac{R}{v}, \tag{2.27}$$

where R is the system radius and v the particle velocity (e.g. Binney & Tremaine, 2008). Assuming the particle cross-section to be $\sigma_{\rm d} = \pi r_{\rm p}^2$, where $r_{\rm p}$ is the particle

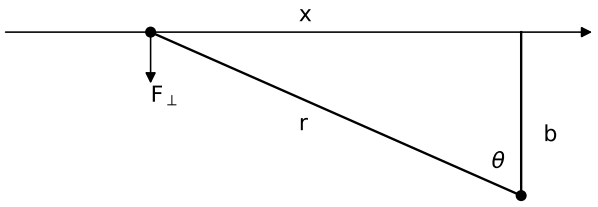

Figure 2.11: A field star moves along a trajectory with velocity v by the subject star, within distance of closest approach b. Figure adapted from Binney & Tremaine (2008).

cross-sectional radius, the mean free path λ of the particles is:

$$\lambda = \frac{1}{n\sigma_{\rm d}} = \frac{4\pi R^3}{3N}\frac{1}{\pi r_{\rm p}^2}, \tag{2.28}$$

where n is the particle number density, and N is the total number of particles. For a direct collision, the timescale is proportional to the particle mean free path:

$$\begin{aligned} t_{\rm direct} = \frac{\lambda}{v} &= \frac{4}{3}\left(\frac{R}{r_{\rm p}}\right)^2 \frac{R}{vN} \\ &\simeq \left(\frac{R}{r_{\rm p}}\right)^2 \frac{t_{\rm cross}}{N}. \end{aligned} \tag{2.29}$$

Assuming a system of stellar particles with identical mass m, an encounter between a particle (the subject particle) moving on a straight-line trajectory past a second stationary particle (the field particle) will experience a force as depicted in Fig. 2.11:

$$F_\perp = \frac{Gm^2}{x^2+b^2}\cos\theta = \frac{Gm^2}{b^2}\left[1+\left(\frac{vt}{b}\right)^2\right]^{-3/2}, \tag{2.30}$$

where b is the impact parameter. Recalling that $\boldsymbol{F} = m\dot{\boldsymbol{v}}$, the velocity perturbation is:

$$\delta v = \frac{Gm}{b^2}\int_{-\infty}^{\infty} \frac{{\rm d}t}{\left[1+(vt/b)^2\right]^{3/2}} = \frac{2Gm}{bv}. \tag{2.31}$$

It is assumed that $\delta v \ll v$, requiring $b > b_{90} \equiv 2Gm/v^2$, where b_{90} is the impact parameter corresponding to a 90° deflection. The number of such encounters that the subject particle experiences is of order:

$$\delta n = \frac{2N}{R^2} b\,{\rm d}b. \tag{2.32}$$

It follows that:

$$\Delta v^2 \equiv \int_{b_{\min}}^{b_{\max}} \sum \delta v^2 \tag{2.33}$$

$$\simeq \int_{b_{\min}}^{b_{\max}} \delta v^2 \delta n \tag{2.34}$$

$$\simeq 8N \left(\frac{Gm}{Rv}\right)^2 \ln \Lambda, \tag{2.35}$$

where $\ln \Lambda \equiv \ln\left(\frac{b_{\max}}{b_{\min}}\right)$ is the Coulomb logarithm (e.g. Binney & Tremaine, 2008). Assuming that the velocity of the field particle is described by:

$$v^2 \approx \frac{Gnm}{R} \implies \frac{\Delta v^2}{v^2} \approx \frac{8 \ln \Lambda}{N}. \tag{2.36}$$

The number of crossings n_{relax} the subject particle experiences before its velocity has changed by order of itself is thus the inverse of Eq. (2.36):

$$n_{\text{relax}} \simeq \frac{N}{8 \ln \Lambda}. \tag{2.37}$$

From the definition of Λ, and taking $b_{\min} \sim b_{90}$ and $b_{\max} \sim R$, the Coulomb logarithm becomes:

$$\ln \Lambda \simeq \ln\left(\frac{Rv^2}{Gm}\right) \tag{2.38}$$

$$\simeq \ln N, \tag{2.39}$$

from Eq. (2.36). Thus, the relaxation time t_{relax} is:

$$t_{\text{relax}} = n_{\text{relax}} t_{\text{cross}} \tag{2.40}$$

$$\simeq \frac{N}{10 \ln N} t_{\text{cross}}, \tag{2.41}$$

where $1/8 \approx 1/10$, as in Binney & Tremaine (2008). Critically, dynamics that occur over a time interval $\delta t \lesssim t_{\text{cross}}$ may be well approximated by a collisionless system:

$$t_{\text{direct}} \gg t_{\text{relax}} \gg t_{\text{H}} \gg t_{\text{cross}}. \tag{2.42}$$

In this work, all stellar dynamics far from a SMBH (see §3.4) are calculated under the assumption of a collisionless system described by a continuous distribution of mass.

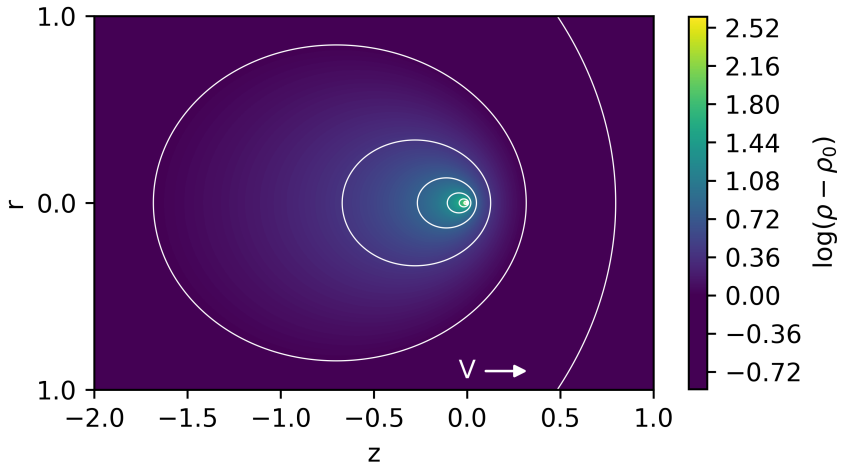

Figure 2.12: Contour plot indicating the fractional enhancement of the local density field $\rho - \rho_0$ as an extended object moves along the z-axis through a background of particles of similar mass. The reference density ρ_0 is set to 1.0, and the background particles have a Maxwellian velocity distribution with the mean velocity to velocity dispersion ratio $V/\sigma = 1.0$. Figure adapted from Mulder (1983).

2.2.4 Dynamical Friction

Following the approach of §2.2.3, dynamical friction is described by studying the motion of a subject particle with mass M_S moving through a collection of collisionless field particles with masses $m \ll M_\mathrm{S}$. As energy and momentum from the subject mass are transferred to the field particles, local enhancements in the density field create a high density 'wake' extending from the subject particle (Fig. 2.12), ultimately reducing the velocity of the subject particle due to the increased gravitational force acting upon it (e.g. Chandrasekhar, 1943; Mulder, 1983; Mo et al., 2010). With the simplifying assumption of a homogeneous number density distribution of field particles, the phase space distribution function $\boldsymbol{f}(\boldsymbol{x}_\mathrm{m}, \boldsymbol{v}_\mathrm{m})$ reduces to $\boldsymbol{f}(\boldsymbol{v}_\mathrm{m})$, where $\boldsymbol{v}_\mathrm{m}$ is the velocity of the field particle. Taking the cumulative change in the subject velocity $\boldsymbol{v}_\mathrm{S}$ to be zero perpendicular to the direction of motion, the cumulative effect of all two body interactions between the field particles and the subject particle may be expressed as:

$$\frac{\mathrm{d}\boldsymbol{v}_\mathrm{S}}{\mathrm{d}t} = \left(\frac{\mathrm{d}\boldsymbol{v}_\mathrm{S}}{\mathrm{d}t}\right)_\parallel = 4\pi G^2 (M_\mathrm{S} + m) m \int \mathrm{d}^3\boldsymbol{v}_\mathrm{m} f(\boldsymbol{v}_\mathrm{m}) \ln\Lambda \frac{\boldsymbol{v}_\mathrm{m} - \boldsymbol{v}_\mathrm{S}}{|\boldsymbol{v}_\mathrm{m} - \boldsymbol{v}_\mathrm{S}|^3}, \tag{2.43}$$

as in Binney & Tremaine (2008). Integrating over velocity space, and assuming isotropy $|\boldsymbol{v}_\mathrm{m}| = v_\mathrm{m}$, the dynamical friction force acting upon the subject particle is

(assuming $m \ll M_{\rm S}$) given by Eq. (2.44):

$$\boldsymbol{F}_{\rm df} = M_{\rm S}\frac{{\rm d}\boldsymbol{v}_{\rm S}}{{\rm d}t} = -16\pi^2 G^2 M_{\rm S}^2 m \ln\Lambda \left[\int_0^{v_{\rm S}} f(v_{\rm m}) v_{\rm m}^2 \, {\rm d}v_{\rm m}\right] \frac{\boldsymbol{v}_{\rm S}}{v_{\rm S}^3}, \tag{2.44}$$

where $\ln(\Lambda)$ is the Coulomb logarithm (see §2.2.3). Eq. (2.44) is known as the Chandrasekhar (1943) dynamical friction formula. It is important to note that Eq. (2.44) does not account for the effect of self-gravity between field particles; the contribution of self-gravity of the field particles is small in the limit $m \ll M_{\rm S}$ (e.g. Binney & Tremaine, 2008). In the case where $v_{\rm S}$ is low, and thus $f(v_{\rm m}) \simeq f(0)$, Eq. (2.44) becomes:

$$\boldsymbol{F}_{\rm df} \simeq -\frac{16\pi^2}{3} G^2 M_{\rm S}^2 m \ln\Lambda f(0) \boldsymbol{v}_{\rm S} \implies F_{\rm df} \propto v_{\rm S}. \tag{2.45}$$

Conversely, in the high $v_{\rm S}$ limit, Eq. (2.44) becomes:

$$\boldsymbol{F}_{\rm df} = -4\pi G^2 M_{\rm S}^2 m n \ln\Lambda \frac{\boldsymbol{v}_{\rm S}}{v_{\rm S}^3} \implies F_{\rm df} \propto v_{\rm S}^{-2}, \tag{2.46}$$

where n is the number density of the field particles. Consequently, dynamical friction is more efficient when the velocity of the subject particle is low compared to when the subject velocity is high. In the instance where the subject particle is a SMBH with mass $M_\bullet$ moving against a background of stellar particles with mass $m \ll M_\bullet$, the dynamical friction force acts as a mass segregation mechanism. The result is the orbital decay of the SMBH to the centre of the gravitational potential well of the system (e.g. Binney & Tremaine, 2008). To understand why a SMBH is most likely to be found at the centre of the potential well of the system, consider a SMBH moving on a circular orbit with radius r within a density distribution given by:

$$\rho(r) = \frac{v_c^2}{4\pi G r^2}, \tag{2.47}$$

from which the frictional force $F_{\rm df}$ is found to be:

$$F_{\rm df} = 0.428 \ln\Lambda \frac{G M_\bullet^2}{r^2}. \tag{2.48}$$

The SMBH loses angular momentum L at a rate proportional to the frictional force

$$\frac{{\rm d}L}{{\rm d}t} = -F_{\rm df} r \propto \frac{M_\bullet^2}{r}, \tag{2.49}$$

as $\boldsymbol{F}_{\rm df}$ is tangential and directed opposite to the constant orbital velocity v_c of the SMBH as it traverses a nearly-circular orbit during its inspiral (Binney & Tremaine, 2008). Taking $L = M_\bullet r v_c$, Eq, (2.49) becomes:

$$r\frac{{\rm d}r}{{\rm d}t} = -0.428 \ln\Lambda \frac{G M_\bullet}{v_c}. \tag{2.50}$$

The solution of the differential equation found by integration dictates that the SMBH reaches the system centre within a time:

$$t_{\rm df} = \frac{1.17}{\ln \Lambda} \frac{M(r)}{M_\bullet} t_{\rm cross} \ll t_{\rm H}, \tag{2.51}$$

where the mass interior to the SMBH is given by $M(r) \equiv v_c^2 r/G$. Thus, the SMBH is expected to be found at the centre of the system (e.g. Binney & Tremaine, 2008). If the SMBH is on an eccentric orbit, the inspiral time is further reduced as result of the SMBH more frequently passing through regions with an enhanced local density, and thus enhanced dynamical friction force (White, 1976).

In the instance of two SMBHs within the system due to a merger event, a SMBH binary will form (e.g. Binney & Tremaine, 2008). The SMBH binary orbit continues to shrink via dynamical friction, corresponding to an increase in the relative orbital velocity v. When the relative orbital velocity v of the binary exceeds the background stellar velocity dispersion $\sigma_\star$, the binary is termed a 'hard' binary (e.g. Merritt, 2013). A hard binary occurs when the SMBH binary semimajor axis is:

$$a_{\rm h} = \frac{G\mu}{4\sigma_\star^2}, \tag{2.52}$$

where

$$\mu \equiv \frac{M_{\bullet,1} M_{\bullet,2}}{(M_{\bullet,1} + M_{\bullet,2})} \tag{2.53}$$

is the reduced mass of the binary.

2.2.5 Three-Body Interactions

Dynamical friction ceases to be the primary mechanism of orbital decay shortly prior to the SMBH binary hardening, with three-body interactions now assuming dominance (e.g. Merritt, 2013). Qualitatively, three-body interactions may be described as an encounter between a stellar particle and the SMBH binary that results in the stellar particle being ejected from the interaction on a hyperbolic orbit with ejection velocity comparable to the SMBH binary orbital velocity (e.g. Milosavljević & Merritt, 2003):

$$v_{\rm ej} \sim \sqrt{\frac{G(M_{\bullet,1} + M_{\bullet,2})}{a}} \gg \sigma_\star, \tag{2.54}$$

where a is the binary semimajor axis. The ejected stellar particle effectively gains a fraction of the binary energy and angular momentum (e.g. Hills & Fullerton, 1980); the binary semimajor axis decreases. Critically, only stars with an orbital angular

momentum L that satisfies:

$$m_\star L \lesssim [G(M_{\bullet,1} + M_{\bullet,2})a]^{1/2}\,, \tag{2.55}$$

may undergo strong interactions with the SMBH binary (e.g. Binney & Tremaine, 2008). Stellar particles which satisfy Eq. (2.55) belong to the region of phase space termed the loss cone (e.g. Merritt, 2013). The evolution of the SMBH binary orbit can be described by a semi-analytic model (e.g. Quinlan, 1996; Sesana, 2010), where the inverse SMBH binary semimajor axis $1/a$ evolves as:

$$\frac{\mathrm{d}}{\mathrm{d}t}\left(\frac{1}{a}\right) = \frac{G\rho}{\sigma_\star}H, \tag{2.56}$$

and the orbital eccentricity e of the SMBH binary evolves with the semimajor axis of the binary as:

$$\frac{\mathrm{d}e}{\mathrm{d}t} = K\frac{G\rho}{\sigma_\star}Ha. \tag{2.57}$$

Here, K and H are constants from three-body experiments (Quinlan, 1996; Sesana, 2010) and ρ is the stellar density. Consequently, orbital eccentricity is expected to increase as the SMBH binary experiences more three-body encounters (e.g. Valtonen & Mikkola, 1991; Ryu et al., 2018; Mannerkoski et al., 2019). Three-body scattering experiments by Sesana et al. (2011) indicate that binary eccentricity is driven to higher values more rapidly if the surrounding stellar population is counter-rotating with respect to the SMBH binary motion. If the stellar population immediate to the binary is co-rotating with respect to the binary, the opposite effect is observed, whereby the binary eccentricity is circularised (Sesana et al., 2011). By the time the semimajor axis of the SMBH binary has reduced to $a = a_\mathrm{h}$, the relinquished energy of the binary is of order:

$$\Delta E \approx -\frac{GM_{\bullet,1}M_{\bullet,2}}{2r_\mathrm{h}} + \frac{GM_{\bullet,1}M_{\bullet,2}}{2a_\mathrm{h}} \approx 2(M_{\bullet,1} + M_{\bullet,2})\sigma_\star^2. \tag{2.58}$$

The SMBH binary typically transfers an energy proportional to the combined SMBH masses $M_{\bullet,1} + M_{\bullet,2}$ to the stellar particles within the loss cone. Consequently, the binary displaces a stellar mass comparable to the binary mass (Merritt, 2006). As stellar particles within the loss cone interact with the SMBH binary and the binary separation reduces, the loss cone becomes depleted. The depletion of the loss cone is visible in the evolution of the radius of the sphere of influence r_SOI about the SMBH binary:

$$r_\mathrm{SOI} = \frac{GM_\bullet}{\sigma_\star^2}. \tag{2.59}$$

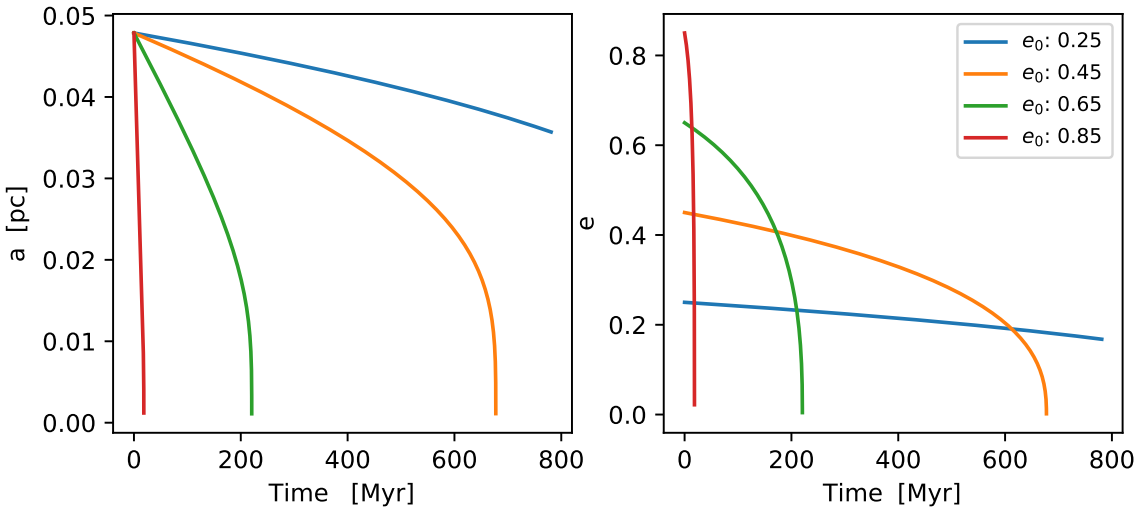

Figure 2.13: Numerical solution of Peters (1964) to an equal mass ($M_\bullet = 10^8\,\mathrm{M}_\odot$) SMBH binary coalescence for a fixed initial semimajor axis $a_0 = 4.79 \times 10^{-2}\,\mathrm{pc}$ at four different initial orbital eccentricities e_0. High initial eccentricities lead to much more rapid merging of the binary compared to low initial eccentricities. Additionally, the eccentricity of the binary orbit decreases as GW emission occurs.

The sphere of influence encloses a stellar mass approximately equal to an individual SMBH mass, assuming the binary has a sufficiently large separation. If the SMBH binary mass exceeds the mass of stellar particles within the loss cone, the loss cone may be fully exhausted of stellar particles (e.g. Binney & Tremaine, 2008). The result of loss cone exhaustion is a stalling of the SMBH binary hardening rate. The SMBH binary separation may continue to decrease if the loss cone is refilled via dynamical processes, such as diffusion of angular momentum, or torques if the galaxy is non-axisymmetric (e.g. Berczik et al., 2006; Vasiliev et al., 2015) or contains gas (Mayer et al., 2007; Mayer, 2013).

2.2.6 Gravitational Waves

If the loss cone is not depleted prior to the semimajor axis of the SMBH binary reducing to scales ($a \lesssim 0.1\,\mathrm{pc}$ for $M_\bullet \sim 10^8\,\mathrm{M}_\odot$), the binary will be driven to coalescence through GW emission (Peters & Mathews, 1963; Peters, 1964). In the sub-parsec regime, the final evolution of the SMBH binary may be well approximated as an isolated system. Using the first dissipative term (PN2.5) in the Post-Newtonian approximation to general relativity (discussed in §2.5), the time-averaged Keplerian

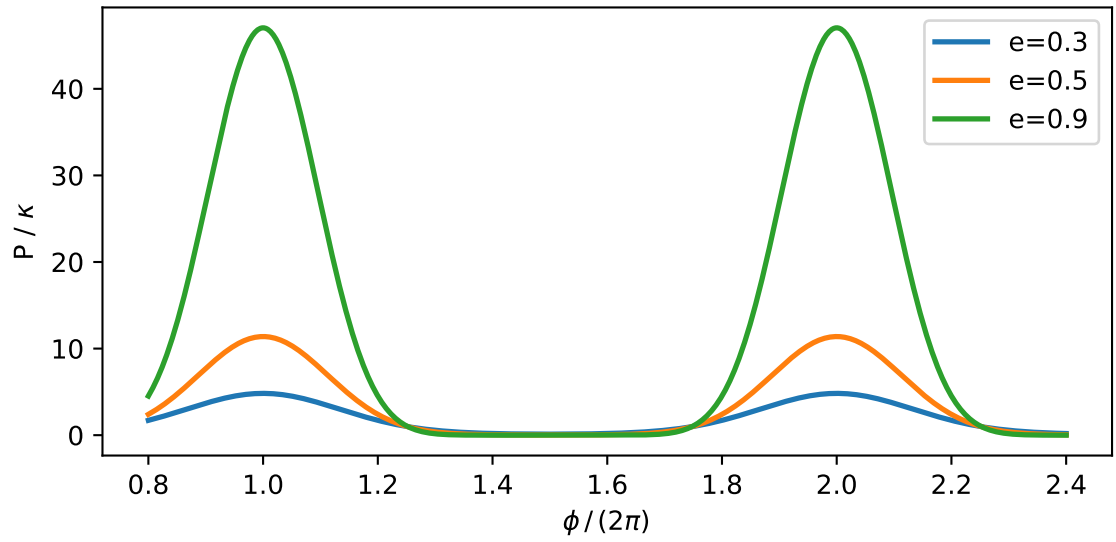

Figure 2.14: Radiated energy P from GW emission (Eq. (2.62)) in units of $\kappa = \left[32G^4 M_{\bullet,1}^2 M_{\bullet,2}^2 (M_{\bullet,1} + M_{\bullet,2})\right] / \left[5c^5 a^5 (1-e^2)^5\right]$ as a function of normalised orbital angle ϕ. The radiated energy peaks at integer values of $\phi/(2\pi)$, coinciding with the pericentre of the orbit where the velocity is greatest. Higher eccentricity orbits radiate more energy than lower eccentricity orbits.

orbital parameters evolve as described by Peters (1964):

$$\left\langle \frac{\mathrm{d}a}{\mathrm{d}t} \right\rangle = -\frac{64}{5} \frac{G^3 M_{\bullet,1} M_{\bullet,2} (M_{\bullet,1} + M_{\bullet,2})}{c^5 a^3 (1-e^2)^{7/2}} \left(1 + \frac{73}{24} e^2 + \frac{37}{96} e^4\right), \tag{2.60}$$

$$\left\langle \frac{\mathrm{d}e}{\mathrm{d}t} \right\rangle = -\frac{304}{15} \frac{G^3 M_{\bullet,1} M_{\bullet,2} (M_{\bullet,1} + M_{\bullet,2})}{c^5 a^4 (1-e^2)^{5/2}} e \left(1 + \frac{121}{304} e^2\right), \tag{2.61}$$

and are shown in Fig. 2.13. From Eq. (2.61), the eccentricity e evolution rate is a function of both semimajor axis a and e, and thus GW emission drives a SMBH binary on a highly eccentric orbit to circularity just prior to merging (Sesana, 2010). The circularisation of the binary orbit can be understood in terms of the radiated power due to GW emission. Without loss of generality the treatment of the orbital motion of the SMBH binary is restricted to a plane of constant latitude ($\mathrm{d}\theta = 0$). Defining the angular coordinates r and ϕ such that $r\ddot{r} = (r\dot{\phi})^2 - G(M_{\bullet,1} + M_{\bullet,2})/r$, the instantaneous radiated energy P and angular momentum flux T^{xy} from GW emission is:

$$P = \frac{32G^4}{5c^5} \frac{M_{\bullet,1}^2 M_{\bullet,2}^2 (M_{\bullet,1} + M_{\bullet,2})}{a^5 (1-e^2)^5} (1 + e\cos\phi)^4 \left[1 + 2e\cos\phi + \frac{e^2}{12}(1 + 11\cos^2\phi)\right], \tag{2.62}$$

and

$$T^{xy} = \frac{32}{5}\frac{G^{7/2}M_{\bullet,1}^2 M_{\bullet,2}^2 (M_{\bullet,1}+M_{\bullet,2})^{1/2}}{c^5 a^{7/2}\left(1-e^2\right)^{7/2}}(1+e\cos\phi)^3\left[1+\frac{3}{2}e\cos\phi-\frac{1}{4}e^2\left(1-3\cos^2\phi\right)\right], \tag{2.63}$$

respectively, as in Poisson & Will (2014). In the case of $e = 0$, the power P is related to the angular momentum flux as $P = \Omega T^{xy}$, where Ω is the orbital angular velocity. In Fig. 2.14 it is shown that the most energy is radiated at periapsis, where the angular coordinate $\phi = 2\pi$ and the orbital velocity is greatest. More energy (and angular momentum) is radiated at periapsis than at apoapsis, resulting in a lowering of orbital eccentricity and overall circularisation of the binary orbit (Peters & Mathews, 1963). Furthermore, a SMBH binary with an initially high eccentricity orbit will merge more rapidly than a binary with an initially low eccentricity orbit due to a reduced periapsis distance and increased energy emission (see Fig. 2.14), assuming that GW emission is the sole mechanism of orbital decay (see Fig. 2.13) (Peters, 1964). The gravitational radiation timescale is given as (Peters, 1964; Yu, 2002):

$$t_{\rm gr}(a) = \left|\frac{a}{\dot{a}}\right| = \frac{5}{64}\frac{c^5 a^4 (1-e^2)^{7/2}}{G^3\mu(M_{\bullet,1}+M_{\bullet,2})^2\left(1+73e^2/24+37e^4/96\right)} \tag{2.64}$$

where μ is the reduced mass given by Eq. (2.53).

For a physical system in which the effects of dynamical friction and three-body interactions cannot be ignored, the actual orbital decay time is determined by the more efficient of dynamical friction and GW emission (refer to §2.2.3). The maximum decay time coincides with the radius at which the decay time due to dynamical friction and the decay time due to GW emission are equal, and is often termed the bottleneck radius (Begelman et al., 1980; Yu, 2002). SMBH binary systems are expected to reside at the bottleneck radius for the majority of the binary lifetime (e.g. Binney & Tremaine, 2008), introducing a constraint for the existence of SMBH binaries. If the bottleneck timescale is longer than a Hubble time, SMBH binaries should be widely observed.

2.2.7 Observational Constraints of Gravitational Waves

Strong evidence for the merging of SMBH binary systems is expected from gravitational wave detection from ongoing pulsar timing arrays (PTA) and the upcoming Laser Interferometer Space Antenna (LISA).

The PTA methodology examines the timing residuals measured from highly-regularised pulses emitted from millisecond pulsars compared to theoretical timing

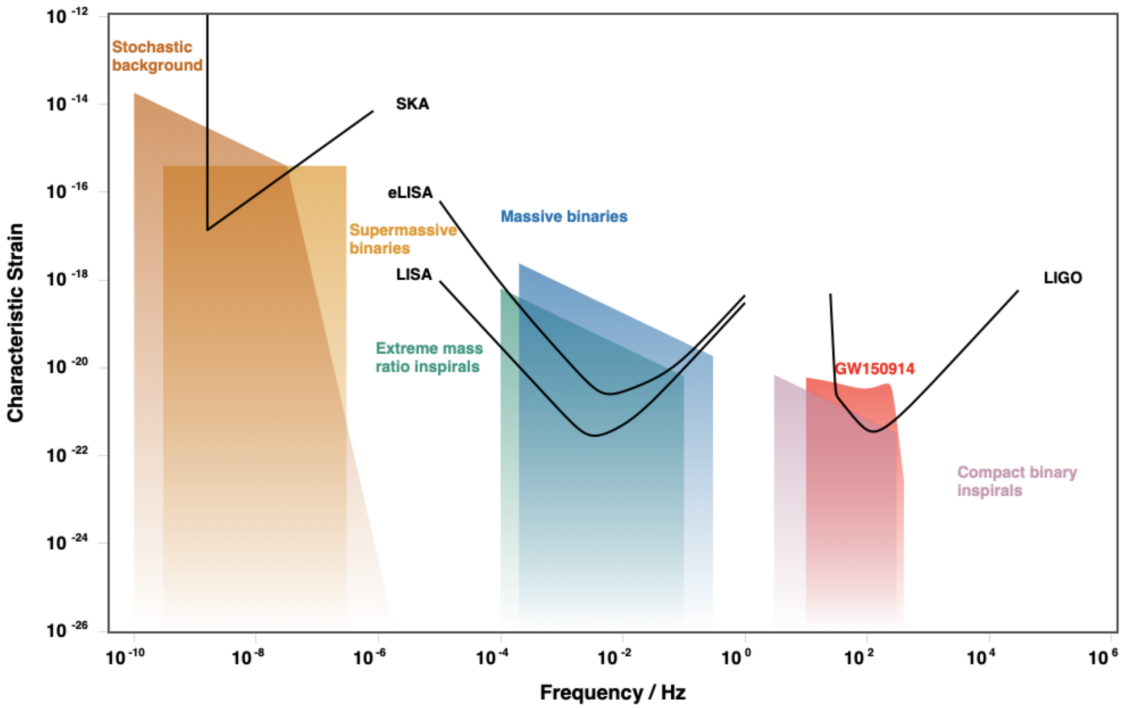

Figure 2.15: Sensitivity of various observation methods and instruments to different GW emission sources. Of particular relevance, massive SMBH binaries are expected to be within the sensitivity threshold of LISA, whereas supermassive SMBH binaries are expected to be within the sensitivity threshold of the SKA. Image produced with software from Moore et al. (2015).

predictions (e.g. Detweiler, 1979; Edwards et al., 2006). Low frequency GW emission, such as that emitted by SMBH binaries with $M_{\bullet,1} \simeq M_{\bullet,2} \gtrsim 10^9\,\mathrm{M}_\odot$ (Fig. 2.15), is expected to be visible as a correlation in the timing residuals of the pulsars (Sazhin, 1978; Detweiler, 1979). Modelling by Jenet et al. (2005) indicates that approximately twenty pulsars, each with timing measurements of 100 nanosecond precision, are required to be observed for five years to remove the measurement stochasticity associated with propagation effects through the interstellar medium (ISM) and irregular pulsar rotation. Such measurements will be a primary goal of the upcoming Square Kilometre Array (SKA) (Cordes et al., 2004), anticipated to come online by the end of this decade. Other PTA projects, such as the North American Nanohertz Observatory for Gravitational Waves (NANOgrav) have already been in operation for more than twelve years. Much of the work to date has been to calibrate for the stochastic background in the PTA signal, however gravitational wave detections are fast-approaching. The first tentative signal in PTA data has been announced by Arzoumanian et al. (2020), though the origin of the signal and the event that caused it cannot be concluded at present. A number of

candidate events that are astrophysical in nature have been suggested by the authors, including primordial GWs from inflation, cosmic strings, and merging SMBH binaries.

The upcoming LISA mission (Amaro-Seoane et al., 2017) will use three satellites in a near-equilateral triangle configuration as the basis of a laser interferometer to detect GW emission from e.g. massive black hole binaries ($10^6\,\mathrm{M}_\odot \lesssim M_{\bullet,1} \simeq M_{\bullet,2} \lesssim 10^9\,\mathrm{M}_\odot$). The peak LISA sensitivity occurs at a frequency of $\sim 10^{-2}\,\mathrm{Hz}$ ($M_\bullet \sim 10^6\,\mathrm{M}_\odot$–$10^8\,\mathrm{M}_\odot$). Consequently, LISA will be well suited for the study of massive black hole binary inspirals during the merger of low-medium mass elliptical galaxies and disc galaxies (Amaro-Seoane et al., 2017).

2.3 The Final Parsec Problem

In numerical studies of isolated galaxy mergers, the SMBH binary can successfully coalesce only if the GW emission regime is reached, requiring that the binary semimajor axis decrease to sub-parsec lengths. The three-body interaction regime presents the greatest challenge in reaching the GW emission regime, due to the emptying of the loss cone and consequent stalling of the binary merger. The inability of a stalled SMBH binary to merge is referred to as the Final Parsec Problem (FPP) (Milosavljević & Merritt, 2001). Whether the FPP is a physical phenomenon or a numerical artefact has been a hotly-debated issue. The lack of observed SMBH binary systems suggests that SMBH binary merging should occur in a timescale less than the Hubble time. The FPP has been investigated in a number of studies, each with different model assumptions; some of the major studies are presented in brief in §2.3.1. Importantly, only in select works, primarily Rantala et al. (2017, 2018, 2019) were the SMBH binary systems able to be integrated to sub-parsec separation in a global galactic setting, and not merged through extrapolation (e.g. Escala et al., 2004). As a result of limitations of mass resolution, not all previous studies of the FPP are therefore confidently converged (e.g. Vasiliev et al., 2014).

As discussed in §2.2.3, if the collision timescale of stellar particles is much greater than the Hubble time, a galaxy may be modelled as a collisionless system. In collisionless studies, gas must be excluded from the system, as gas is described as a hydrodynamical fluid which is not solely governed by gravitational interaction (e.g. Mo et al., 2010). As the cold gas component in massive ETGs is negligible at small galactocentric radii, ETGs may be appropriately modelled as a collisionless system (e.g. Mo et al., 2010).

2.3.1 Previous Studies

Investigations of the FPP that do not incorporate gas dynamics may be broadly divided into two categories: those which had two SMBHs placed in a single, isolated galaxy system, and those which involved the merging of two initially distinct galactic systems. For models of the former category, the FPP is seen to arise in systems which are axisymmetric; such studies include Milosavljević & Merritt (2001), Makino & Funato (2004), and Vasiliev et al. (2015). Milosavljević & Merritt (2001) argue that the emptying of the loss cone is most likely to be prevalent in massive ETGs, such as cD galaxies. In idealised, axisymmetric galaxies, the loss cone may only be repopulated through two-body relaxation of the stellar particles, leading to a loss cone refilling timescale in excess of the Hubble time (e.g. Vasiliev et al., 2015). Makino & Funato (2004) suggest that gas dynamics might be able to resolve the loss cone depletion.

In isolated, non-idealised, triaxial systems, the loss cone may be repopulated by mechanisms additional to two-body relaxation, such as large-scale torques (Merritt & Poon, 2004). Studies by Berczik et al. (2006), Vasiliev et al. (2015), and Gualandris et al. (2017) did not encounter a stalling of the SMBH binary hardening rate, thus allowing the SMBHs to merge. In the case of Gualandris et al. (2017), the SMBH binary was assumed to merge by gravitational radiation when the binary semimajor axis became:

$$a_{\rm GW} \approx 2 \times 10^{-3} \left(\frac{M_{\bullet,1} + M_{\bullet,2}}{10^6\,{\rm M}_\odot} \right)^{3/4} \ {\rm pc}. \tag{2.65}$$

Stalling of the SMBH binary was also not observed by Berentzen et al. (2009) in models of triaxial galaxies including Post-Newtonian (PN) corrections (§2.5) up to order of 2.5. Furthermore, eccentricity is expected to be an important factor in overcoming the FPP in the collisionless merger studies. A SMBH binary on a highly eccentric orbit has the ability to interact with a greater number of stars compared to a SMBH binary on a circular orbit (Quinlan, 1996); highly eccentric binaries are observed by Khan et al. (2011) and Rantala et al. (2017), though this in part due to the initial orbital configuration of both systems. Non-physical merging of SMBHs binaries has been found to occur through Brownian motion at low resolution ($N \simeq 6.4 \times 10^4$), whereby the loss cone of some binary systems is artificially repopulated by the random wandering of the binary system (Merritt, 2001; Bortolas et al., 2016). The numerical artefact of Brownian motion may be negated by using a sufficiently high number of stellar particles, typically taken to be $N \sim 10^6$ (Bortolas et al., 2016).

The effect of host galaxy axisymmetry or triaxiality may be neglected in studies where two galaxies were merged, compared to two SMBHs being placed within a single system. During the merger event, the effects of dynamical friction dictates the resulting merger system is necessarily triaxial and chaotic (e.g. Khan et al., 2011). In the studies of Rantala et al. (2017, 2018, 2019) and Ryu et al. (2018), the loss cone was at no stage depleted, and the SMBH binary formed from the galactic interactions able to merge. The afore-mentioned studies also included PN corrections, unlike the study of Khan et al. (2011); the triaxiality of the merger remnants of Khan et al. (2011) are sufficient to ensure the SMBH binary is brought to within an orbital separation where coalescence is inevitable.

The study of the FPP has also been performed in the context of simulations that incorporate gas. Typically, such studies model the merging of disc or ultra-luminous infrared galaxies (ULIRGs) where the gas component may not be neglected (e.g. Mo et al., 2010). Large scale cosmological studies typically set a SMBH merging criterion as:

1. The binary separation reduces below the spatial resolution of the simulation, and

2. The relative velocity of the SMBH binary is below the sound speed of the gas,

as in Springel (2005) and Di Matteo et al. (2008). In studies of two progenitor galaxies merging, the SMBH binary coalesced in the works of Escala et al. (2004) and Mayer et al. (2007). The binary was merged when the semimajor axis was 0.1 pc in Escala et al. (2004), and 2.0 pc in Mayer et al. (2007). Torques from a gaseous disc about an equal-mass ($M_\bullet \lesssim 10^7\,\mathrm{M}_\odot$) SMBH binary in the study of Cuadra et al. (2009) were a viable mechanism for SMBH binary coalescence. For SMBH masses $M_\bullet \gtrsim 10^7\,\mathrm{M}_\odot$, a gaseous disc was unable to result in the SMBHs merging, however Cuadra et al. (2009) suggest that repopulation of the loss cone by stellar particles scattered by the fragmenting disc may induce SMBH coalescence.

2.4 Algorithmic-Regularisation

Close encounters between particles in numerical simulations of galactic-scale mergers are of particular importance for binary systems involving a SMBH, such as three-body encounters and the final pre-gravitational wave regime of the SMBH binary. Such encounters involve very large accelerations, requiring highly-accurate calculation with small timesteps (e.g. Mikkola & Merritt, 2008). A simple solution to

ensure accurate force calculation is to reduce the particle softening length ϵ (further discussed in §3.3). Two negative consequences of arbitrarily small softening lengths are:

1. Non-Newtonian dynamics at scales shorter than the softening length, and

2. Adaptive time-stepping (see §3.4.2) increases with close encounters, potentially stalling the simulation as the timestep $\Delta t \to 0$.

An alternative solution to ensure accurate force computation lies in the removal of the coordinate singularity in the force calculation (Eq. (1.1)) by coordinate regularisation. Regularisation ensures all dynamical quantities remain finite during a collision, albeit at the expense of computational time (e.g. Aarseth, 2003). A number of regularisation schemes exist, such as the Levi-Civita and Kustaanheimo-Stiefel (KS) schemes (e.g. Aarseth, 2003). The regularisation scheme used in the studies by this work is the minimum spanning tree algorithmic regularisation (MSTAR) (Rantala et al., 2020), which has its origins in the algorithmic-regularisation chain (AR-CHAIN) method (Mikkola & Aarseth, 2002; Mikkola & Merritt, 2008). The AR-CHAIN method uses a time transformation and leapfrog integrator, a chained coordinate system, and an extrapolation algorithm to obtain high numerical accuracy (Mikkola & Aarseth, 2002; Rantala et al., 2017). The time transformation is discussed below, and the chained coordinate system, extrapolation algorithm, and integrator are discussed in §3.4.2-§3.4.8.

The time transformation of the dynamical system takes a fictitious time s which is parameterised by a regularisation triplet (α, β, γ) as:

$$\mathrm{d}s = [\alpha(T + B) + \beta\omega + \gamma]\mathrm{d}t, \tag{2.66}$$

where T is the kinetic and B the binding energy of the system, and ω a velocity-like variable of the coordinates $\boldsymbol{r}$ defined by Rantala et al. (2017) as:

$$\omega(0) = \Omega(\{\boldsymbol{r}_i\}) \tag{2.67}$$

$$\frac{\mathrm{d}\omega}{\mathrm{d}t} = \sum_i^N \nabla_{\boldsymbol{r}_i}\Omega \cdot \boldsymbol{v}_i. \tag{2.68}$$

In Eq. (2.67), the variable Ω is defined following Mikkola & Merritt (2006) as:

$$\Omega = \sum_i^N \sum_{j>i}^N \frac{\Omega_{ij}}{|\boldsymbol{r}_{ij}|}, \tag{2.69}$$

where

$$\Omega_{ij} = \begin{cases} \tilde{m}^2, & m_i m_j < \epsilon_\Omega \tilde{m} \\ 0 & \text{otherwise} \end{cases} \tag{2.70}$$

and

$$\tilde{m} = \frac{2}{N(N-1)} \sum_{i}^{N} \sum_{j>i}^{N} m_i m_j, \tag{2.71}$$

with ϵ_Ω of order $\sim 10^{-3}$ (Rantala et al., 2017). The optimal regularisation method is achieved with a choice of $(\alpha, \beta, \gamma) = (1, 0, 0)$ (Mikkola & Merritt, 2008), corresponding to the logarithmic Hamiltonian regularisation of Mikkola & Tanikawa (1999). The calculation for ω and Ω can still be performed in this instance, though is not used in MSTAR (Mikkola & Aarseth, 2002; Rantala et al., 2017).

2.5 Post-Newtonian Dynamics

Due to the extreme distortion of spacetime about any black hole, general relativistic effects must be accounted for in the treatment of a SMBH binary system. In general relativity (GR), gravity is a geometric property arising from the spacetime distortion as described by the Einstein field equations (e.g. Carroll, 2004):

$$R_{\mu\nu} - \frac{1}{2} R g_{\mu\nu} + \Lambda g_{\mu\nu} = \frac{8\pi G}{c^4} T_{\mu\nu}, \tag{2.72}$$

where $R_{\mu\nu} \equiv R^{\alpha}_{\mu\alpha\nu}$ is the Ricci tensor, formed from the contraction over the first and third indices of the Riemann tensor, and $R \equiv g^{\mu\nu} R_{\mu\nu}$ the Ricci scalar. Both $R_{\mu\nu}$ and R derive from the metric $g_{\mu\nu}$ through the Levi-Civita connection, and thus describe the departure of spacetime from the flat, Minkowski metric $\eta_{\mu\nu}$, i.e. how spacetime curves in the presence of mass. Additionally, Λ in Eq. (2.72) is the cosmological constant describing the energy density of the vacuum, and $T_{\mu\nu}$ the energy-momentum tensor that describes the flux of the μ-component of momentum through a surface with x^ν constant (e.g. Carroll, 2004). Eq. (2.72) yields ten equations involving the metric, its derivative in the form of the Levi-Civita connection, and the second derivative of the metric in the form of the Riemann tensor. Each equation is also non-linear, so that the superposition of two solutions may not be used to find a third. Solving Eq. (2.72) for the long-term evolution of a SMBH binary spacetime is computationally infeasible; approximations to the GR treatment of distorted spacetimes are required.

Widely used are the Post-Newtonian (PN) corrections, which extend regular Newtonian dynamics to approximate relativistic effects. The PN approximation may

be used in the weak-field limit of GR, and most effectively between two bodies (e.g Poisson & Will, 2014). The PN corrections become progressively inaccurate as the orbital separation of the two bodies reduces (e.g. Mora & Will, 2004). Restricting the treatment to low velocities:

$$\frac{v}{c} \ll 1, \tag{2.73}$$

additional terms may be added to the Newtonian acceleration $\boldsymbol{a}_{\mathrm{N}}$ to construct the PN-description:

$$\boldsymbol{a} = \boldsymbol{a}_{\mathrm{N}} + \boldsymbol{a}_{\mathrm{PN1}} + \boldsymbol{a}_{\mathrm{PN2}} + \boldsymbol{a}_{\mathrm{PN2.5}} + \boldsymbol{a}_{\mathrm{PN3}} + \boldsymbol{a}_{\mathrm{PN3.5}}, \tag{2.74}$$

where $\boldsymbol{a}_{\mathrm{N}}$ is the regular Newtonian acceleration calculated between all particles, and the terms $\boldsymbol{a}_{\mathrm{PN}i}$ are calculated between the two bodies in question, i.e. the SMBH binary. Each PN term in Eq. (2.74) is labelled (e.g. Mannerkoski et al., 2019) such that:

$$|\boldsymbol{a}_{\mathrm{PN}i}| \propto \epsilon^i_{\mathrm{PN}} \sim \left(\frac{v}{c}\right)^{2i} \sim \left(\frac{R_{\mathrm{s}}}{r}\right)^{i}, \tag{2.75}$$

where ϵ^i_{PN} is the formal PN expansion parameter, v the relative velocity and r the relative separation of the SMBH binary, and R_s the Schwarzschild radius from Eq. (2.21). The PN terms with integer i allow for conservative quantities such as energy and angular momentum, whereas half-integer PN terms correspond to non-conservative dissipative effects arising from GW emission (e.g. Mora & Will, 2004; Poisson & Will, 2014; Mannerkoski et al., 2019). Consequently, PN corrections up to and including PN2.5 are required to model the GW-driven inspiral of the SMBH binary, with PN3.5 ideally included as well.

It should be noted that the PN treatment of the SMBH binary can include a term $\boldsymbol{a}_{\mathrm{S}}$ that describes the contribution of particle spin to the spacetime distortion. If neither binary member displays spin, or the spins of both binary members are orientated perpendicular to the orbital plane, the orbital plane will remain fixed in space (e.g. Kidder, 1995). Conversely, if one or both binary members have spins not aligned with the orbital plane, the orbital plane will precess as a result of spin-orbit coupling, and thus affect the observed gravitational waveform as measured by an observer. Additionally, precession of the spin of the body may be induced by spin-spin coupling, again altering the observed waveform (e.g. Kidder, 1995). The contribution of spin effects are small, with spin-orbit coupling effectively an order 1.5PN effect, and spin-spin coupling effectively of order 2PN (e.g. Kidder, 1995; Mora & Will, 2004). In this work, all black holes are assumed to be non-spinning Schwarzschild black holes.

3. Solving the N-Body Problem

This chapter provides a brief background to the simulation code KETJU developed by Rantala et al. (2017) used for the thesis investigation. The KETJU code is a hybrid code that allows for calculating both the large-scale dynamics, using the code GADGET-3 (Springel, 2005), and accurately following the small-scale dynamics in a small region about a SMBH using an algorithmic regularisation technique (AR, §2.4). Particles outside the AR region are propagated with GADGET-3, and are represented by softened gravitational potentials, whereas those particles within the AR region are not softened: the force calculation is limited only by the mass resolution of the simulation.

For typical galactic-scale N-body simulations, physical particles (some 10^{11} stars for a typical galaxy) cannot have individually-resolved dynamics due to computational efficiency, with integration methods typically scaling as $\mathcal{O}(N \ln N)$. Accordingly, a system is represented as a collection of simulation particles which are sampled from a mass density distribution (§4.1.4-§4.2), with individual particle masses some orders of magnitude larger than an individual physical particle. Increasing the number of simulation particles improves the resolution at which the dynamics are resolved, however this comes at the cost of computational time.

3.1 Overview

Evolving a collisionless dynamical system comprises of two general steps:

1. Calculation of the gravitational potential $\Phi_i(r_i)$ acting on all particles to determine the particle accelerations, and

2. Integration of the equation of motion to determine the updated position and velocity of each particle,

$$\ddot{\boldsymbol{r}}_i = -\nabla_i \Phi_i(\boldsymbol{r}_i). \tag{3.1}$$

In practice for methods other than the particle-mesh method, the acceleration $\ddot{\boldsymbol{r}}$ is calculated directly and the potential $\Phi_i(r_i)$ only when required. Maintaining generality, an intuitive method to determine the potential is direct summation, or the particle-particle (PP) method, i.e.:

$$\Phi(\boldsymbol{r}_i) = -G \sum_{j,\, j \neq i}^{N} \frac{m_j}{|\boldsymbol{r}_i - \boldsymbol{r}_j|}. \tag{3.2}$$

As for every particle the force calculation is the superposition of individual forces from every other particle, the computational complexity of Eq. (3.2) scales as $\mathcal{O}(N^2)$, thus limiting the number of system particles able to be used in typical high-resolution calculations to $N \sim 10^6$ (e.g. Wang et al., 2015). Thus, approximative methods for the force calculation are required, with an approximation chosen after considering the need for accurate dynamics against computational expense.

A large class of N-body simulations employ a particle-mesh (PM) technique to determine the gravitational potential, whereby the simulation particles are further discretised by representing the simulation particle density field on a grid. The Poisson equation:

$$\nabla^2 \Phi = 4\pi G \rho \tag{3.3}$$

is then employed to compute the potential from the mesh using e.g. Fast-Fourier Transform (FFT) techniques, from which the force at the original simulation particle position is computed. Performance improvement is achieved by using multiple grids of differing resolutions (multigrid techniques), or adaptive mesh refinement (AMR) techniques (e.g. Teyssier, 2002). Alternatively, the system space may be decomposed into regions where the integration is performed using a PP method for high accuracy small-scale dynamics, coupled with a PM method for integrations of lower accuracy for more distant forces (P^3M).

An alternative to PM methods is the tree code approach first developed by Barnes & Hut (1986). A hybrid TreePM method is the basis of the widely successful GADGET-3 code (Springel, 2005), into which KETJU is integrated (§3.4). GADGET-3 combines the efficiency of the tree code for collisionless N-body simulations with smoothed particle hydrodynamics (SPH) for modelling gas, thus allowing the code to be applied to a variety of different astrophysical settings.

3.2 Tree Code

The tree code (Barnes & Hut, 1986) relies on the multipole expansion to approximate the gravitational force acting on a subject particle from a distant group of particles

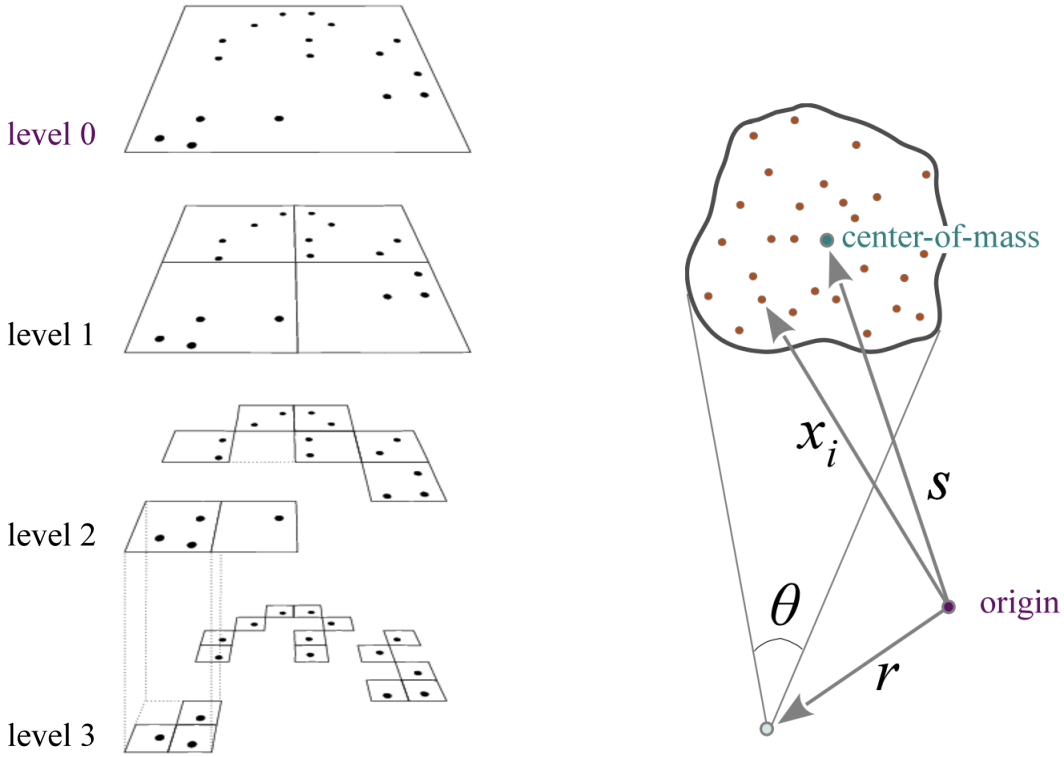

(a) Tree decomposition in two-dimensions.

(b) Tree opening angle criteria.

Figure 3.1: Key concepts of the tree code method of Barnes & Hut (1986). Figures are reproduced from Springel (2016) (their Figs. 15 and 14).

as originating from a single 'source'. The simulation domain is halved recursively into nodes, until a 'leaf' node is obtained that contains a single particle, and is shown in Fig. 3.1a. Sub-nodes that do not contain any particles can be removed, improving computational efficiency. Each node has a mass equal to the collective mass of the constituent particles, and is located at the centre of mass of the particle group.

In Fig. 3.1b, it is visible that the potential $\Phi(\boldsymbol{r})$ may be written as:

$$\begin{aligned}\Phi(\boldsymbol{r}) &= -G\sum_i \frac{m_i}{|\boldsymbol{r}-\boldsymbol{x}_i|} \\ &= -G\sum_i \frac{m_i}{|\boldsymbol{r}-\boldsymbol{s}+\boldsymbol{s}-\boldsymbol{x}_i|}\end{aligned} \tag{3.4}$$

from which, assuming:

$$|\boldsymbol{x}_i - \boldsymbol{s}| \ll |\boldsymbol{r} - \boldsymbol{s}|, \tag{3.5}$$

and defining $\boldsymbol{y} \equiv \boldsymbol{r} - \boldsymbol{s}$, a Taylor expansion of the denominator in Eq. (3.4) yields

(e.g. Binney & Tremaine, 2008):

$$\frac{1}{|\boldsymbol{y}+\boldsymbol{s}-\boldsymbol{x}_i|} \simeq \frac{1}{|\boldsymbol{y}|} - \frac{\boldsymbol{y}\cdot(\boldsymbol{s}-\boldsymbol{x}_i)}{|\boldsymbol{y}|^3} + \frac{1}{2}\frac{\boldsymbol{y}^T\left[3(\boldsymbol{s}-\boldsymbol{x}_i)(\boldsymbol{s}-\boldsymbol{x}_i)^T - (\boldsymbol{s}-\boldsymbol{x}_i)^2\right]\boldsymbol{y}}{|\boldsymbol{y}|^5}, \quad (3.6)$$

where the first term gives rise to the monopole moment, the second term to the dipole moment, and the third term to the quadrupole moment. The dipole term vanishes in the centre of mass frame. The monopole can be calculated by:

$$M = \sum_i m_i, \quad (3.7)$$

and the quadrupole is given by:

$$Q_{ij} = \sum_k m_k \left[3(\boldsymbol{s}-\boldsymbol{x}_k)_i(\boldsymbol{s}-\boldsymbol{x}_k)_j - \delta_{ij}(\boldsymbol{s}-\boldsymbol{x}_k)^2\right]. \quad (3.8)$$

Thus, the potential is computed as:

$$\Phi(\boldsymbol{r}) = -G\left(\frac{M}{|\boldsymbol{y}|} + \frac{1}{2}\frac{\boldsymbol{y}^T\boldsymbol{Q}\boldsymbol{y}}{|\boldsymbol{y}|^5}\right). \quad (3.9)$$

For computational efficiency, GADGET-3 uses only the monopole moment. The approximation is only valid if the particle group is sufficiently far from the subject particle, satisfying the criterion imposed by Eq. (3.5):

$$\theta \simeq \frac{\langle|\boldsymbol{x}_i-\boldsymbol{s}|\rangle}{|\boldsymbol{y}|} \simeq \frac{l}{y} \ll 1, \quad (3.10)$$

where l is the particle group radius. If Eq. (3.10) is not satisfied, the node is opened, and Eq. (3.10) calculated for each sub-node, and is termed the 'tree-walk'. The procedure is repeated until Eq. (3.10) is satisfied, and any remaining sub-nodes are ignored. Alternative opening criteria exist, such as the opening criteria employed by GADGET-3:

$$\frac{GM}{r^2}\left(\frac{l}{r}\right)^2 \leq \alpha|\boldsymbol{a}|, \quad (3.11)$$

where M is the node mass, $|\boldsymbol{a}|$ is the magnitude of the total acceleration of the previous timestep, and α is a user-defined tolerance parameter (Springel, 2005). The criterion of Eq. (3.11) aims to reduce the absolute force error introduced in interactions between a particle and a node. Note that at the first timestep, when particle accelerations are not known, GADGET-3 uses the distance-based criterion of Eq. (3.10).

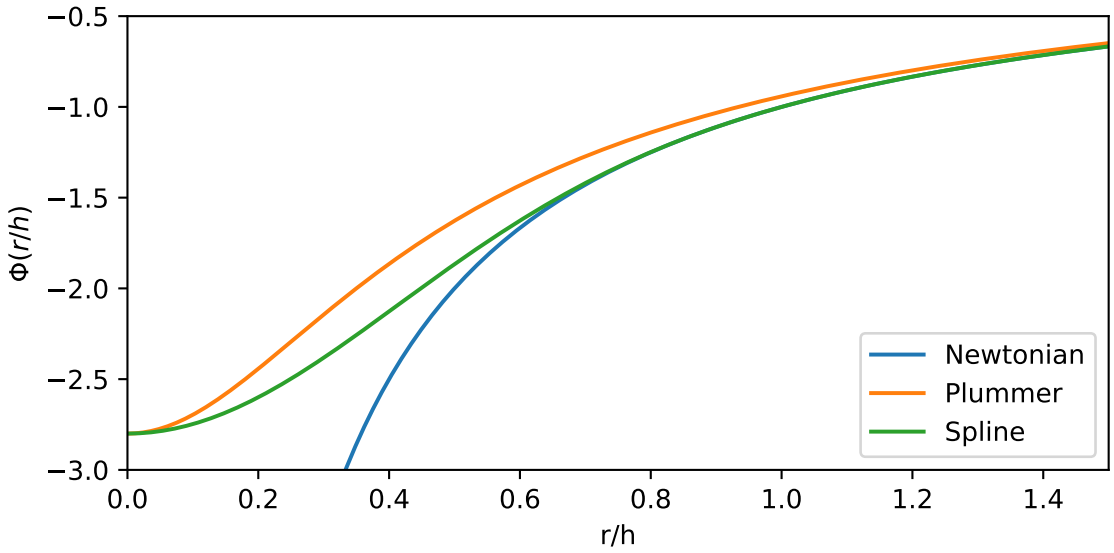

Figure 3.2: Comparison of the Plummer potential and the Monaghan & Lattanzio (1985) spline potential to the Newtonian potential. Both softened potentials converge as $r \to 0$, unlike the Newtonian potential. The spline kernel is exactly Newtonian for $r/h \geq 1$, unlike the Plummer potential which is never quite Newtonian. Here h is taken to be 1.0, from which $\epsilon = h/2.8$.

3.3 Dynamics: Softened and Unsoftened

As the real number of physical bodies within a galactic merger simulation far exceeds the computational limits of a direct N-body solution, the mass density of the system is instead represented as a distribution of a continuous variable. Monte Carlo methods are used to sample the phase space distribution (see §2.1.3), with the sample consisting of macro simulation particles that trace the six-dimensional phase space distribution, analogous to Lagrangian particles in fluid dynamics. The evolution of the macro particles thus describes the evolution of the phase space distribution function. To compensate for the discretisation of the phase space distribution, the divergence in the gravitational potential of Eq. (3.2) must be softened. A simple softening scheme is the Plummer softening, which introduces a small constant ϵ to the potential equation:

$$\Phi(r) = -\frac{Gm}{\sqrt{r^2 + \epsilon^2}}, \tag{3.12}$$

where r is the radial distance between the two simulation masses. A comparison of the Plummer potential to the Newtonian potential is shown in Fig. 3.2. Critically, the error in the Plummer potential relative to the Newtonian potential at small particle separations is significant, which throughout the simulation may accumulate to result in large-scale dynamical errors.

An improvement to the Plummer softening is introduced by the Monaghan & Lattanzio (1985) softening, which employs the use of basis-splines (B-splines) that interpolate with errors less than $\mathcal{O}(h^2)$, where h is a resolution measure. B-splines are non-zero within a finite domain, have continuous first or second derivatives, and are spherically symmetric. In GADGET-3 the spline-potential is used (Springel et al., 2001):

$$\Phi(r) = G\frac{m}{h}W_2\left(\frac{r}{h}\right) \tag{3.13}$$

from which the spline-kernel W_2 is (taking $u \equiv r/h$):

$$W_2(u) = \begin{cases} \frac{16}{3}u^2 - \frac{48}{5}u^4 + \frac{32}{5}u^5 - \frac{14}{5}, & 0 \leq u < \frac{1}{2}, \\ \frac{1}{15u} + \frac{32}{3}u^2 - 16u^3 + \frac{48}{5}u^4 - \frac{32}{15}u^5 - \frac{16}{5}, & \frac{1}{2} \leq u < 1, \\ -\frac{1}{u}, & u \geq 1. \end{cases} \tag{3.14}$$

Choosing $h = 2.8\epsilon$, where ϵ is again the Plummer softening length, the B-spline converges to the Plummer model as $r \to 0$. The B-spline converges to the Newtonian potential more rapidly with increasing r than the Plummer potential for $r < h$, and is exactly Newtonian beyond $r = h$ as seen in the third case of Eq. (3.14). Conversely, the Plummer potential is never exactly Newtonian. Using the spline kernel thus significantly reduces the accumulated error in the force calculation compared to the Plummer model (see Fig. 3.2).

Simulation particles which are used to represent the density distribution of a particular particle species must be softened. Typically, these particle species are stars and dark matter. The softening lengths used for simulation particles must be large enough that the density distribution is adequately described. A comparison of DM modelled with two differing softening lengths for a given system configuration is shown in Fig. 3.3. DM simulation particles in particular must model a smooth density distribution, as the simulation particle masses are often large, and comparable to the mass of a supermassive black hole around which lies the region of interest for this study. Critically, the Ketju region is not embedded within a constant gravitational potential perturbed by the potential of the DM distribution in the left panel (ϵ_{DM} =10 pc) of Fig. 3.3, but rather experiences the effect of the DM potential from individual particles. The short softening length can result in unphysical dynamics if the separation r between a SMBH and a DM particle becomes sufficiently reduced. An extreme example of such an unphysical event is DM-driven SMBH coalescence. DM particles with a short softening length interact with the SMBHs akin to individual massive particles, exerting a force great enough to significantly disrupt the

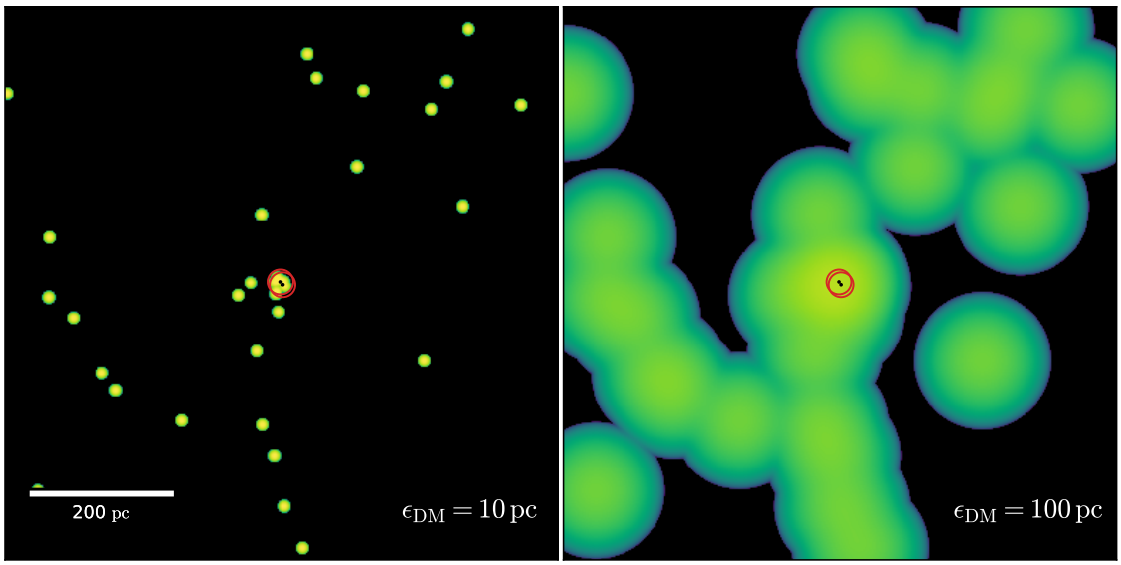

Figure 3.3: Dark matter particle softening in the inner 200 pc region around both SMBHs. The vicinity about the SMBHs (the Ketju region, see §3.4) is indicated by the red circles. The DM particles are shown with colouring proportional to the magnitude of the potential. Choosing too small a softening (left, ϵ =10 pc) can lead to unphysical dynamics, such as DM-driven SMBH merging. Choosing an appropriately large softening length (right, ϵ =100 pc) is required to reproduce accurate dynamics in the collisionless regime.

SMBH orbit. The disruption can lead to the SMBH merger timescale being of the order of a few hundred years.

The right panel of Fig. 3.3 represents a better choice of DM softening length, with $\epsilon_{\rm DM}$ =100 pc. Importantly, the Ketju region is well embedded within the DM potential, and thus interacts with the DM simulation particles as a smooth perturbation to the gravitational potential. Consequently, physical dynamics are better represented compared to the case of $\epsilon_{\rm DM}$ =10 pc, i.e. SMBH coalescence proceeds via physically meaningful stellar interactions.

In practice, the softening lengths of different particle species is chosen such that the softening is proportional to the mean interparticle separation of that species. The constant of proportionality typically ranges between 0.1 and 0.02 (e.g. Theis, 1998; Springel, 2005). Further discussion on motivating a choice of softening length is presented in §4.4.

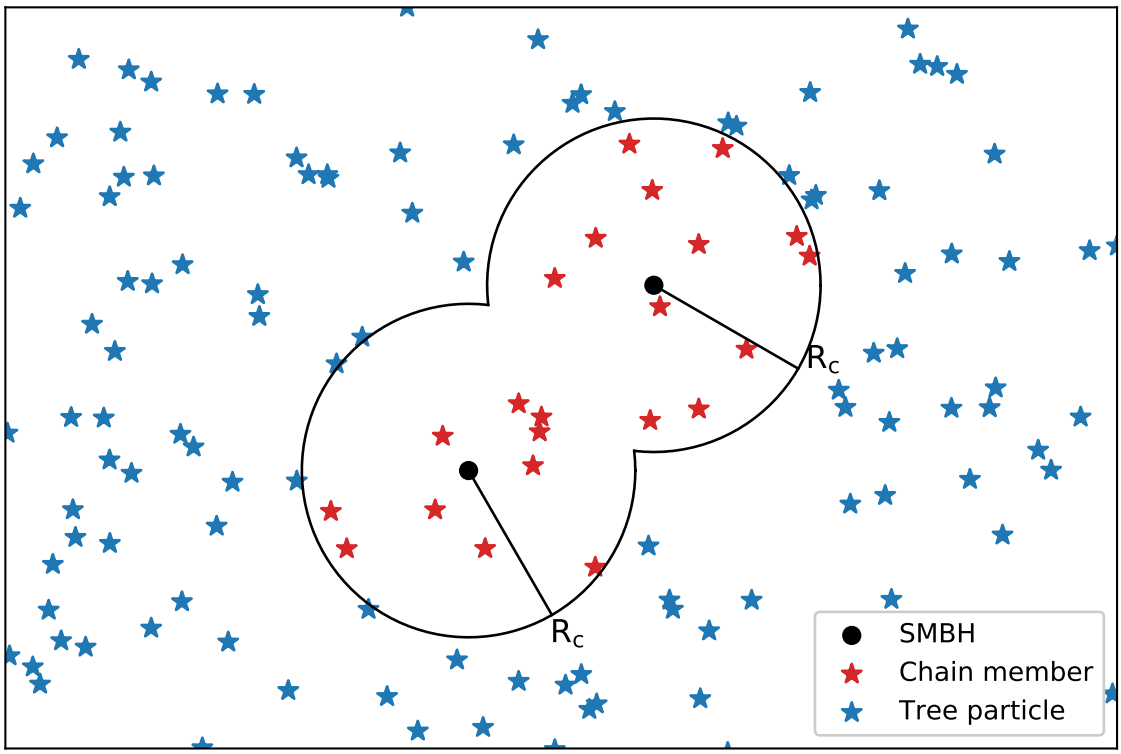

Figure 3.4: Two-dimensional region division in the KETJU code. The region immediately surrounding the SMBHs (black points) is the Ketju region, which may contain multiple SMBHs. The chain radius R_c is indicated by the black line. Stellar particles within the Ketju region are shown in red. Particles beyond the chain radius are integrated using the TreePM method of GADGET-3, and are indicated by blue stars.

3.4 Ketju

The hybrid regularised tree code KETJU[1] (Rantala et al., 2017) extends upon the capabilities of the GADGET-3 code by introducing a small region of user-defined radius about all SMBHs that allows for extremely high accuracy in dynamical calculations. The inner (Ketju) region is integrated using minimum spanning tree algorithmic regularisation (MSTAR, see §3.4.2), within which the force calculation between stellar particles and the SMBH is not softened. Particles which are not a member of the Ketju region are evolved using the TreePM scheme of GADGET-3, and are termed tree particles. Tree particles interact with the Ketju particles via the standard Tree-PM scheme. A schematic diagram of the region division is shown in Fig. 3.4.

As shown in Fig. 3.5, KETJU allows for the evolution of a SMBH merger to proceed to a much smaller orbital separation than in standard GADGET-3. Addition-

[1]Ketju is Finnish for 'chain'.

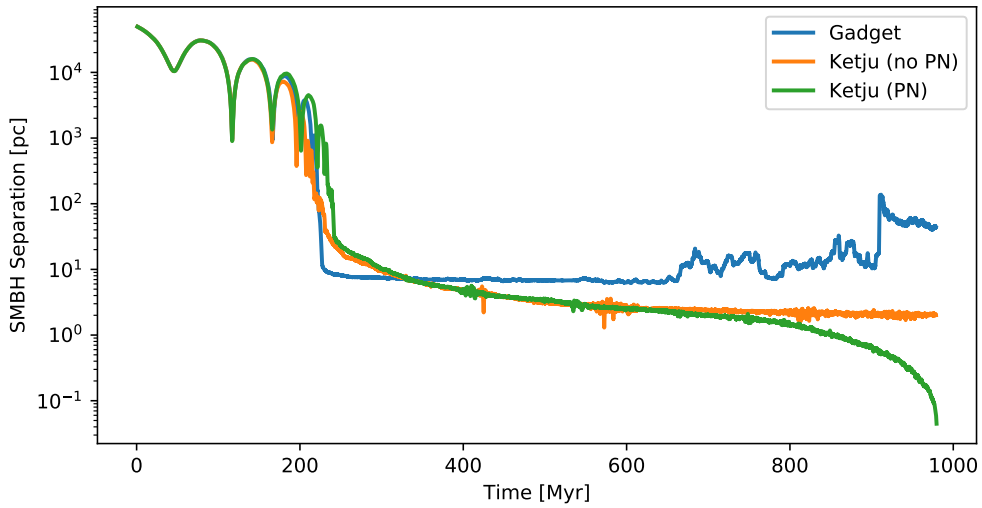

Figure 3.5: Comparison of the SMBH radial separation as a function of time for three runs starting from identical initial conditions. The separation has been smoothed with a moving average scheme to remove periodic oscillations arising from the orbital eccentricity. The GADGET-3 run (blue) does not allow for the SMBH binary to achieve close separation, whereby the separation stalls at the softening length ($\sim$10 pc). Two KETJU runs, one with and one without PN terms enabled, are shown in orange and green respectively. The use of PN corrections is essential for the SMBH binary separation to sufficiently reduce to allow for the final orbital decay by GW emission through the dissipative PN2.5 and PN3.5 terms. Without PN corrections, the KETJU simulation stalls at $\sim$1 pc.

ally, with Post-Newtonian corrections, the SMBH binary is able to be evolved until the SMBH merger criteria is satisfied (see §3.4.6), allowing one to study the merger system until the SMBH binary has a separation of the order 10^{-2} pc, corresponding to a few tens of the Schwarzschild radii of the binary. The superiority of KETJU over GADGET-3 in the study of SMBH orbital dynamics is thus clearly demonstrated.

3.4.1 Regularised Region Overview

Particles within the regularised region of KETJU satisfy a distance criterion, whereby the radial distance of the particle from a SMBH $||\boldsymbol{r}_i - \boldsymbol{r}_\bullet||$ must be less than the chain radius r_{chain}, defined as:

$$r_{\text{chain}} \geq 2.8\epsilon_\star \tag{3.15}$$

where $\epsilon_\star$ is the softening length of stellar particles used in the definition of the spline kernel Eq. (3.14). Only stellar particles and SMBHs may belong to a chain system, i.e. gas (if used) and DM particles are unable to enter the chain system by defini-

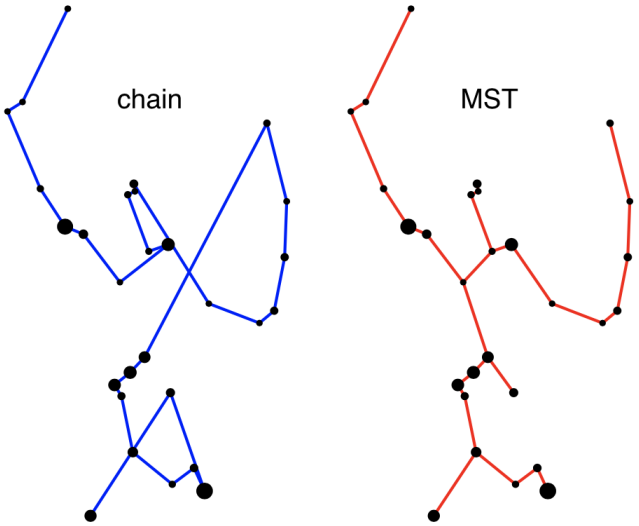

Figure 3.6: Different coordinate systems used for a collection of particles. *Left:* Original chain system, whereby each node is connected to at most two chain segments, a 'head', and a 'tail'. *Right:* Minimum spanning tree coordinate system. An arbitrary number of segments may branch from any node. Figure reproduced from Rantala et al. (2020) (their Fig. 1).

tion. The softening length criterion ensures that the potential calculated between all stellar particles and the SMBH(s) is unsoftened. A previous code version defined the chain radius with respect to the SMBH mass $M_\bullet$, resulting in an ambiguity when the SMBHs were of unequal mass. Defining the chain radius with respect to the stellar softening length safeguards the Ketju region against softened potential calculations in unequal mass merger events.

As shown in Fig. 3.4, multiple (i.e. two in the case of an isolated merger) SMBHs may belong to a single Ketju region. As a result, each member of a Ketju region can only belong to a single Ketju region. In the event:

$$||\boldsymbol{r}_{\bullet,i} - \boldsymbol{r}_{\bullet,j}|| < r_{\mathrm{chain},i} + r_{\mathrm{chain},j}, \tag{3.16}$$

the two Ketju regions are joined.

3.4.2 MSTAR

The original KETJU code (Rantala et al., 2017) achieved accurate small-scale dynamics about each SMBH by using the algorithmic regularisation technique, discussed in §2.4, coupled with a chained coordinate system. In the chained coordinate system, a set of position vectors $\boldsymbol{X}_k$ are chosen dependent on the relative distance between particles following Mikkola & Merritt (2008) and Rantala et al. (2017). The current version of the KETJU code introduces instead a minimum spanning tree coordinate

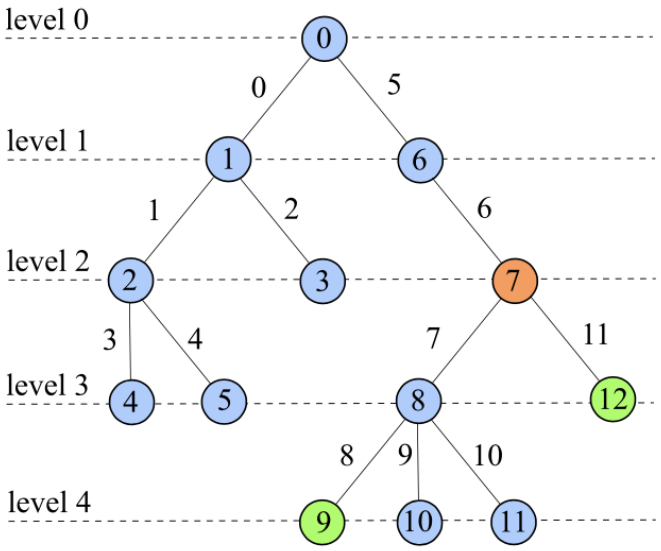

Figure 3.7: Tree structure with labelled vertices (0-12) and edge weights. The tree structure contains five levels. The lowest common ancestor of vertices V_9 and V_{12} (shaded green) is vertex V_7 (shaded orange). Figure reproduced from Rantala et al. (2020) (their Fig. 2).

system algorithmic regularisation (MSTAR) scheme. Qualitatively, the difference between the two schemes is visualised in Fig. 3.6. The minimum spanning tree (MST) coordinate system, coupled with an improved parallelisation scheme and cache efficiency, allows the MSTAR integrator to integrate systems with a particle count in the Ketju region in excess of 10^4, two orders of magnitude more than the AR-CHAIN technique. The MST coordinates are explained in the terminology of graph theory (e.g Harary, 1969) following Rantala et al. (2020).

The particles within the Ketju region are used as vertices V connected by edges E weighted by the relative distance between vertices to define a graph $G = (V, E)$. The sequence of edges with each vertex included exactly once (a Hamiltonian path), and that has the minimum edge weight, is found using the Prim algorithm (Prim, 1957). The Prim algorithm (see Fig. 3.7) in the context of MSTAR is presented.

1. The particle spatially closest to the centre of mass is chosen to be the starting vertex V_0.

2. The edge E connected to V_0 with the minimum weight is added to the MST and labelled V_1.

3. The minimum edge weight between vertices in the MST and vertices yet to be added are found, and the corresponding vertex added to the MST until all vertices belong to the MST.

In the instance of MSTAR, only an approximate MST is required to accurately resolve the system dynamics. The MST approach has the distinct advantage over the chained coordinate system in that spatially close particles are necessarily close in the MST data structure (Rantala et al., 2020), as shown in Fig. 3.6.

3.4.3 Timesteps

The GADGET-3 timestep $\Delta t_{\rm G}$ is determined as:

$$\Delta t_{\rm G} = \min \left[\Delta t_{\rm max}, \left(\frac{2\eta\epsilon}{|\boldsymbol{a}|} \right)^{1/2} \right], \tag{3.17}$$

where $\Delta t_{\rm max}$ is a user-defined maximum timestep, ϵ is the gravitational softening length, η a user-defined error tolerance parameter (typically set to 2×10^{-3}), and $\boldsymbol{a}$ the particle acceleration vector (Springel, 2005). At each GADGET-3 timestep $\Delta t_{\rm G}$, many timestep updates $\Delta t_{\rm K}$ are made for particles within the Ketju region. Regardless of the coordinate system (chained or MST) used, the coordinate structure is rebuilt at each $\Delta t_{\rm G}$, and assumed to be sufficiently accurate for the sub-timesteps $\Delta t_{\rm K}$. The primary advantage of using a chained/MST coordinate system lies in the reduction of numerical round-off error associated with the subtraction of two large floating point numbers (e.g. Rantala et al., 2017). The equations of motion may be recast to be used in the new coordinate system, such that the subtraction of large numbers occurs only once every $\Delta t_{\rm G}$, thus reducing the accumulated floating point error arising from integrations during the small sub-timesteps $\Delta t_{\rm K}$.

3.4.4 Regularised Equations of Motion

The equations of motion for the chained coordinate system may be naturally extended to the MST coordinate system. The physical quantities become, in chained coordinates:

$$\boldsymbol{X}_k = \boldsymbol{r}_{k+1} - \boldsymbol{r}_k \tag{3.18}$$

$$\boldsymbol{V}_k = \boldsymbol{v}_{k+1} - \boldsymbol{v}_k \tag{3.19}$$

$$\boldsymbol{A}_k = \boldsymbol{a}_{k+1} - \boldsymbol{a}_k \tag{3.20}$$

$$\boldsymbol{F}_k = \boldsymbol{f}_{k+1} - \boldsymbol{f}_k \tag{3.21}$$

$$\boldsymbol{G}_k = \boldsymbol{g}_{k+1} - \boldsymbol{g}_k. \tag{3.22}$$

Here $\boldsymbol{X}$ is the chained position vector, $\boldsymbol{V}$ the chained velocity vector, $\boldsymbol{A}$ the chained acceleration vector, $\boldsymbol{F}$ the chained additional acceleration due to external perturbations (see §3.4.7), and $\boldsymbol{G}$ the chained additional velocity-dependent accelerations

arising from e.g. PN corrections (refer to §2.5). The equations of motion, taking the fictitious time s, the kinetic energy T, potential energy U, and binding energy B as in §2.4, become:

$$\frac{\mathrm{d}t}{\mathrm{d}s} = \frac{1}{T+B} \tag{3.23}$$

$$\frac{\mathrm{d}\boldsymbol{X}_i}{\mathrm{d}s} = \frac{1}{T+B}\boldsymbol{V}_i, \tag{3.24}$$

and the velocity equations become:

$$\frac{\mathrm{d}\boldsymbol{V}_i}{\mathrm{d}s} = \frac{1}{U}(\boldsymbol{A}_i + \boldsymbol{F}_i + \boldsymbol{G}_i) \tag{3.25}$$

$$\frac{\mathrm{d}B}{\mathrm{d}s} = -\frac{1}{U}\sum_i m_i \boldsymbol{v}_i \cdot (\boldsymbol{f}_i + \boldsymbol{g}_i), \tag{3.26}$$

where the binding energy is evaluated in the original coordinate system for computational efficiency (Rantala et al., 2020). Finally, when it is appropriate to use chained coordinates must be determined, and is set by the condition:

$$\boldsymbol{r}_j - \boldsymbol{r}_i = \begin{cases} \boldsymbol{r}_j - \boldsymbol{r}_i & \text{if } |i-j| > N_\mathrm{d} \\ \displaystyle\sum_{k=\min\{i,j\}}^{\max\{i,j\}-1} \mathrm{sign}(i-j)\boldsymbol{X}_k & \text{if } |i-j| \leq N_\mathrm{d}, \end{cases} \tag{3.27}$$

where N_d is the index difference between two particles in the chain. Extensive testing by Mikkola & Merritt (2008) have found the optimum value of N_d to be $N_\mathrm{d} = 2$, as using chained coordinates for particles further than this in the chain reintroduces an increase in the floating point error in the calculation.

In MST coordinates, the notion of the location of a particle in the tree is less straightforward than in the chained coordinate system. However, N_d may be expressed in terms of the lowest common ancestor (LCA) vertex of the vertices V_i and V_j (Rantala et al., 2020). An example of the LCA is given in Fig. 3.7. If the level of a vertex V_i is represented by $L(V_i)$, the criterion for two vertices being within N_d of each other in the tree structure is:

$$|L(V_i) - L(V_\mathrm{LCA})| + |L(V_j) - L(V_\mathrm{LCA})| \leq N_\mathrm{d}, \tag{3.28}$$

as in Rantala et al. (2020). If Eq. (3.28) is not satisfied, the force calculation between the vertices V_i and V_j is computed in the original coordinate system, analogous to Eq. (3.27).

3.4.5 Gragg-Bulirsch-Stoer Extrapolation

To achieve very high-accuracy in the integration, the MSTAR scheme is coupled with an extrapolation method. One popular method is the serial Gragg-Bulirsch-Stoer (GBS) algorithm (Gragg, 1965; Bulirsch & Stoer, 1966). The GBS algorithm may be coupled to the leapfrog integration scheme (see §3.4.8). The scheme exploits that integration with a step size h will converge as $h \to 0$. In the GBS algorithm, a total step size H is divided into n segments of length h, which are integrated. The procedure is repeated $k_{\max}$ times with increasing n, which are used to extrapolate to the division of H as $n \to \infty$ with a polynomial function. In MSTAR the division sequence is given by:

$$n_k = \{2k \mid k \in \mathbb{N}, k > 0\}. \tag{3.29}$$

The integral is considered converged if the criterion:

$$\frac{||\Delta S_k||}{||S(s)||} \leq \eta_{\mathrm{GBS}}, \tag{3.30}$$

holds. In Eq. (3.30), S is any dynamical system variable, ΔS_k is the extrapolation error estimate after the k-th substep, and $S(s)$ is the value of the dynamical variable obtained after the last complete timestep. The parameter η_{GBS} acts as a tolerance, below which the integration is considered converged. Typically, a value of $\eta_{\mathrm{GBS}} \simeq 10^{-8}$ is used (Rantala et al., 2020). The parallelisation scheme of MSTAR computes all $k_{\max}$ subdivisions (typically 8 (e.g. Press et al., 2007)) of the region in parallel before extrapolating the result from each k subdivision and checking for convergence. If Eq. (3.30) is not satisfied, the step size is decreased such that for the interval H_{i+1}:

$$H_{i+1} = a_{\mathrm{GBS}} \left(\frac{\eta_{\mathrm{GBS}}}{\epsilon_k} \right)^{\frac{1}{2k-1}} H_i, \tag{3.31}$$

where ϵ_k is the maximum error in the dependent variables from the previous step, $a_{\mathrm{GBS}} \in (0, 1]$ is a safety parameter, and k is the substep sequence at which convergence was achieved for the region H_i (Press et al., 2007; Rantala et al., 2020). Additionally, it is ensured that the step size is decreased sufficiently to improve the likelihood of convergence by imposing:

$$H_{i+1} < 0.7 H_i. \tag{3.32}$$

3.4.6 SMBH Merger Criteria

In the KETJU simulations, particle mergers are implemented for SMBH-SMBH mergers and SMBH-stellar particle mergers, though the latter is not used in this work.

A SMBH binary will merge if the orbital separation of the binary becomes less than two times the radius of the innermost stable circular orbit r_{ISCO}, defined for Schwarzschild black holes as:

$$r_{\mathrm{ISCO}} = 3R_{\mathrm{S}}. \tag{3.33}$$

By using that the Schwarzschild radius R_{S} is the sum of the individual Schwarzschild radii of the binary constituents, the distance separation criterion for a SMBH merger is:

$$r_{\mathrm{min}} = 6\left(R_{\mathrm{S},1} + R_{\mathrm{S},2}\right), \tag{3.34}$$

as in Rantala et al. (2017). The conservation equations arising from the merging of the SMBH binary, taking $\boldsymbol{r}_{12} = \boldsymbol{r}_2 - \boldsymbol{r}_1$, are:

$$M = M_1 + M_2 \tag{3.35}$$

$$\boldsymbol{r} = \frac{M_1\boldsymbol{r}_1 + M_2\boldsymbol{r}_2}{M} \tag{3.36}$$

$$\boldsymbol{v} = \frac{M_1\boldsymbol{v}_1 + M_2\boldsymbol{v}_2}{M} \tag{3.37}$$

$$\boldsymbol{L} = \frac{M_1 M_2}{M}\boldsymbol{r}_{12} \times \boldsymbol{v}_{12} \tag{3.38}$$

$$\boldsymbol{S} = \boldsymbol{L} + \boldsymbol{S_1} + \boldsymbol{S_2}. \tag{3.39}$$

Here $\boldsymbol{L}$ is the angular momentum and $\boldsymbol{S}$ the spin. In the case the SMBHs are Schwarzschild black holes, the spin $\boldsymbol{S}$ is necessarily zero. The implementation of a merger event in KETJU follows that of GADGET-3, whereby one of the merging particles inherits the dynamical properties of the progenitor particles from the conservation laws, with the other particle being 'transformed' into a zero-mass particle that does not interact further with the simulation. The zero-mass particle may be removed from the simulation, though this is not implemented in the current version of KETJU. Consequently, whether or not a merger event has occurred can be ascertained from a zero-mass SMBH particle.

3.4.7 Perturbers

Tree particles, i.e. those particles that are not part of the Ketju region, may provide a force perturbation to the Ketju particles if the GADGET-3 opening criterion (Eq.(3.11)) is satisfied. Previous code versions (Rantala et al., 2017) incorporated a separate 'perturber' class of particles that provided individual force perturbations to Ketju particles, and were selected by a radial distance criterion. Due to computational inefficiency, particles either belong to the Ketju region or not. A prime source

of the computational inefficiency stemmed from analytically evolving the perturbing particle positions with a Taylor series:

$$\boldsymbol{r}_i(t_{\rm K}) = \boldsymbol{r}_i(t_{\rm G}) + \dot{\boldsymbol{r}}_i(t_{\rm G})\Delta t_{\rm K} + \frac{1}{2}\ddot{\boldsymbol{r}}_i(t_{\rm G})(\Delta t_{\rm K})^2. \tag{3.40}$$

In the current implementation (Rantala et al., 2020), all tree particles that provide a perturbing force to the Ketju particles are held in a fixed dynamical state for the duration of the GADGET-3 timestep $\Delta t_{\rm G}$, and consequent higher temporal resolution steps of the KETJU integration, $\Delta t_{\rm K}$. A single kick (see §3.4.8) from the perturbing particle is applied at the beginning and end of the MSTAR integration. In essence, the Ketju region is evolved independent of the background environment dynamics, with the exception of a perturbative force that is held constant throughout the GADGET-3 timestep $\Delta t_{\rm G}$. The difference in the experienced perturbing force is expected to be small between the two schemes. Thus, the computational speed up offered by the current implementation (Rantala et al., 2020) is favoured over earlier implementations (Rantala et al., 2017).

3.4.8 Leapfrog Integration

The second step in evolving the dynamic system after determining the interparticle forces is to update the positions and velocities of the particles (§3.1). In updating particle positions and velocities, a symplectic integration method is desirable. Symplectic integrators have conserved first integrals (i.e. energy), and demonstrate phase-space conservation (e.g. Springel, 2016). A widely used symplectic integrator is the leapfrog method, which whilst second-order accurate, provides lower energy error than higher order schemes such as the fourth-order Runge-Kutta (RK-4) scheme, due to its symplectic nature. A well-known comparison of the energy-conserving properties of the leapfrog scheme compared to the RK-4 scheme is the Kepler problem, shown in Fig. 3.8. Over an integration period of 200 orbits, the orbital semimajor axis is seen to decrease dramatically for the RK-4 scheme in Fig. 3.8, corresponding to an energy error that accumulates over the integration period. Comparatively, the leapfrog scheme displays orbital precession, but minimal change in orbital semimajor axis, over the same 200 orbits.

The central idea of the leapfrog integration is to update the position ('drifting') and velocity ('kicking') of a particle by using a time evolution operator $\tilde{U}(\Delta t)$ as in Springel (2005). Eq. (3.41) is the drift-kick-drift (DKD) scheme, and Eq. (3.42) is

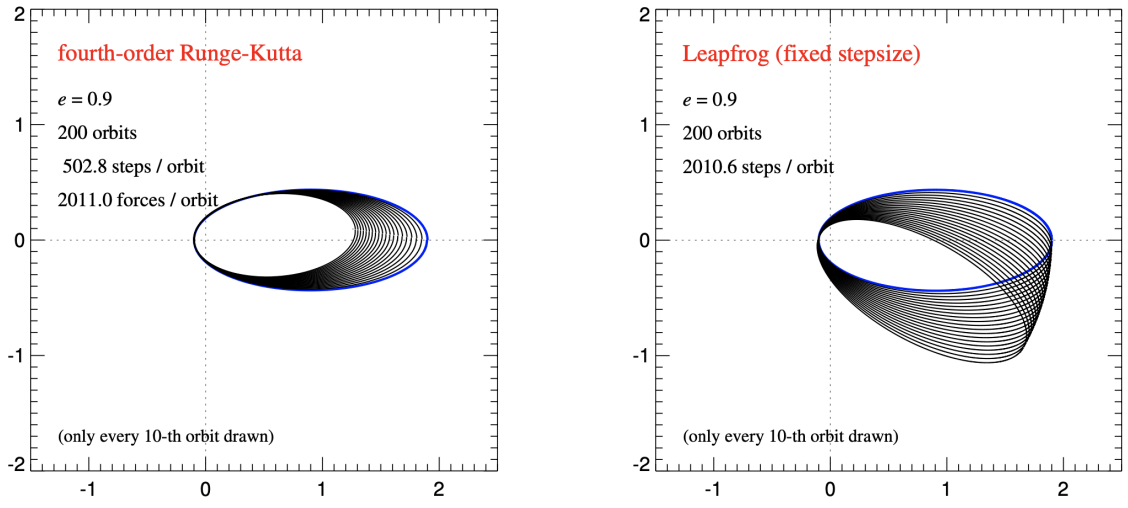

(a) **(b)**

Figure 3.8: Two integration schemes of the Kepler problem. *Left:* Fourth-order Runge-Kutta scheme. Note the decreasing semimajor axis corresponding to cumulative energy error. *Right:* Leapfrog integrator, which displays only minor energy error and small orbital precession. In both figures, the blue ellipse marks the initial orbit. Figures are reproduced from Springel (2005) (their Fig. 4).

the kick-drift-kick (KDK) scheme.

$$\tilde{U}(\Delta t) = D\left(\frac{\Delta t}{2}\right) K(\Delta t) D\left(\frac{\Delta t}{2}\right) \tag{3.41}$$

or

$$\tilde{U}(\Delta t) = K\left(\frac{\Delta t}{2}\right) D(\Delta t) K\left(\frac{\Delta t}{2}\right), \tag{3.42}$$

where the operator D is the drift operator and the operator K is the kick operator. The operator definitions are given in Quinn et al. (1997) as:

$$D_t(\Delta t) : \begin{cases} \boldsymbol{p}_i \mapsto \boldsymbol{p}_i \\ \boldsymbol{r}_i \mapsto \boldsymbol{r}_i + \dfrac{\boldsymbol{p}_i}{m_i} \displaystyle\int_t^{t+\Delta t} \mathrm{d}t \end{cases} \tag{3.43}$$

$$K_t(\Delta t) : \begin{cases} \boldsymbol{r}_i \mapsto \boldsymbol{r}_i \\ \boldsymbol{p}_i \mapsto \boldsymbol{p}_i + \boldsymbol{f}_i \displaystyle\int_t^{t+\Delta t} \mathrm{d}t, \end{cases} \tag{3.44}$$

where $\boldsymbol{p}_i$ is the momentum, a is the cosmic scale factor, and $\boldsymbol{f}_i$ the force on particle i and is given by:

$$\boldsymbol{f}_i = -\sum_j m_i m_j \frac{\partial \Phi(\boldsymbol{x}_{ij})}{\partial \boldsymbol{x}_i}. \tag{3.45}$$

In GADGET-3 the integration scheme used is a variation of the KDK scheme (Springel, 2005).

In MSTAR the leapfrog scheme is updated to be usable in MST (or chained) coordinates. Recalling that h is defined as the total integration step H divided into n substeps (see §3.4.5), the MST leapfrog is given as:

$$\tilde{U}(h,n) = D\left(\frac{h}{2}\right)\left[K\left(h\right)D\left(h\right)\right]^{n-1}K\left(h\right)D\left(\frac{h}{2}\right) \tag{3.46}$$

as in Rantala et al. (2020).

3.4.9 Loosening of Stellar Binaries

In the collisional Ketju region, uncharacteristically tight binaries between two-stellar particles or a stellar particle and a SMBH may form, particularly if the stellar density is high (see §4.1.4). Owing to the adaptive timestep of GADGET-3, as seen in Eq. (3.17), the simulation may be brought to a standstill if a disproportionate amount of wall-clock time is spent integrating a single, tightly bound binary system. A numerical work around is described.

At each timestep, all bound binary systems within a Ketju region are found through the energy criterion $E < 0$, where the energy E is the difference of kinetic and potential energies of the particles. In the event a star-star or star-SMBH binary has an orbital period:

1. Smaller than the GADGET-3 timestep Δt_{G}, and

2. Smaller than the SMBH-SMBH binary period,

then the binary system may need to be loosened. At most, only one tight binary system per Ketju region per timestep may be loosened if there are multiple tight binaries. The tight binary system to be loosened is the system with the shortest period, and must have a period that is statistically a clear outlier. The binary system with the shortest period is considered to have an outlying period if:

$$N_{\mathrm{B}<2P_\bullet} < \max\left\{\frac{N_{\mathrm{R}}}{100}, 5\right\}, \tag{3.47}$$

where $N_{\mathrm{B}<2P_\bullet}$ is the number of binaries with a period less than two times the SMBH-SMBH binary period, and N_{R} is the number of particles within the Ketju region. If Eq. (3.47) is satisfied, then the binary system with the shortest period is loosened by kicking the particles to twice the orbital period. The binary kick does not occur at

the apocentre or pericentre of the orbit, but simply at the time when the short period condition is met. Kicking the particles, whilst violating the energy conservation principle, is expected to have minimum impact on the overall dynamics due to the infrequency with which the process occurs, some 10^2–10^3 total instances depending on the mass resolution and the stellar density. Additionally, the doubling of a very short binary orbital period will result in an orbital period that is at most comparable to the orbital period of the SMBH binary. The loosening of tight stellar binaries is performed only if the overall simulation performance will be improved.

4. KETJU Simulations: Initial Conditions

In the following chapter, the method by which the initial conditions for the seventeen major-merger events simulated were determined is detailed. The simulations extend upon those performed by Rantala et al. (2017), with the physical properties of the individual galaxies being chosen through statistical motivation from observations. The physical properties of massive galaxies, for example the ratio of bulge mass to SMBH mass, are tightly correlated (e.g. Magorrian et al., 1998; Marconi & Hunt, 2003; Häring & Rix, 2004; Johansson et al., 2009b). To ascertain if the Final Parsec Problem is a physical phenomenon, or a manifestation of numerical representation, the simulated galaxies are required to be representative of those real observed galaxies. The aim is to reduce the number of free physical parameters to two: namely the bulge mass, and the steepness (γ-parameter) of the density distribution, where $\rho \propto r^{-\gamma}$. The effect of mass resolution is also to be investigated.

4.1 Component Masses and Density

4.1.1 Stellar Bulge Mass

The first free physical parameter to be investigated is the bulge mass of the elliptical galaxy, here taken to pertain solely to the stellar mass. Previous simulations (e.g. Khan et al., 2016; Rantala et al., 2017; Ryu et al., 2018; Lahén et al., 2018; Rantala et al., 2018; Mannerkoski et al., 2019) have used stellar masses of $10^{10}\,\mathrm{M}_\odot$–$10^{11}\,\mathrm{M}_\odot$. To motivate the choice of stellar mass for the model galaxies from a statistical standpoint, the masses of all elliptical galaxies with stellar mass greater than $10^9\,\mathrm{M}_\odot$ from the Sloan Digital Sky Survey[1] (SDSS) Data Release 7 (DR7) were taken and binned into twenty binnings. The SDSS DR7 contains 61543 galaxies with a visual mor-

[1] http://www.sdss.org

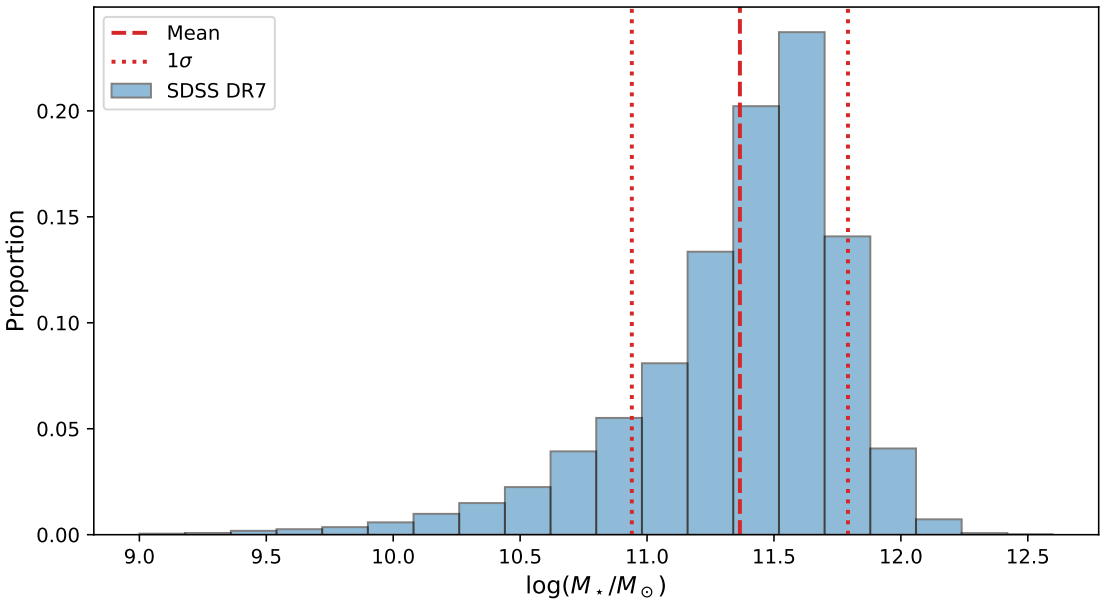

Figure 4.1: Stellar mass distribution of elliptical galaxies in SDSS DR7. The mean value, 11.365 $\log(M_\star/\mathrm{M}_\odot)$, is given by the dashed red line, with 1-σ bounds by the dotted red lines. The histogram is scaled to indicate the proportion of galaxies falling within a given mass bin.

phology classification of elliptical, defined by a lack of disc structure in a composite g-r-i survey image (Lintott et al., 2008). The redshift range of the dataset extends from $z \sim 0.010$ to $z \sim 0.497$. Critically, the SDSS survey contains a high number of high-mass elliptical galaxies compared to for example the Galaxy and Mass Assembly (GAMA) survey (Baldry et al., 2018). The high-mass SDSS galaxies are suitable for modelling as gas-free galaxies; the lack of cold gas and dust present in high-mass elliptical galaxies allows for gas to be neglected in the simulation (e.g. Mo et al., 2010). The distribution of elliptical galaxy stellar masses from SDSS DR7 is shown in Fig. 4.1. The mean stellar mass, found to be 11.365 $\log(M_\star/\mathrm{M}_\odot)$, is indicated by the dashed red line, with 1-σ bounds given by the dotted red lines. From the SDSS DR7, two galaxies of different masses were chosen to be investigated. The first has a stellar mass of 11.365 $\log(M_\star/\mathrm{M}_\odot)$, i.e. the mean value of the data sample. The second has a mass one standard deviation greater than the mean value; the mass of the second galaxy is taken to be 11.792 $\log(M_\star/\mathrm{M}_\odot)$. Consequently, the investigated mergers have mass ratios $q = 1$ in the equal mass merger case, and $q \simeq 2.67$ in the unequal mass merger case: both merger events are major (see §2.2.2).

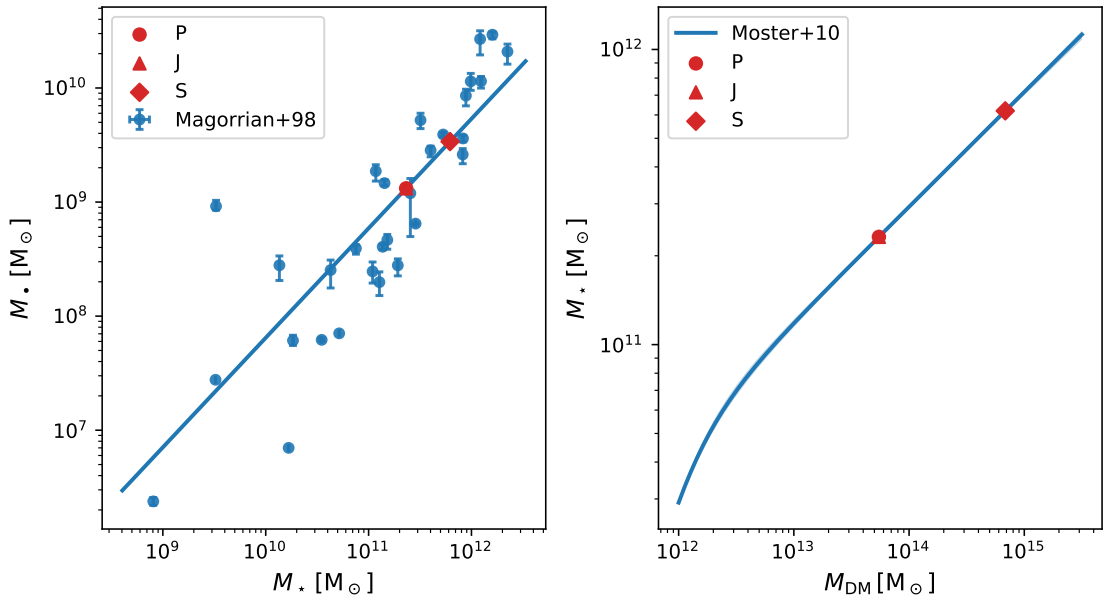

Figure 4.2: *Left:* Observational data and fit of SMBH mass to bulge mass (Magorrian et al., 1998). *Right:* Analytical function of bulge mass as a function of DM mass as described by Moster et al. (2010). The profile is parametrised in accordance with Yang et al. (2003). In both plots, class P, J, and S galaxies are shown by a circle, triangle, and diamond respectively. As the $M_\bullet$–$M_\star$ and $M_\star$–$M_{\rm DM}$ relations are the same for class P and J galaxies, the circle and the triangle coincide.

4.1.2 Ratio of Bulge Mass to SMBH Mass

The tight relation between the stellar mass and the mass of the SMBH of elliptical galaxies has been researched extensively since observational findings were first published by Magorrian et al. (1998) and further explored by Marconi & Hunt (2003) and Häring & Rix (2004). Magorrian et al. (1998) analysed a sample of 32 elliptical galaxies from HST data to determine that the logarithm of SMBH mass $M_\bullet$ was proportional to the logarithm of stellar mass, by Eq. (4.1). A plot of the data and fit from Magorrian et al. (1998) is shown in the left panel of Fig. 4.2:

$$\log(M_\bullet/\mathrm{M}_\odot) = (0.96 \pm 0.12)\log(M_\star/\mathrm{M}_\odot) - (1.79 \pm 1.35). \tag{4.1}$$

From Eq. (4.1), the SMBH mass of the model galaxies are determined, and presented in Table 4.1. An alternate derivation of SMBH mass may be derived from the $M_\bullet$–σ relation (presented in §4.3.4), however this would require initially generating the model galaxy without the SMBH to determine the central stellar velocity dispersion. The simpler approach, determining SMBH mass from stellar bulge mass, is thus employed for this study.

4.1.3 Dark Matter Halo Mass

The mass of the dark matter halo $M_{\rm DM}$, like the mass of the SMBH, is correlated with the stellar mass of the galaxy (e.g. Erickson et al., 1987; Springel & Hernquist, 2003; Yang et al., 2003). To determine the halo mass of the model galaxies, the halo mass is calculated from the stellar mass following the Halo Occupation Distribution formalism as in Moster et al. (2010). The relation follows the parametrisation of Yang et al. (2003) (Eq. (4.2)):

$$\frac{m(M_{\rm DM})}{M_{\rm DM}} = 2\left(\frac{m}{M_{\rm DM}}\right)_0 \left[\left(\frac{M_{\rm DM}}{M_1}\right)^{-\beta} + \left(\frac{M_{\rm DM}}{M_1}\right)^{\gamma}\right]^{-1}. \tag{4.2}$$

In Moster et al. (2010) the best fit parameters are determined to be $\log(M_1) = 11.899$, $(m/M_{\rm DM})_0 = 0.02817$, $\beta = 1.068$, and $\gamma = 0.611$. The relation Eq. (4.2), with these parameters, is shown in the right panel of Fig. 4.2. To invert the function to determine the halo mass for a given stellar mass, the function is evaluated at 10^4 points such that $10.5 \leq \log(M_{\rm DM}) < 15$, and the first value greater than the desired stellar mass taken to be the halo mass.

4.1.4 Density Profiles

The second free physical parameter to be investigated is the central stellar density profile. A number of density profiles have been proposed during the 20$^{\rm th}$ century, most notably the de Vaucouleurs $r^{1/4}$ profile (de Vaucouleurs, 1948). Other profiles, such as the Hernquist, Jaffe, and Dehnen models, also describe well the stellar density profile of elliptical galaxies, and reduce to the de Vaucouleurs profile when accounting for projection onto the sky (Dehnen, 1993). The Dehnen profile (Dehnen, 1993) is the most general of the three latter profiles, and is described by the double-power law of Eq. (4.3):

$$\rho(r) = \frac{(3-\gamma)M}{4\pi}\frac{a}{r^{\gamma}(r+a)^{4-\gamma}}, \tag{4.3}$$

where a is a scaling radius.

The Hernquist model corresponds to Eq. (4.3) with $\gamma = 1$, and the Jaffe model with $\gamma = 2$. In this study, γ is left as a free parameter. Modelling of elliptical galaxies in the Coma cluster by Thomas et al. (2007) and ten elliptical galaxies in different environments by Humphrey & Buote (2010) have indicated that the total density (stellar plus dark matter) profile follow a power law relation $\rho(r) \propto r^{-\gamma}$ for $\gamma \sim 2.1$. Similar results were obtained by Remus et al. (2017) in numerous

cosmological simulations. Three galaxies in the Humphrey & Buote (2010) sample with total masses (dell'Antonio et al., 1995; O'Sullivan et al., 2005) comparable to the chosen simulation masses of $\log(M_\star/\mathrm{M}_\odot) = 11.365$ and $\log(M_\star/\mathrm{M}_\odot = 11.792)$ have density profiles with $\gamma \simeq 1.6$. The most massive galaxy of the Humphrey & Buote (2010) sample has a density profile with $\gamma \sim 1.39$.

The two stellar density slopes corresponding to $\gamma = 1.8$ and $\gamma = 1.6$ are chosen to be modelled. Following the observations of Humphrey & Buote (2010) of more massive elliptical galaxies having a shallower total density profile, found also in observations from the SPIDER & ATLAS^{3D} surveys (Tortora et al., 2014), the steeper density profile of $\gamma = 1.8$ is chosen to be used only for the $\log(M_\star/\mathrm{M}_\odot) = 11.365$ galaxy.

Consequently, three classes of galaxies are to be investigated, and have mass and density profile parameters as presented in Table 4.1. The class names are derived from the Finnish language, with the first class termed *pieni* ('small'), the second *jyrkkä* ('steep'), and the final class *suuri* ('large').

Mass and Density Parameters				
Class	$\log(M_\star/\mathrm{M}_\odot)$	$\log(M_\bullet/\mathrm{M}_\odot)$	$\log(M_{\mathrm{DM}}/\mathrm{M}_\odot)$	γ
P	11.365	9.120	13.738	1.6
J	11.365	9.120	13.738	1.8
S	11.792	9.530	14.835	1.6

Table 4.1: Mass and density parameters of the model galaxies. Galaxies are divided into three classes: P (*pieni*), J (*jyrkkä*), and S (*suuri*).

4.2 Model Generation

The model galaxies are generated following the procedures of Rantala et al. (2017) and Rantala et al. (2018). In both works, the galaxy initial conditions are generated using the distribution function method of Merritt (1985) and Hilz et al. (2012) to create a multicomponent, isotropic system: a single stellar population, enclosed within a single dark matter halo population, are created separately. Finally, the SMBH is placed at the centre of the system. To obtain accurate galactic models, the generation scheme is an iterative approach, whereby a 'trial' galaxy with the desired mass and density properties is produced, and its kinematics analysed (§4.3.1-4.5) to

ascertain if the model is realistic. Generally, two iterations are required to produce realistic and stable initial conditions for the model galaxy.

Assuming a density profile described by Eq. (4.3), the potential may be calculated from Eq. (4.4) (Dehnen, 1993):

$$\Phi(r) = \frac{GM}{a} \times \begin{cases} -\frac{1}{2-\gamma}\left(1 - \left(\frac{r}{r+a}\right)^{2-\gamma}\right), & \gamma \neq 2 \\ \ln\left(\frac{r}{r+a}\right), & \gamma = 2. \end{cases} \tag{4.4}$$

The total gravitational potential of the system, $\Phi_{\rm T}$ is defined as the sum of each individual component potential, namely:

$$\Phi_{\rm T} = \Phi_\star + \Phi_{\rm DM} + \Phi_\bullet \tag{4.5}$$

$$= -\frac{GM_\star}{r + a_\star} - \frac{GM_{\rm DM}}{r + a_{\rm DM}} - \frac{GM_\bullet}{r + \xi_\bullet}, \tag{4.6}$$

where it is demanded that the potential remains finite at $r = 0$, and hence a small softening $\xi_\bullet$ is introduced, typically of order 10^{-5} kpc for the SMBH particle (e.g. Rantala et al., 2017).

The spatial distribution of each component of the multicomponent sphere is sampled with Monte Carlo methods using the inverse of the cumulative mass function (e.g. Rantala et al., 2018). The cumulative mass function is the integral of the density profile in Eq. (4.3):

$$M(r) = 4\pi \int_0^r \rho(r) r^2 dr \tag{4.7}$$

$$= M\left(\frac{r}{r+a}\right)^{3-\gamma}. \tag{4.8}$$

In principle, the mass function extends asymptotically to M as $r \to \infty$, resulting in a small number of Monte Carlo generated particles residing at an unphysically large radial distance from the galactic centre. To combat this sampling effect, a maximum radius cut is applied, initially set to an extreme value of 10^5 kpc. The maximum radius is then reduced to $r_{\rm max} \sim 2r_{200}$kpc in the second model iteration, with particles at radial distance $r_i > r_{\rm max}$ being resampled from the inverse cumulative mass distribution until $r_i \leq r_{\rm max}$. Additionally, a minimum radial distance from the SMBH is prescribed for stellar particles to ensure computational efficiency, i.e. to protect the system against particles that are very bound to the central SMBH. Particles on very bound orbits force the simulation timestep to be dramatically reduced (see §GADGET). In all simulations, the minimum orbital radius $r_{\rm min}$ is set to half the SMBH softening length, such that $r_{\rm min} = 1.5 \times 10^{-3}$ kpc.

The velocity profiles of each component i are obtained from the phase-space distribution function f_i following Rantala et al. (2018). The distribution functions f_i are related to the the density ρ_i and total gravitational potential Φ_T through the Eddington formula (e.g. Binney & Tremaine, 2008):

$$f_i(\mathcal{E}) = \frac{1}{\sqrt{8}\pi^2} \int_{\Phi_\mathrm{T}=0}^{\Phi_\mathrm{T}=\mathcal{E}} \frac{d^2\rho_i}{d\Phi_\mathrm{T}^2} \frac{d\Phi_\mathrm{T}}{\sqrt{\mathcal{E}-\Phi_\mathrm{T}}}. \tag{4.9}$$

By using a relative potential Ψ defined such that $\Psi = -\Phi_\mathrm{T} + \Phi_0$ for some zero point Φ_0, the relative energy $\mathcal{E}$ in Eq. (4.9) can be defined as $\mathcal{E} = \Psi - \frac{1}{2}v^2$ for a velocity v (Binney & Tremaine, 2008). Typically, the zero point potential Φ_0 is chosen such that $f_i > 0$ for $\mathcal{E} > 0$, and $f_i = 0$ for $\mathcal{E} \leq 0$. In the case of the simulated galaxies in this study, which are created in isolation and extend (ignoring sampling methods) to infinity, the zero potential is taken to be zero and the relative energy equal to the binding energy of the system (Binney & Tremaine, 2008).

The distribution functions f_i are computed into look-up tables, after which Monte Carlo methods are again employed to randomly sample the distributions.

4.3 Kinematic Relations and Properties

After generating the model galaxies from the mass and density profile parameters as in Table 4.1, a number of kinematic assessments are made to ensure the model galaxy accurately represents a physical elliptical galaxy. The kinematic assessments to be discussed are the value of the half-mass radius, the inner dark matter fraction, the value of the virial radius, and the SMBH mass – stellar velocity dispersion relation.

4.3.1 Mass Distribution and Half-Mass Radius

The first of kinematic assessments is the radial distribution of mass, and the consequent stellar half-mass radius $R_{1/2}$, defined as the radius within which half of the stellar (luminous) mass is contained (e.g. Remus et al., 2017). From Eq. (4.3), constraining the density profile steepness γ still allows for a choice of stellar scaling radius a.

Constraining the density profile shape is done following observations by Thomas et al. (2007) and simulations by Remus et al. (2017), such that the total density follows $\rho(r) \propto r^{-2.1}$ for $r \lesssim r_{200}$. The dark matter halo is modelled as a Hernquist sphere ($\gamma = 1$) as in Rantala et al. (2017), with choice of scale radius a_DM. A preliminary choice for a and a_DM is made, and the radial mass distribution examined.

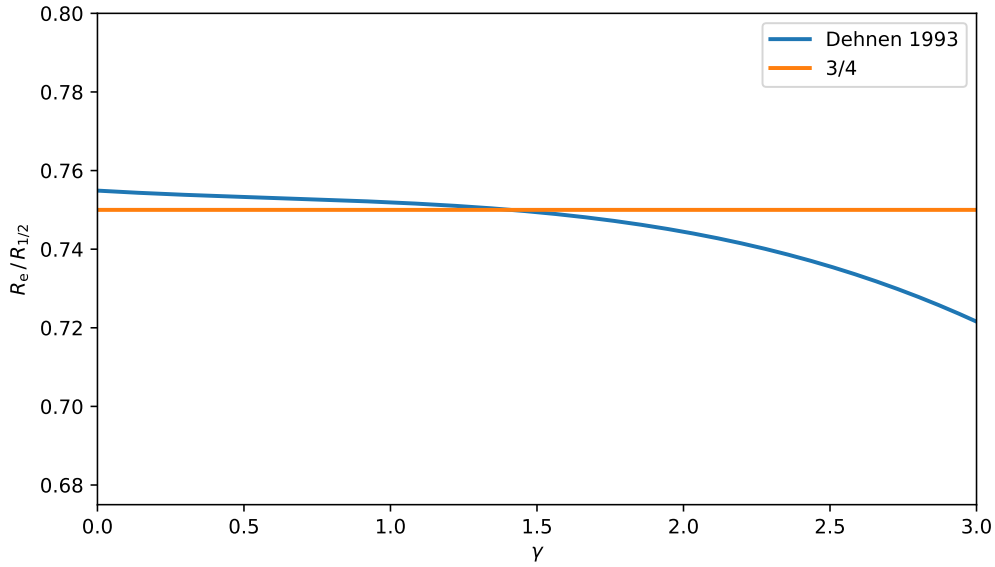

Figure 4.3: Ratio of $R_e/R_{1/2}$ as determined from numerical integration by Dehnen (1993) (Eq. (4.11)) compared to $R_e/R_{1/2} = 3/4$. The relation $R_e = 3/4R_{1/2}$ is seen to approximate the true relation well for $\gamma \lesssim 2.5$. Note the y-axis range.

Additionally, the stellar half-mass radius $R_{1/2}$ is calculated and compared to the observed R_e–$\log(M_\star)$ relation for SDSS DR7 galaxies as discussed in Shen et al. (2003) and Mosleh et al. (2013). The R_e–$\log(M_\star)$ relation is given by Eq. (4.10), where R_e is the effective radius in kpc:

$$R_e = \eta \left(\frac{M_\star}{\mathrm{M}_\odot}\right)^\alpha \left(1 + \frac{M_\star}{M_0}\right)^{\beta-\alpha}. \tag{4.10}$$

From Mosleh et al. (2013), the best-fit values to the parameters of Eq. (4.10) for elliptical galaxies are $\alpha = -0.020$, $\beta = 1.258$, $\log(\eta) = 0.247$, and $\log(M_0/\mathrm{M}_\odot) = 10.673$. The effective radius is then converted to the half-mass radius $R_{1/2}$. Due to the projection of the 3-dimensional mass distribution onto the 2-dimensional plane of the sky and the colour gradient within the galaxy, $R_e \neq R_{1/2}$ (e.g. Suess et al., 2019). From numerical integration, Dehnen (1993) shows that for a density profile as given by Eq. (4.3):

$$\frac{R_e}{R_{1/2}} \approx 0.7549 - 0.00439\gamma + 0.00322\gamma^2 - 0.00812\gamma^3 \pm 7 \times 10^{-4}, \tag{4.11}$$

which may be well approximated (for $\gamma \lesssim 2.5$) by:

$$R_e \approx \frac{3}{4} R_{1/2}, \tag{4.12}$$

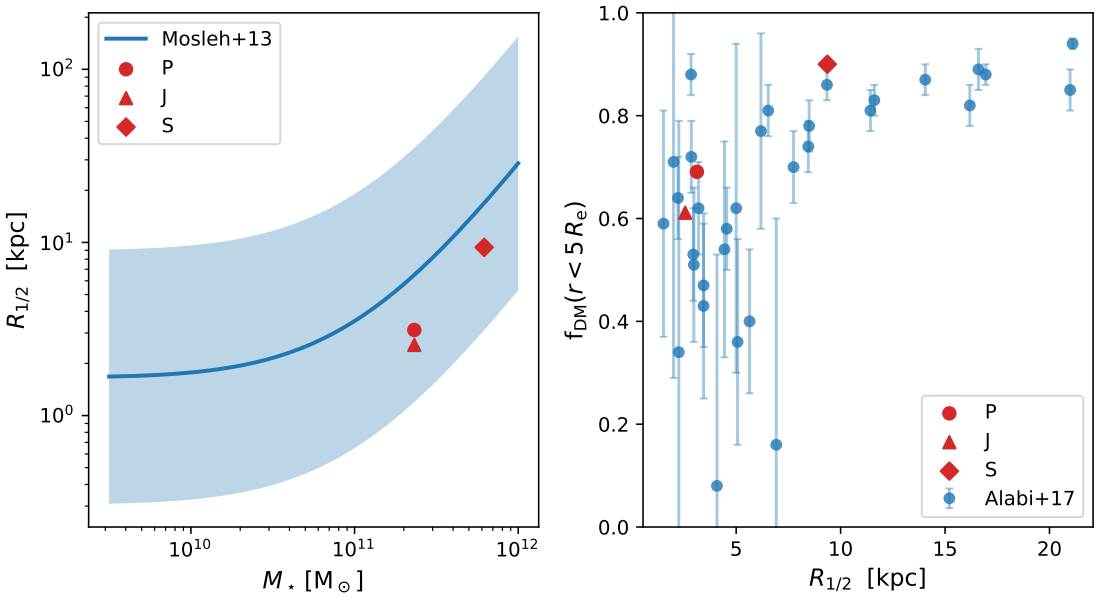

Figure 4.4: *Left:* Stellar half-mass radius as a function of stellar mass, following the relation of Mosleh et al. (2013). The shaded region corresponds to the observed scatter associated with the parameter $\log(\eta)$. *Right:* The half-mass radius as a function of the fraction of dark matter within $5\,R_e$. The blue points correspond to data from galaxies in the SLUGGS survey (Alabi et al., 2017). In both plots, class P, J, and S galaxies are shown by a circle, triangle, and diamond respectively.

and is shown in Fig. 4.3. A plot of $R_{1/2}$–$M_\star$ is shown in the left panel of Fig. 4.4. The shaded region corresponds to the error associated with $\log(\eta)$, namely $\log(\eta) = 0.247 \pm 0.734$.

To determine the stellar half-mass radius of the model galaxy, the cumulative mass function (Eq. (4.7)) is set to $M(r) = \frac{1}{2}M$, from which it follows that:

$$R_{1/2} = a\left(2^{1/(3-\gamma)} - 1\right)^{-1}. \tag{4.13}$$

In addition to Eq. (4.13), the half-mass radius of the model galaxies is also determined by a similar inverse-function search, as was done for determining the halo mass, by evaluating Eq. (4.10) at 10^4 values of $M_\star$. The two methods serve as validation of each other, and are in agreement for all model galaxies. By comparison of the half-mass radius of the model galaxy with Eq. (4.10), the parameters a and $a_{\rm DM}$ can be be constrained. A satisfactory choice of a and $a_{\rm DM}$ is defined when $R_{1/2}$ of the model galaxy lies within the shaded region of Fig. 4.4. Increasing the stellar scale radius results in a larger half-mass radius, and reducing the stellar scale radius results in a complementary smaller half-mass radius.

4.3.2 Inner Dark Matter Fraction

In addition to the constraints on a and $a_{\rm DM}$ provided by the half-mass radius to stellar mass relation, the same parameters may be constrained by investigating the dark matter fraction interior to a given radius. The dark matter fraction is computed by determining the proportion of dark matter to total matter within $5\,R_{\rm e}$, such that:

$$f_{\rm DM}(r < 5\,R_{\rm e}) = \frac{M_{\rm DM}(r < 5\,R_{\rm e})}{M_{\rm DM}(r < 5\,R_{\rm e}) + M_{\star}(r < 5\,R_{\rm e})}. \tag{4.14}$$

Results from the SAGES Legacy Unifying Globulars and GalaxieS (SLUGGS) survey find that ETGs with larger effective radius (and thus half-mass radius) have a greater interior fraction of dark matter compared to those ETGs with smaller effective radii (Alabi et al., 2017), as shown in the right panel of Fig. 4.4. An analogous relation is determined for the dark matter fraction interior to one half-mass radius for a suite of simulations (e.g. Oser et al., 2012; Remus et al., 2017). Using results from the Magneticum Pathfinder simulations (Dolag et al., 2016), the scaling between dark matter fraction and effective radius is found to be linear with coefficient 4.76 (Remus et al., 2017). Knowledge of the central dark matter fraction within the model galaxy allows for an estimation of the scaling radius of the dark matter component $a_{\rm DM}$. As discussed in e.g. Rantala et al. (2018), combining Eq. (4.14) with Eq. (4.7), the scale radius $a_{\rm DM}$ may be given as a function of $f_{\rm DM}$:

$$a_{\rm DM} = R_{1/2}\left(\sqrt{\frac{2M_{\rm DM}}{M_{\star}}\left(\frac{1}{f_{\rm DM}} - 1\right)} - 1\right). \tag{4.15}$$

Comparing the central dark matter fraction of the model galaxy to the results of Remus et al. (2017), combined with the half-mass radius restrictions imposed by Mosleh et al. (2013), allows for the effective constraining of a and $a_{\rm DM}$.

4.3.3 Virial Radius

The virial radius of each model galaxy is computed to apply a cut to the radial distribution of stellar particles. Such a radial cut is necessary to ensure that the representative stellar particles are within a realistic radius of the host galaxy (refer to §2.1.1). Calculation of the virial radius introduces a redshift-dependence of the physical properties of the galaxy into the simulation as a result of the evolution of the cosmological background density (Eq. (4.17)). However, the change in virial radius for a short ($\sim$2 Gyr) simulation time at redshifts $z \lesssim 0.28$ for a fixed galaxy mass is small, and thus the redshift-dependence of the simulation is negligible.

The redshift of the galaxy at the start of the simulation is computed with a conservative estimate of a 1 Gyr simulation time. The redshift-cosmic time relation is taken from Carmeli et al. (2006):

$$z = \sqrt{\frac{2}{\zeta H_0 \cdot t} - 1} - 1, \tag{4.16}$$

where $H_0 = 67.39\,\mathrm{km\,s^{-1}\,Mpc^{-1}}$, and ζ is the conversion factor from standard Hubble constant units to Hz, such that $\zeta = 3.24 \times 10^{-20}$, and the time t is in s.

The virial radius is taken, as per convention, to be the radius within which the mean density ρ of the galaxy is equal to the critical density of the universe in a spatially-flat Λ-CDM cosmology multiplied by the overdensity factor Δ_c of 200:

$$\rho(t) = \Delta_c \frac{3H^2(t)}{8\pi G}, \tag{4.17}$$

where the redshift dependence of the Hubble parameter, assuming Planck cosmology (Planck Collaboration et al., 2018), is taken to be (e.g. Carroll & Ostlie, 2017):

$$\begin{aligned} H(t)^2 &= H_0^2 \left(\Omega_{r,0}(1+z)^4 + \Omega_{m,0}(1+z)^3 + \Omega_{\Lambda,0}\right) \\ &\simeq H_0^2 \left(0.3153(1+z)^3 + 0.6847\right). \end{aligned} \tag{4.18}$$

The virial radius r_{200} of each model galaxy is computed from the particle density ρ of the galaxy using an inverse-function search method, as was done for determining the halo mass.

The half-mass radius $R_{1/2}$ is related to the virial radius r_{200} by:

$$R_{1/2} = (0.015 \pm 0.015 \times 10^{0.2}) r_{200} \tag{4.19}$$

as in Kravtsov (2013). As shown in the left panel of Fig. 4.5, the P and J class model galaxies, with $\log(M_\star/\mathrm{M}_\odot) = 11.365$, are expected to fall within the same region of the $R_{1/2}$–r_{200} parameter space as galaxies observed by Misgeld & Hilker (2011) and Bernardi et al. (2012). Conversely, owing to its larger mass and hence larger virial radius, S class model galaxies are expected to lie beyond the region of Misgeld & Hilker (2011) galaxies, though should still follow the $R_{1/2}$–r_{200} trend of Kravtsov (2013).

4.3.4 SMBH Mass - Stellar Dispersion Relation

As a final assessment of the model galaxy kinematics, the stellar velocity dispersion is computed and compared to results from Ferrarese & Merritt (2000) detailing the

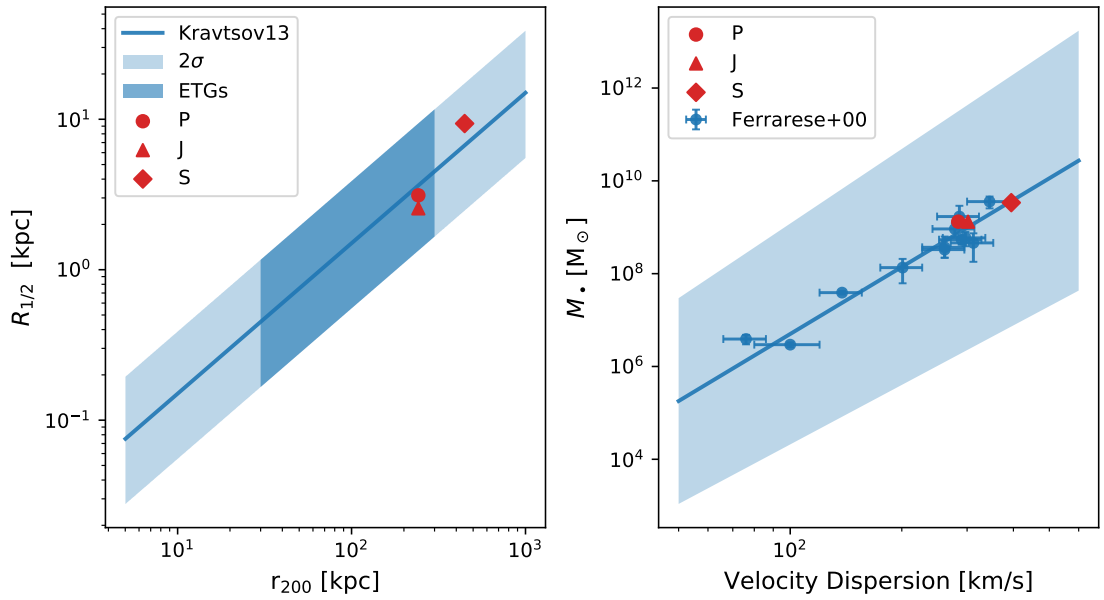

Figure 4.5: *Left:* The $R_{1/2}$–r_{200} relation from Kravtsov (2013). The light blue region indicates the 2σ confidence interval of Eq. (4.19). Typical elliptical galaxies (Bernardi et al., 2012; Misgeld & Hilker, 2011) are found within the darker-shaded region. *Right:* The $M_\bullet$–σ relation shown for galaxies in the original work of Ferrarese & Merritt (2000). In both plots, class P, J, and S galaxies are shown by a circle, triangle, and diamond respectively.

SMBH mass - velocity dispersion relation (Gebhardt et al., 2000; Tremaine et al., 2002; Graham et al., 2011; McConnell & Ma, 2013). The line of sight (LOS) velocity is determined by constructing a hemispherical grid about the galaxy, which defines 100 uniformly distributed observation points in angular space at a radial distance of 10^3 kpc from the galaxy SMBH, as visualised in Fig. 4.6. The LOS velocity is calculated as the scalar projection of the stellar velocity $\boldsymbol{v}_\star$ onto the observer (e.g. Binney & Tremaine, 2008):

$$v_{\mathrm{LOS}} = -\frac{\boldsymbol{v}_\star \cdot \boldsymbol{x}_{\mathrm{obs}}}{||\boldsymbol{x}_{\mathrm{obs}}||}. \tag{4.20}$$

The LOS velocity dispersion is consequently calculated as the standard deviation of the sample of LOS velocities determined through the observation sampling, and is denoted by σ. The SMBH mass is plotted against the calculated LOS velocity dispersion and compared to the data of Ferrarese & Merritt (2000), as depicted in the right panel of Fig. 4.5. The relation, with error shown as the shaded region, is described by:

$$\log(M_\bullet/\mathrm{M}_\odot) = 4.80(\pm 0.54)\log(\sigma) - 2.9(\pm 1.3), \tag{4.21}$$

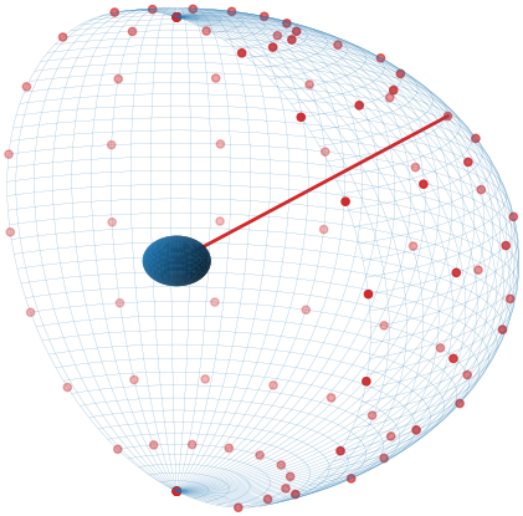

Figure 4.6: Observation points (red) are generated in 100 uniformly distributed locations at a radial distance of 10^3 kpc from the model galaxy (central blue sphere) to determine the line of sight stellar velocity dispersion. An example line of sight vector is shown by the red line.

where σ is in units of km s^{-1}. The model galaxies are required to lie within the error bounds of Fig. 4.5. It is found that modelled galaxies of class P typically lie slightly above the relation of Eq. (4.21), whereas galaxies of class J typically lie slightly below the relation of Eq. (4.21). In all cases, the modelled galaxies have velocity dispersion comparable to the most massive of the Ferrarese & Merritt (2000) sample.

4.4 Determining the Softening Lengths

Critical to the accuracy of the model galactic dynamics is appropriate choice of gravitational softening length ϵ_i for each component. To determine the softening length for each particle species, 250 particles of each species are drawn at random from the model. The distance to the nearest-neighbour (of the same species) $r_{\rm NN}$ of particle i is determined by restricting the search area to a cube centred on the particle with side length 0.28 kpc for stellar particles, and 10 kpc for DM particles. If no neighbours are found within the volume (as may be the case in particular for DM particles at large radii), the side length of the cube is doubled; this procedure is iterated for a maximum of ten repetitions until a neighbour is found. The nearest-neighbour distance is plotted as a function of particle distance from the SMBH in Fig. 4.7. Taking the mean nearest-neighbour distance, and dividing by 50 (see §3.3)

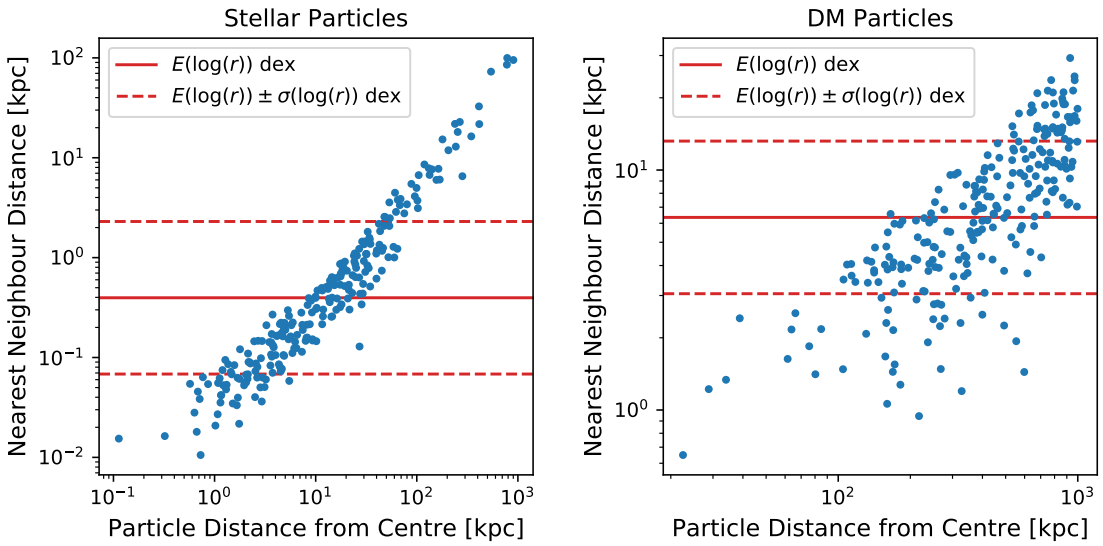

Figure 4.7: Nearest-neighbour distance for stellar particles (left) and DM particles (right) for model galaxy S1. The mean nearest-neighbour distance is indicated by the solid red line, with 1σ spread in the logarithm indicated by the dotted red lines.

allows for a motivated choice of softening length. The softening lengths are found to be centred about $\epsilon_\star \simeq 6 \times 10^{-3}\,\mathrm{kpc}$ and $\epsilon_{\mathrm{DM}} \simeq 0.1\,\mathrm{kpc}$, consistent with the choices of Rantala et al. (2017).

4.5 Stability Tests

Before merging two galaxies, each galaxy is required to demonstrate stable dynamics. The low resolution realisation of each model galaxy class (P1a, J1, S1) is run in isolation for 250 Myr, and the variation in mass with radius $\frac{dM(r)}{dt}$ is determined. An example plot for galaxy P1a is shown in Fig. 4.8. The species population is first trimmed to include only those particles with radial distance within the 95% quantile of the species. The radius containing 10%, 30%, 50%, and 80% of the species mass is measured throughout the simulation. The relative change in final radius for stellar particles is $\Delta r \leq 1.440\%$. The relative change in final radius for DM particles varies from $\Delta r \leq 1.97\%$ for galaxy P1a to $\Delta r \leq 4.909\%$ for the larger galaxy S1. Thus, the stability of the three component models are validated, and appropriate to be used in merger simulations.

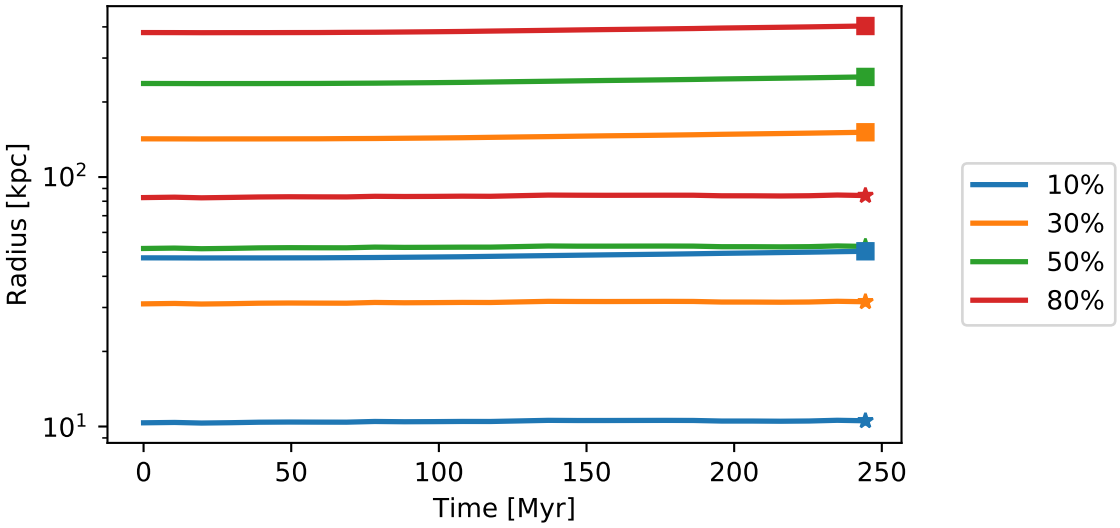

Figure 4.8: Stability of isolated galaxy P1a. Blue lines indicate the radius enclosing 10% of the species mass, orange lines 30%, green lines 50%, and red lines 80%. Stellar particle stability is demonstrated by starred lines, whereas DM particle stability is shown as boxed lines.

4.6 Merger Conditions

Fourteen galaxies are created following the method outlined in §4.2, and are classified into the appropriate class as determined by their physical parameters. Additionally, three different stellar mass resolutions are studied for each class, as indicated by the suffix number of the galaxy identifier. For the lower mass (P and J) class galaxies, '1' corresponds to $N_\star \sim 1.0 \times 10^5$ ($N_{\rm DM} \sim 5.0 \times 10^4$), '2' to $N_\star \sim 5.0 \times 10^5$ ($N_{\rm DM} \sim 6.0 \times 10^4$), and '3' to $N_\star \sim 1.0 \times 10^6$ ($N_{\rm DM} \sim 1.0 \times 10^5$). To ensure equal particle masses in unequal mass mergers, the corresponding number of particles in each resolution model for class S galaxies is $N_\star \sim 2.6 \times 10^5$ ($N_{\rm DM} \sim 5.0 \times 10^5$), $N_\star \sim 1.3 \times 10^6$ ($N_{\rm DM} \sim 6.0 \times 10^5$), and 03 to $N_\star \sim 2.7 \times 10^6$ ($N_{\rm DM} \sim 1.0 \times 10^6$). For select low and medium resolution galaxies, different realisations of the same galaxy albeit with a changed random seed used to determine the initial mass distributions are created; these galaxies are labelled with the additional suffix a, b, c, or d.

The merger progenitors are presented in Table 4.2 for the low resolution study, Table 4.3 for the medium resolution study, and Table 4.4 for the high resolution study.

Progenitor 1			Progenitor 2		
ID	$M_{\bullet,1}/m_{\star,1}$	γ_1	ID	$M_{\bullet,2}/m_{\star,2}$	γ_2
P1a	570	1.6	P1b	570	1.6
P1a	570	1.6	P1c	570	1.6
P1b	570	1.6	P1c	570	1.6
P1b	570	1.6	P1d	570	1.6
P1a	570	1.6	S1	1463	1.6
P1a	570	1.6	J1	570	1.8
J1	570	1.8	S1	1463	1.6

Table 4.2: Low resolution study, with stellar particle mass $m_\star = 2.317 \times 10^6\,\mathrm{M}_\odot$.

Progenitor 1			Progenitor 2		
ID	$M_{\bullet,1}/m_{\star,1}$	γ_1	ID	$M_{\bullet,2}/m_{\star,2}$	γ_2
P2a	2846	1.6	P2a	2846	1.6
P2a	2846	1.6	P2b	2846	1.6
P2a	2846	1.6	S2a	7316	1.6
P2a	2846	1.6	S2b	7316	1.6
P2a	2846	1.6	J2	2846	1.8
J2	2846	1.8	S2a	2846	1.6

Table 4.3: Medium resolution study, with stellar particle mass $m_\star = 4.635 \times 10^5\,\mathrm{M}_\odot$.

Progenitor 1			Progenitor 2		
ID	$M_{\bullet,1}/m_{\star,1}$	γ_1	ID	$M_{\bullet,2}/m_{\star,2}$	γ_2
P3	5693	1.6	P3	5693	1.6
P3	5693	1.6	S3	14635	1.6
P3	5693	1.6	J3	5693	1.8
J3	5693	1.8	S3	14635	1.6

Table 4.4: High resolution study, with stellar particle mass $m_\star = 2.317 \times 10^5\,\mathrm{M}_\odot$.

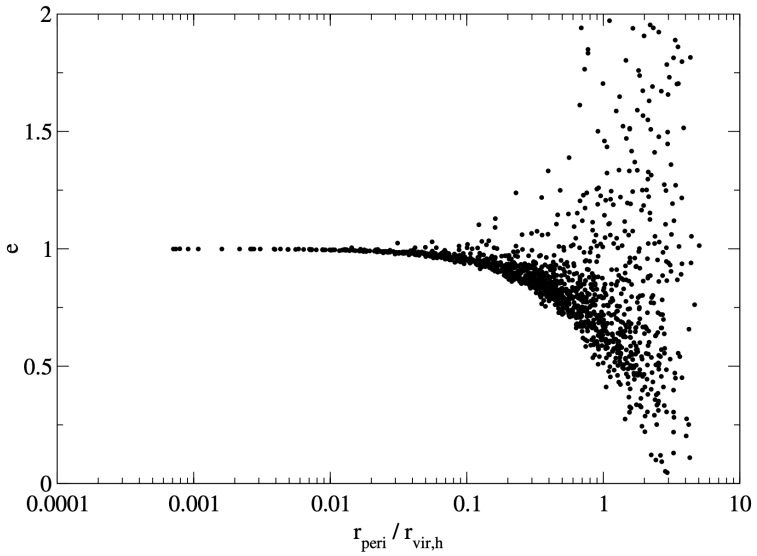

Figure 4.9: Eccentricity e as a function of pericentre distance $r_{\rm peri}$ relative to the halo virial radius $r_{\rm vir,\,h}$ for merging halos for simulated major mergers. Credit: Khochfar & Burkert, A&A, 445, 403, 2006, reproduced with permission © ESO.

4.7 Orbital Parameters

In each of the simulated mergers, the member galaxies are set on a nearly-parabolic merger orbit such that the eccentricity is $e \simeq 1$, following Rantala et al. (2018). An exact parabolic orbit is well defined only for a point-particle, and not an extended mass object consisting of a number of particles, such as a galaxy. In the limiting case of an exact parabolic orbit, the energy $E = 0$, from which:

$$E = \frac{1}{2}\mu\dot{r}^2 - \frac{GM_1M_2}{r} \implies \dot{r} = \sqrt{\frac{2G(M_1 + M_2)}{r}}, \tag{4.22}$$

where M_1 and M_2 are the virial masses of the systems, and $r \equiv |r_1 - r_2|$. Thus, the merger system may be described with two values of r: the initial separation r_0, and the separation at the first pericentre passage $r_{\rm peri}$. The respective velocities $\dot{r}_0$ and $\dot{r}_{\rm peri}$ of the system are given by Eq. (4.22). Fig. 4.9 depicts the relation between orbital eccentricity and pericentre distance for simulated major mergers, as presented in Khochfar & Burkert (2006). For a parabolic orbit to ensue, it is visible that $r_{\rm peri}/r_{\rm vir}$ must remain below 0.1. A smaller pericentre separation results in less scatter in the orbital eccentricity about $e = 1$ compared to larger pericentre distances, providing an upper constraint on $r_{\rm peri}$. A lower constraint on the pericentre distance is provided by the pericentre velocity $\dot{r}_{\rm peri}$, which (from Eq. (4.22)) increases asymptotically as $r_{\rm peri}$ decreases. As a particle p_i passes through a neighbourhood of particles p_j, the dynamical friction experienced by p_i is smaller

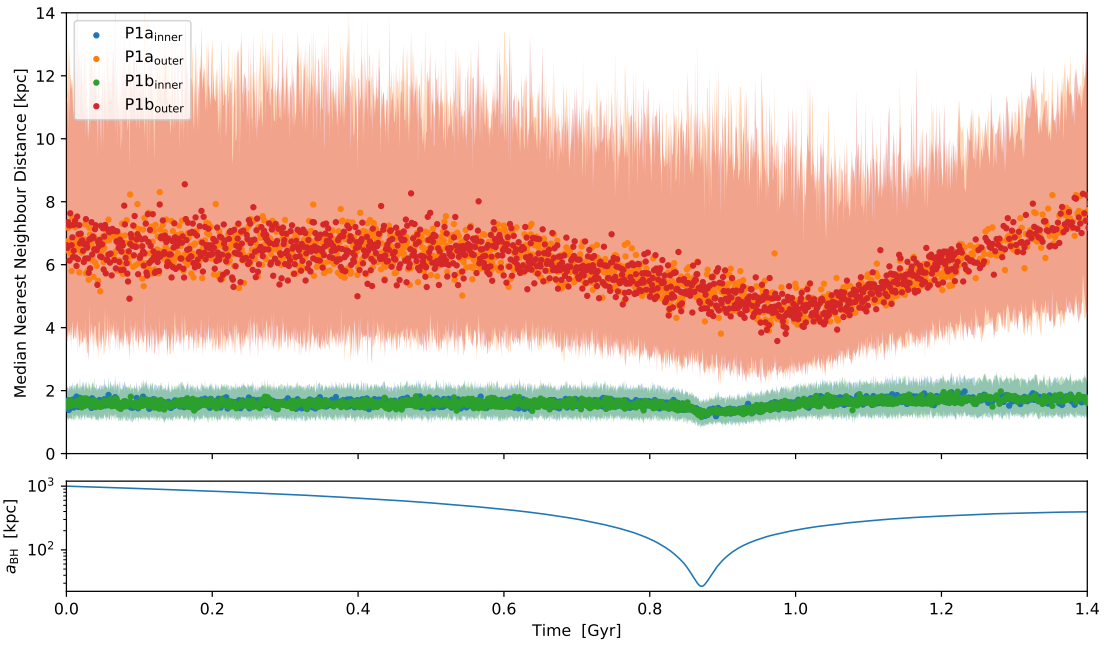

Figure 4.10: *Top:* Median nearest-neighbour distance for DM particles in the trial merger of P1a and P1b. Each galaxy is divided into two regions, an inner and outer region defined by the division radius $r_{\rm div} = 10R_{1/2}$. The shaded area corresponds to the interquartile range of nearest-neighbour distance. *Bottom:* Radial separation of the two SMBHs.

with increasing velocity $\dot{r}_{\rm peri}$ (refer to Eq. (2.44) §2.2.4). As a consequence of the low dynamical friction, the parent bodies of particles p_i and p_j will likely not merge, but rather flyby each other. To ensure a merger event occurs, Eq. (2.44) implies that $\dot{r}_{\rm peri} \sim \sigma$. The criterion:

$$\dot{r}_{\rm peri} < 10^{0.5}\sigma \tag{4.23}$$

is adopted to constrain the maximum velocity at first pericentre, from which the minimum pericentric distance $r_{\rm peri}$ is calculated using Eq. (4.22). The pericentric distances for the simulated mergers range from 10 kpc–25 kpc, dependent on the radial extent of the more massive of the two systems in the simulation. In practice, the choice of pericentre distance corresponds to $r_{\rm peri} \sim 2R_{1/2}$, consistent with the studies of Bois et al. (2011) and Rantala et al. (2017, 2018).

The choice of initial separation r_0 was determined by running a single simulation of the P1a+P1b merger system. The system was configured to have an initial separation equal to the sum of the maximum radial extent of the DM halos; the consequential initial separation of the two SMBHs was of the order 10^3 kpc. The pericentre distance was set to a small value of $1.5R_{1/2} \sim 5$ kpc, and the system integrated for 1.4 Gyr. A bound binary system did not develop in the simulation.

The median nearest-neighbour DM particle distance $\bar{r}_{\rm NN}$ was then studied at each time step for both systems. To reduce the error in sampling the nearest-neighbour distance (refer to Fig. 4.7 for the dependence of the nearest-neighbour distance on the radial distance of the particle), each galaxy is divided into an inner and an outer region. The division radius, $r_{\rm div}$ is defined as:

$$r_{\rm div} = 10 R_{1/2}, \tag{4.24}$$

which for the P1 model galaxies equates to $r_{\rm div} \sim 30\,{\rm kpc}$. The nearest-neighbour distance of the two regions of both galaxies is then sampled with 200 randomly-selected DM particles, following the procedure presented in §4.4. The evolution of $\bar{r}_{\rm NN}$ is presented in the top panel of Fig. 4.10. The bottom panel of Fig. 4.10 depicts the radial separation of the two SMBHs in the merger system. Critically, DM particles beyond $r_{\rm div}$ experience minimal evolution in $\bar{r}_{\rm NN}$ in the outer regions, however the interquartile range typically extends some 8 kpc. Taking all outer region measurements at t <0.1 Gyr, the median $\bar{r}_{\rm NN}$ is found to be 6.506 kpc, compared to 7.524 kpc for measurements at t >1.3 Gyr.

All sampled points experience a decrease in $\bar{r}_{\rm NN}$ following the closest approach of the SMBHs. For sampled points within the division radius $r_{\rm div}$, the maximum decrease in $\bar{r}_{\rm NN}$ is less than, and occurs earlier than, the maximum decrease in $\bar{r}_{\rm NN}$ for points sampled beyond the division radius. The median nearest-neighbour DM particle distance decreases by ∼0.3 kpc for inner DM particles, compared to ∼1.5 kpc for outer DM particles. There is no apparent change in the magnitude of the interquartile range of $\bar{r}_{\rm NN}$ in either set of sampled points during the closest approach of the SMBHs. The dip in $\bar{r}_{\rm NN}$ is a result of the two galaxies passing through each other causing a temporary density increase.

As evidenced by the constancy of $\bar{r}_{\rm NN}$ for the outer regions, there is no need for initialising the merger system to have an initial separation where the DM halos do not overlap. The merger system can thus be confidently initialised with a value of r_0 in which there is significant overlap of the DM halos of the two galaxies. Consequently, the initial separation of all merger systems is set to a 95% overlap of the DM halos (see Fig. A.1), resulting in $r_0 = 50\,{\rm kpc}$ for mergers not involving class S galaxies, and $r_0 = 75\,{\rm kpc}$ for mergers that do contain a class S galaxy. The reduced initial separation ensures a time of first pericentre passage $t_{\rm peri}$ <0.08 Gyr, compared to $t_{\rm peri}$ ∼0.8 Gyr for a merger realisation in which the DM halos do not overlap. Consequently, the simulations are numerically more feasible to perform, as the integration time to obtain a merger event is significantly reduced.

5. KETJU Simulations: Analysis

This chapter presents the analysis of the seventeen major-merger events completed with the KETJU code. First, a qualitative description of the chief stages of the SMBH coalescence process is provided. Secondly, the system parameters of simulations with different mass resolutions of the same physical initial conditions are contrasted and compared to determine the effect of mass resolution on the merging of the SMBH binary. Additionally, comparison of the same parameters between different physical conditions are made to explore the similarities and differences between the four simulation suites. Furthermore, a brief discussion of the GW signal from an equal mass SMBH binary is presented. Finally, an analysis of the large-scale kinematics of the highest resolution realisation of each physical system is performed, and discussed with respect to observational results. Surprisingly, not all simulations resulted in the coalescence of the SMBH binary, even at mass resolutions deemed 'sufficient' (e.g. Nasim et al., 2020). This single observation indicates that the Final Parsec Problem is highly sensitive to both the initial conditions of the system and the ensuing interactions of the SMBH binary with the stellar particles in the immediate vicinity.

5.1 Qualitative Overview

A qualitative description of the three principal interaction stages for the coalescence of a SMBH binary is shown in Fig. 5.1, which depicts the state of the high-resolution, equal mass, equal density (P3+P3) merger system at three different times. In the top panel of Fig. 5.1, the nuclei of both progenitor galaxies are distinct, and the SMBH binary forms a bound binary in the following 1 Myr (see Fig. A.2). The SMBH separation is some hundreds of parsecs, and each SMBH is surrounded by a large number of stellar particles. The large number of stellar particles, each with a mass of $2.317 \times 10^5\,\mathrm{M}_\odot$, provides a dynamical friction force that torques the SMBHs towards the centre of mass. Critically, the dynamical friction from stars is efficient only as

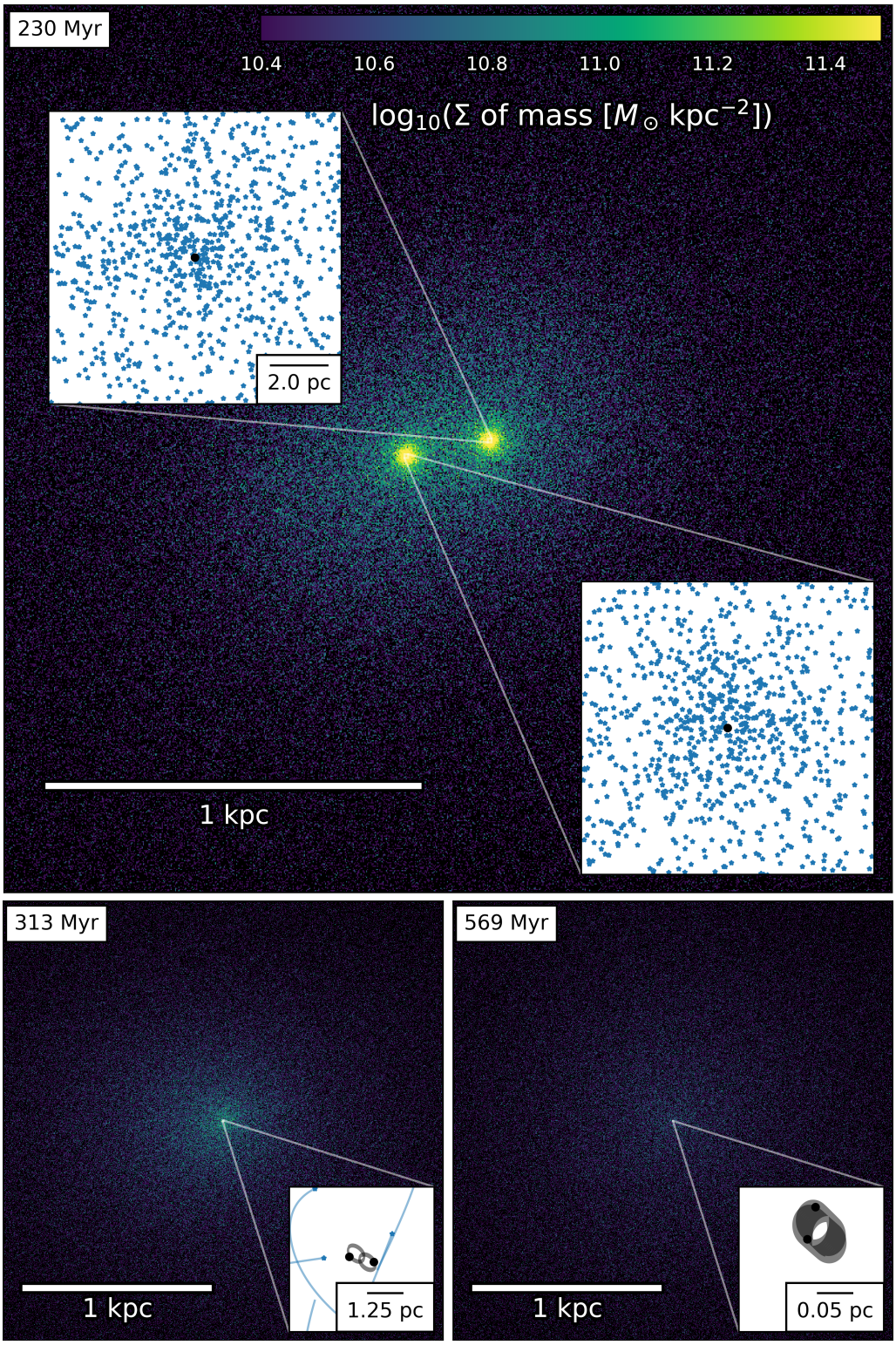

Figure 5.1: The three primary interaction stages of the SMBH coalescence for the high-resolution, equal mass, equal density merger P3+P3. *Top:* The SMBHs (black) are brought together through dynamical friction interactions with stars (blue) of the second galaxy. *Bottom left:* The SMBH binary is brought to within parsec-scale separation through three-body interactions with stars in the nearby vicinity. *Bottom right:* The SMBH binary finally coalesces through emission of gravitational waves at sub-parsec scales. In all panels, the main figures have a consistently scaled surface mass density (colour bar at top), and are aligned with the stellar angular momentum.

the relative velocity between the SMBHs is low (refer to §2.2.4). The surface mass density within the nucleus of each progenitor is in excess of $2.5 \times 10^{11}\,\mathrm{M}_{\odot}\,\mathrm{kpc}^{-2}$, and thus allows for the dynamical friction to bring the SMBH binary to parsec-scale separations.

In the bottom left panel of Fig. 5.1, taken 83 Myr after the top panel, the disappearance of the distinctly separate nuclei is immediately apparent. The resulting nucleus has diffused to a maximum surface mass density of $\sim 6.3 \times 10^{10}\,\mathrm{M}_{\odot}\,\mathrm{kpc}^{-2}$. The SMBHs have now formed a tightly bound binary that is driven to smaller orbital separation through three-body interactions with stars in the immediate vicinity of the binary. Stellar interactions, with the stars seen to be primarily on radial orbits, are shown in the inset panel. Three-body interactions drive the binary to sub-parsec separations, assuming the loss cone of the binary contains stars. It is in the three-body interaction phase that the FPP may arise, if all stars able to interact with the binary are ejected from the loss cone. In the merger simulation shown, the FPP was not encountered.

Finally, in the bottom right panel of Fig. 5.1, the SMBH binary enters the GW emission phase. The timescale of the three-body interaction phase is dramatically longer than both the dynamical friction phase and the GW emission phase, as indicated by the binary entering the GW emission regime more than 250 Myr after the plot in the bottom left panel of Fig. 5.1. The nucleus of the merger remnant has diffused further to $\sim 4.0 \times 10^{10}\,\mathrm{M}_{\odot}\,\mathrm{kpc}^{-2}$. The inset figure shows the orbit of the SMBH binary integrated for a short time prior to the coalescence of the binary. As the emission of GW radiation increases, the binary is driven to lower orbital eccentricity (see Fig. 5.2).

5.2 Equal Mass, Equal Density Mergers

The equal mass, equal density merger simulations are denoted as P+P mergers: this terminology shall be used throughout. In total, six P+P mergers of differing resolutions are presented. If the binary eccentricity circularised ($e \to 0$) prior to the GW regime, the simulation was discontinued, owing to the dramatically increased coalescence time (refer to §2.3.1).

The evolution of the orbital parameters of the SMBH binary are presented in Fig. 5.2, with the inverse semimajor axis and eccentricity shown in the top and bottom panels respectively. The time at which the SMBH binary becomes hard ($a = a_{\mathrm{h}}$, Eq. (2.52)) is indicated by a point. The mean hardening radius is found to

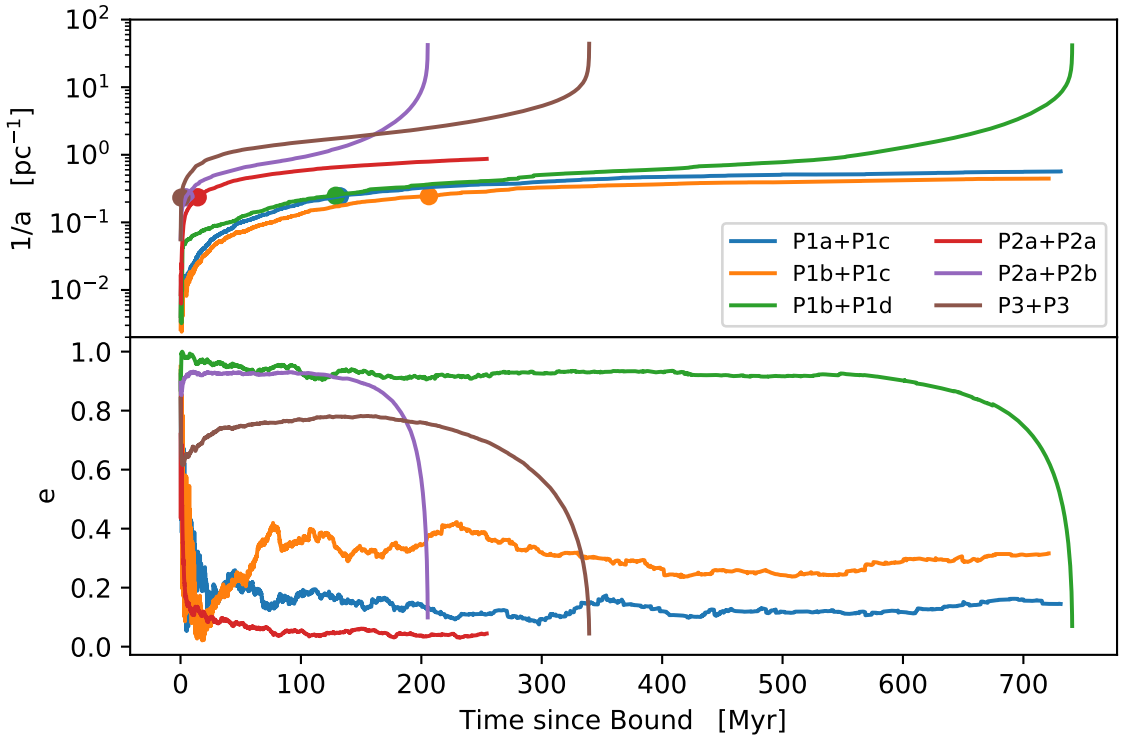

Figure 5.2: SMBH binary orbital parameters of the P+P suite. *Top:* The inverse semimajor axis $1/a$ as a function of time. All times are shifted such that t_0 corresponds to the time when the SMBHs formed a bound binary. The points indicate where $a = a_\mathrm{h}$, i.e. the time when the binary becomes hard. Simulations that resulted in SMBH coalescence are clearly depicted by the upturn in $1/a$. *Bottom:* The eccentricity e as a function of time, with the time shifted as in the top panel. Binaries are initially on eccentric orbits ($e \sim 1$). Simulations that resulted in SMBH coalescence are characterised by a high eccentricity that falls in a rapid concave-down curve. The number suffix indicates the resolution of the simulation, with a letter suffix indicating a differing random seed.

be $a_\mathrm{h} = (4.18 \pm 0.10)\,\mathrm{pc}$ across all P+P simulations, indicating limited resolution-dependence. A binary that coalesces is characterised by an inverse semimajor axis that increases asymptotically as a result of the semimajor axis $a \to 0$. Generally, higher resolution (P2+P2, P3+P3) mergers coalesce on timescales much shorter than the low resolution (P1+P1) systems. Even so, the effects of stochasticity are visible for P2+P2 mergers as well as P1+P1 mergers. Stochasticity is introduced through the Monte Carlo sampling of the initial phase space distribution function. Simulations of decreasing resolution attribute a larger mass to each particle, thus increasing the degree to which a single particle may influence the local dynamics. If the sampling of the phase space is poor, the number of particles within the binary loss cone can be quickly depleted, even though the mass of a single particle is large.

The depleted loss cone consequently prevents the SMBH binary from losing enough energy and angular momentum for GW emission to be efficient. This effect can be seen most clearly in the P1+P1 simulations, where the inverse semimajor axis stalls at $\sim$0.1 pc^{-1} for both P1a+P1c and P1b+P1d. The P1b+P1d system temporarily stalls at 0.1 pc^{-1} before a small number of three-body interactions are able to drive the SMBH binary to sub-parsec separations. Comparing the inverse semimajor axis of P2a+P2a to P1b+P1d at early times (t <200 Myr), the inverse semimajor axis of the former is seen to be greater than the latter, yet P2a+P2a does not undergo coalescence. A similar comparison can be made between P2a+P2b and P3+P3: P2a+P2b initially has a smaller inverse semimajor axis, yet undergoes coalescence $\sim$100 Myr prior to P3+P3. From these observations, it may be concluded that the inverse semimajor axis of the binary is not the dominant parameter dictating whether or not a SMBH binary coalesces. Indeed, the decisive parameter in the fate of a SMBH binary is the orbital eccentricity.

The orbital eccentricities of the P+P suite are shown in the bottom panel of Fig. 5.2. Immediately apparent is the characteristic concave-down curve characterising GW emission and consequent binary coalescence. The eccentricity curves that result in binary coalescence are seen to maintain a high eccentricity for much of the simulation, in excess of $e \sim 0.7$ as in the case of the P3+P3 merger. The timescale between the binary becoming bound and the GW regime being entered varies between the three simulations P1b+P1d, P2a+P2b, and P3+P3. Of particular interest for the FPP is the eccentricity curve of P1b+P1d, which remains at high eccentricities for more than 600 Myr after the binary becoming bound. The long duration of the binary is explained by a deficit in stellar particles that the binary is able to interact with. The P1b+P1d simulation likely had a loss cone that was refilled after spending much of the bound-time emptied, allowing the binary to finally achieve coalescence. The shorter timescales of P2a+P2b and P3+P3 are readily explained by the increased number of stellar particles, albeit with a decreased particle mass, that are able to interact with the SMBH binary. The P2a+P2b simulation displays an eccentricity that remains largely constant until entering the GW regime, whereas the eccentricity of P3+P3 gently increases until $t \sim$150 Myr, after which the eccentricity decreases as GW emission becomes dominant. Investigation of the stellar kinematics about the SMBH binary indicates a kinematically-distinct core (KDC), with the SMBH binary at the centre of the core (see Fig. A.3). The counter-rotating stellar structure may be responsible for the subtle initial eccentricity increase in P3+P3, in agreement with three-body experiments by Sesana et al.

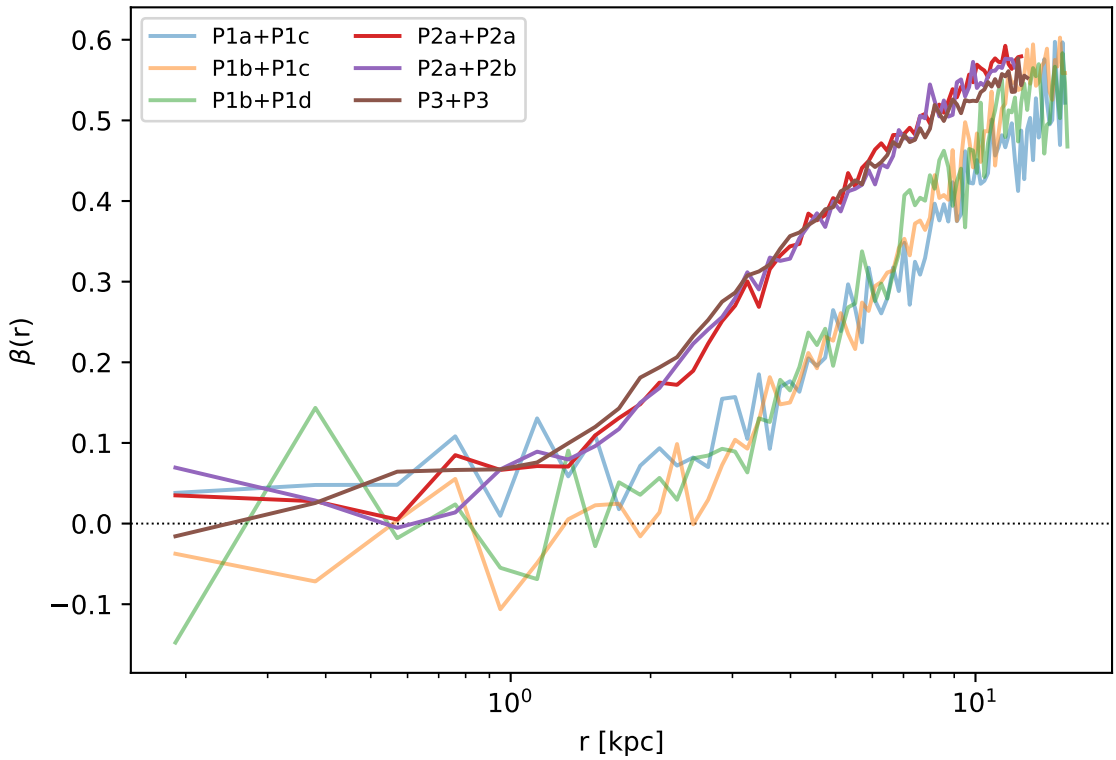

Figure 5.3: Velocity anisotropy parameter $\beta(r)$ as a function of radius for the P+P suite. Low resolution simulations are faded for clarity. The decreasing $\beta(r)$ towards the centre of the merger remnant is evidence for core-scouring by the SMBH binary, leading to an observational luminosity-deficit in the galactic centre.

(2011). The P2a+P2b merger does not display a KDC, and also has a constant eccentricity for the duration of the three-body interaction phase. In the P1b+P1d and P2a+P2b simulations, the GW-dominant phase lasts for approximately 50 Myr, compared to ∼150 Myr for the P3+P3 merger.

Half of the P+P simulations demonstrate a drastic initial decrease in eccentricity that cannot be interpreted as GW-emission, but rather circularisation driven by stellar interactions. At such low eccentricities, it is extremely difficult for the SMBH binary to interact with a sufficient number of stars to lose the required orbital energy and angular momentum. All of P1a+P1c, P1b+P1c, and P2a+P2a, had binaries that stalled in the FPP.

The interaction of the SMBH binary with the stellar population may be explored through the velocity anisotropy parameter within a given maximum radius, here taken to be twice the half mass radius of the galaxy measured from the centre

of mass of the SMBH binary[1]:

$$\beta(r) = 1 - \frac{\sigma_\theta^2 + \sigma_\phi^2}{2\sigma_r^2}, \tag{5.1}$$

where σ is the stellar velocity dispersion in spherical coordinates, as in Binney & Tremaine (2008). Regions with stars on a purely radial orbit have $\beta(r) = 1$, and regions with stars with purely tangential motion have $\beta(r) \to -\infty$. The radial bins have a fixed bin width of 0.19 kpc motivated by observations of NGC 1600 by Thomas et al. (2016), used also in the work of Rantala et al. (2018) against which the results of this work are compared. The P+P simulation suite demonstrate a $\beta(r)$ that increases with radius, and is shown in Fig. 5.3. Most of the P+P simulations have central regions with little bias to radial or tangential stellar orbits, with the exception of P1b+P1d, which demonstrates a tangentially-biased stellar population at the centre. Central-circular stellar orbits are evidence of core-scouring by the SMBH binary (e.g. Rantala et al., 2018), often observed as a luminosity-deficit in the core of massive ETGs (e.g. Thomas et al., 2016). The $\beta(r)$ profile of P1b+P1d is not dissimilar to that observed for simulated ETGs with less-steep density profiles in Rantala et al. (2018), however there is a strong tendency for an increased central-$\beta(r)$ value compared to Rantala et al. (2018). Also shown in Fig. 5.3 is the tendency for low resolution simulations to have a smaller $\beta(r)$ value for a given radius compared to medium and high resolution simulations. The reduced tendency of low resolution simulations to have radial stellar orbits may consequently reduce the number of interactions the SMBH binary can undergo, however stellar particles more than 1 kpc from the binary are not expected to affect its evolution to any great extent. The variation in the $\beta(r)$ profile for the low resolution simulations (particularly at small radii) again highlights the stochasticity associated with too few particle numbers in the merger simulations.

Finally, the velocity of stars crossing a thin shell about the SMBH binary is investigated. The stellar mass crossing a 30 pc shell after the binary has become bound is depicted in the top row of Fig. 5.4, from which the stochasticity of the low resolution simulations is seen as more step-wise compared to the smooth evolution of the medium and high resolution simulations. For all P+P simulations, the incoming stellar mass peaks just after the binary is formed at $\sim 10^8\,\mathrm{M}_\odot$, and is shortly followed by a near-identical quantity of mass outgoing through the shell. The amount of mass

[1]The CoM of the SMBH binary is used in preference to the CoM of the entire system owing to the system CoM being displaced from the region of highest stellar density by outlying DM particles (refer to Fig. A.4).

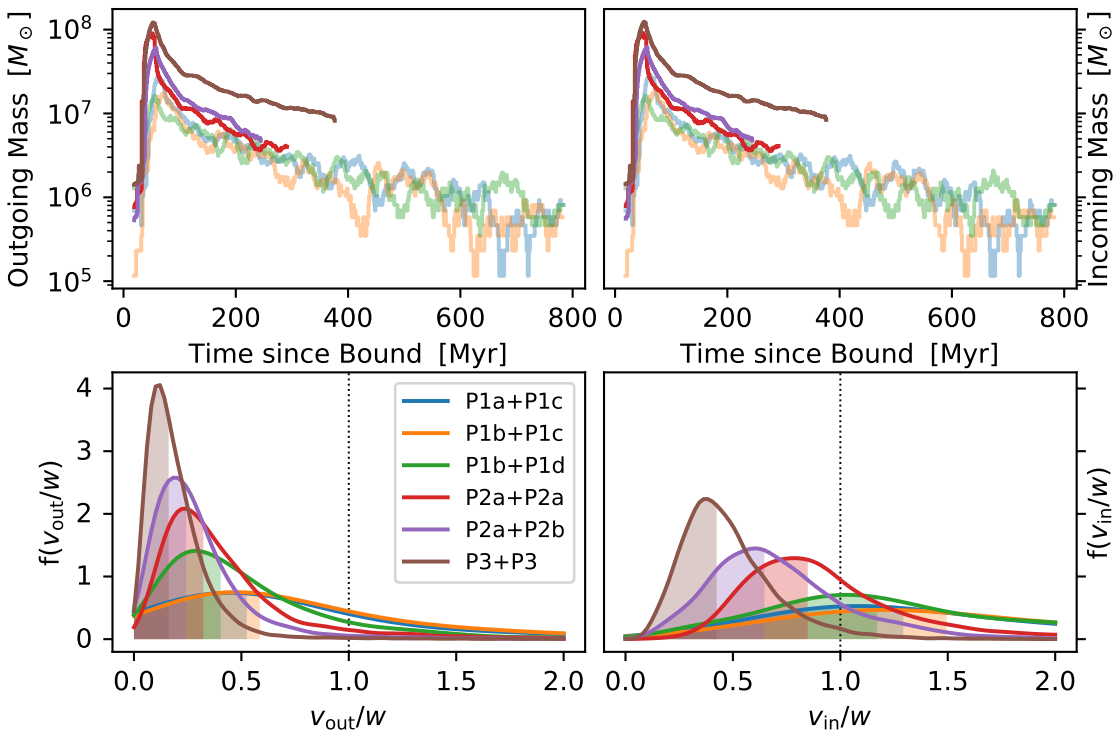

Figure 5.4: Velocity analysis of stellar particles crossing a 30 pc shell about the SMBH binary. Low resolution simulations are faded for clarity. *Top left:* Stellar mass outgoing through the shell. *Top right:* Stellar mass incoming through the shell. *Bottom left:* Velocity distribution of stars outgoing through the shell relative to the watershed velocity w. *Bottom right:* Velocity distribution of stars incoming through the shell relative to w. In both bottom panels, the shaded region corresponds to the 50% quantile of the respective velocity distribution.

flowing through the shell in both directions decreases steadily as time progresses, clearly exemplifying the scouring of the immediate vicinity of stars and the emptying of the loss cone. There is a tendency for high resolution simulations to have an increased mass flow, which is also seen in the instantaneous stellar mass within the Ketju region in Fig. A.5.

The bottom row of Fig. 5.4 shows the kernel density estimates (KDE) velocity distributions of the stellar particles crossing the 30 pc shell relative to the watershed velocity w. The watershed velocity is proportional to the orbital velocity of the binary V_{bin}, and is given by:

$$w \approx 0.85 \cdot \sqrt{\frac{M_{\bullet,1}}{M_{\bullet,1} + M_{\bullet,2}}} V_{\mathrm{bin}} = 0.85 \cdot \sqrt{\frac{GM_{\bullet,2}}{a}}, \tag{5.2}$$

where a is the semimajor axis of the binary and $M_{\bullet,2} \leq M_{\bullet,1}$ (Quinlan, 1996). The effect of orbital eccentricity is inconsequential in determining w, thus allowing for the simplifying assumption of all SMBH binary orbits being circular (Mikkola &

Valtonen, 1992; Quinlan, 1996). Scaling the stellar velocity by the watershed velocity identifies the proportion of stars which can gain energy from the binary ($v < w$) and the proportion which can lose energy to the binary ($v > w$). All stellar particles that cross the 30 pc shell after the SMBH binary is bound are included in the velocity distribution estimates: the effect of the simulation timespan was separately investigated by including stellar crossings occurring before 200 Myr following the binary becoming bound. No dependence was observed, and thus the full set of stellar crossings is used in Fig. 5.4. The (unscaled) outgoing stellar velocity demonstrates a narrower range of velocities compared to the incoming stellar velocity, and peaks at a value of $\sim$400 km s^{-1} independent of mass resolution (see Fig. A.7). However, the scaled velocities in Fig. 5.4 demonstrate a clear resolution dependence that offers a potential explanation for which systems resulted in SMBH coalescence. Increasing the mass resolution of the simulation increases the number of interactions the SMBH binary can undergo with stars that may gain energy from the binary. All low resolution simulations have their median $v_{\rm in}/w$ greater than unity, i.e. less than half of the stellar interactions result in a hardening of the SMBH binary. In the P3+P3 simulation, 95.9% of stellar interactions with the binary gain energy from the binary, compared to only 20.9% in the P1b+P1c simulation. Of the low resolution simulations, P1b+P1d had the highest proportion of stellar interactions $v_{\rm in}/w < 1$ (35.2%): this was also the only low resolution simulation which had SMBH coalescence. The number of stars the SMBH is able to interact with (due to orbital eccentricity) remains a dominant factor in SMBH coalescence however, as demonstrated by the failure of P2a+P2a to merge.

Comparing the bottom row of Fig. 5.4, the outgoing stellar velocity displays a reduced spread compared to the incoming stellar velocity, with almost all simulations having a median $v_{\rm out}/w < 0.5$. Incoming stellar particles may in principle have any velocity in the range $0 \leq v \leq \infty$. Conversely, outgoing stellar particles have a velocity that is dictated by the SMBH binary, resulting in a distribution of $v_{\rm out}/w$ that is increasingly right-skewed for increasing mass resolution.

The P+P simulation suite, whilst having a steeper progenitor density profile ($\gamma = 1.6$) than previous work by Rantala et al. (2017) and Rantala et al. (2018), is used as a fiducial set of simulations owing to the equal mass and equal density profiles of the progenitor galaxies. In the following sections, the results of each simulation suite are compared and contrasted to the results of the P+P suite.

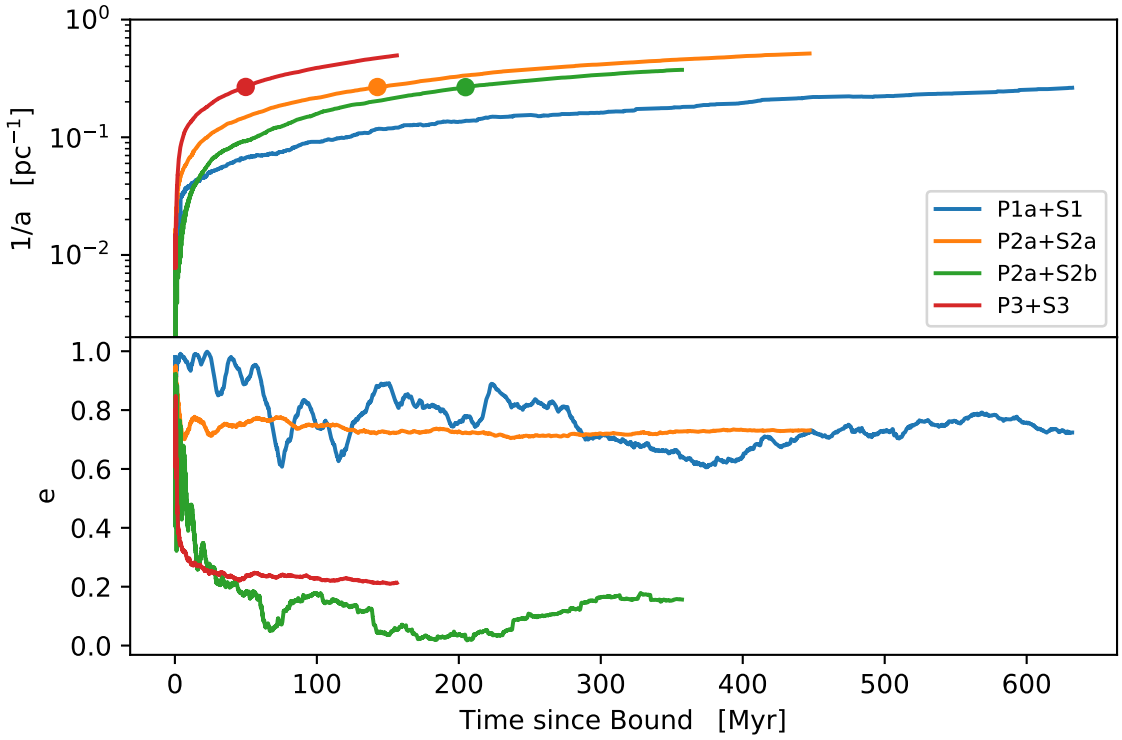

Figure 5.5: Same as Fig. 5.2, showing the inverse semimajor axis and orbital eccentricity of simulations in the P+S suite.

5.3 Unequal Mass, Equal Density Mergers

The unequal mass, equal density merger simulations form the P+S simulation suite. Similar to the P+P simulations, if a SMBH binary was driven to a circularised orbit early in the simulation (i.e. the inverse semimajor axis is still low) and maintained a low eccentricity for an extended duration, the simulation was discontinued.

The orbital parameters of simulations in the P+S suite are shown in Fig. 5.5. The lack of an upturn in the inverse semimajor axis for simulations at all resolutions indicates that none of the SMBH binaries coalesced. The eccentricity evolution of the different simulations is varied, with the P3+S3 and P2a+S2b simulations quickly settling to $e \simeq 0.25$ and $e \simeq 0.2$ respectively. Conversely, the P1a+S1 and P2a+S2a simulations maintain a high eccentricity ($e \simeq 0.7$) for more than 400 Myr following the SMBH binary becoming bound. The high eccentricity and failure to achieve SMBH coalescence indicates that the P1a+S1 and P2a+S2a galaxies have emptied the loss cone of stars that are able to interact with the binary. Similar to the P+P suite, the hardening radius of the P+S suite shows little variation between resolutions, with $a_\mathrm{h} = (3.74 \pm 0.01)\,\mathrm{pc}$. The low resolution simulation (P1a+S1)

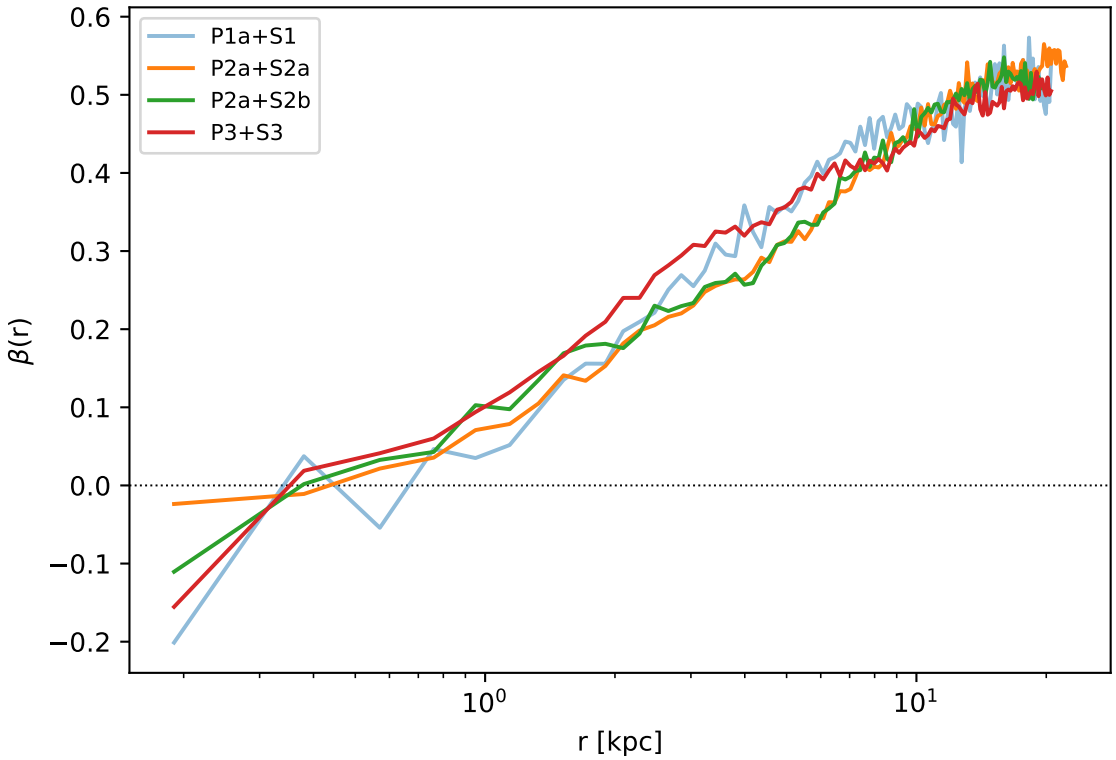

Figure 5.6: Same as Fig. 5.3, showing the $\beta(r)$ profile of galaxies in the P+S suite. All $\beta(r)$ profiles are seen to decrease towards the centre of the merger remnant.

did not form a hard binary, as $a > a_{\rm h}$ at all times.

The $\beta(r)$ profile for each simulation in the P+S suite demonstrates a profile that increases with radius, as shown in Fig. 5.6. All profiles indicate a stellar velocity that is tangentially-biased in the centre, and thus represents a deficit in the number of particles that can undergo three-body interactions with the SMBH binary. Stellar orbits at the kiloparsec-scale are radially-biased, thus indicating the presence of core-scouring by the SMBH binary. Greater stochasticity is present in the low resolution P1a+S1 compared to P3+S3, reflecting a similar result to the P+P suite. The central regions of the simulations in the P+S suite are not so tangentially-biased so as to account for the lack of SMBH coalescence, particularly when compared to the $\beta(r)$ profiles reported in Rantala et al. (2018), hinting at an inability of nearby stars to extract energy from the binary.

The mass flow through a 30 pc shell about the SMBH binaries in the P+S suite is comparable to that for the P+P suite. A general trend of increasing mass resolution displaying a greater stellar mass both outgoing and incoming through the shell is seen, as is the initial peak in mass flow. In the P+S simulations, in particular the P3+S3 simulation, evidence for 'sloshing' of stellar material is seen as

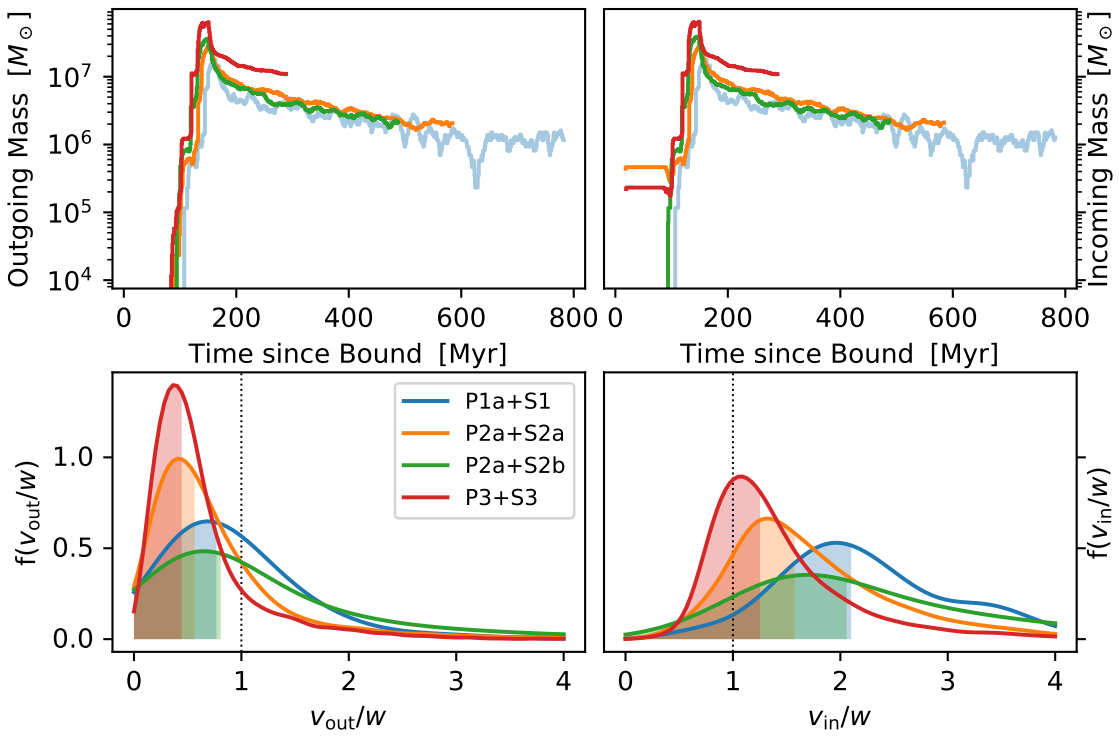

Figure 5.7: Same as Fig. 5.4, showing the velocity of stellar particles crossing a 30 pc shell about the SMBH binary in the P+S suite. Note the scale in the bottom row of the figure.

local peaks in the mass within the Ketju region during the time the SMBH binary becomes bound (see Fig. A.6). The sloshing of stellar particles is understood in terms of the dynamical disturbance caused by the SMBHs ploughing through the dense stellar field. As such, the decrease in stellar mass crossing the shell in Fig. 5.7 is naturally explained as the systems settle to an equilibrium state. Similar to the P+P simulations, the low resolution P1a+S1 simulation demonstrates the greatest stochasticity in the stellar mass flow.

The incoming stellar velocity distribution scaled by the watershed velocity in Fig. 5.7 clearly explains the difficulty in achieving SMBH coalescence in an unequal-mass merger. Each simulation in the P+S suite, including the highest mass resolution P3+S3, has a median v_{in}/w in excess of unity. The P1a+S1 and P2a+S2b simulations have less than 4.06% and 5.70% of the incoming stellar population able to interact with the binary, respectively. In the high mass resolution P3+S3, the proportion of incoming stellar particles that can harden the SMBH binary is a more generous 25.7%, which is still drastically less than the 97.0% in the comparable P3+P3 simulation. From Fig. 5.7, it may be deduced that the majority of stellar particles approach the SMBH binary with a velocity that imparts energy to the

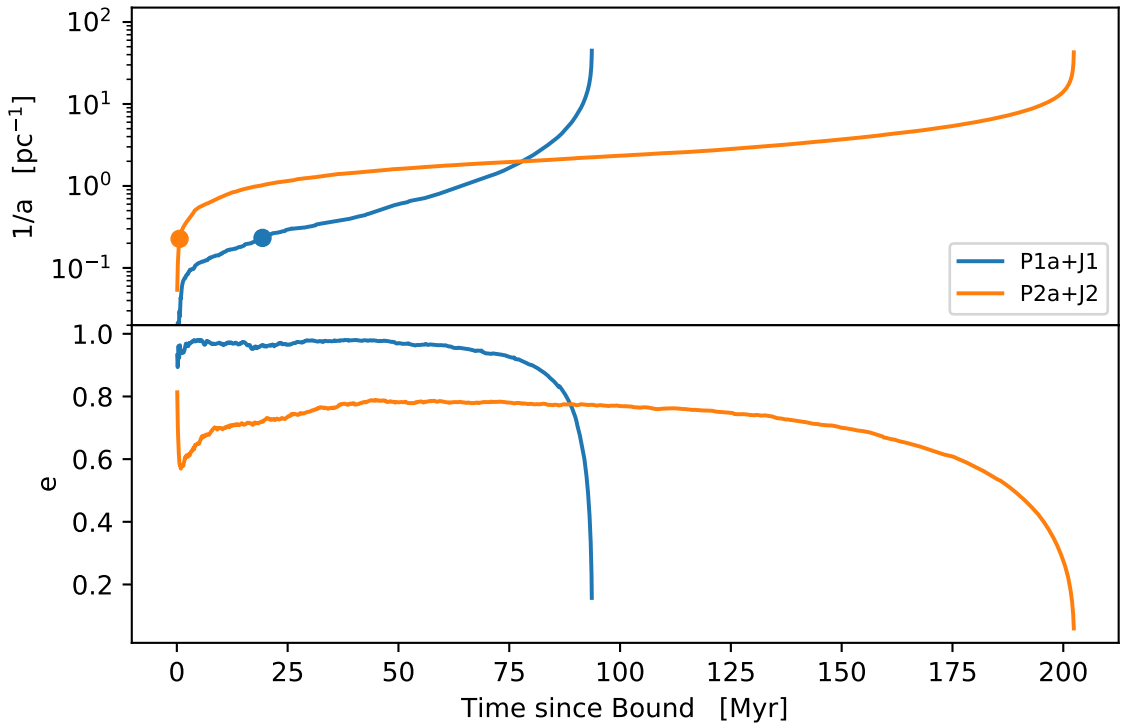

Figure 5.8: Same as Fig. 5.2, showing the inverse semimajor axis and orbital eccentricity of simulations in the P+J suite.

binary, preventing any appreciable decrease in the semimajor axis. As shown in Fig. A.8, the mean approach velocity of stellar particles is greater than $1.5 \times 10^3\,\mathrm{km\,s^{-1}}$ for all medium and low resolution P+S simulations.

The outgoing (scaled) stellar particle velocity distribution demonstrates the increasingly right-skewed distribution with increasing mass resolution as shown by the P+P suite. All simulations have a median $v_{\rm out}/w$ less than unity, indicating the dominance of the SMBH binary in regulating the stellar velocities following an interaction.

5.4 Equal Mass, Unequal Density Mergers

The equal mass, unequal density merger simulations form the P+J simulation suite. Owing to the computational cost of simulating high-γ density profiles, only one simulation per mass resolution was performed. The high resolution (P3+J3) simulation resulted in a direct collision of the SMBH binary: this simulation is excluded from the following analysis, and discussed separately in §5.4.1.

The orbital parameters of the simulations in the P+J suite, presented in Fig.

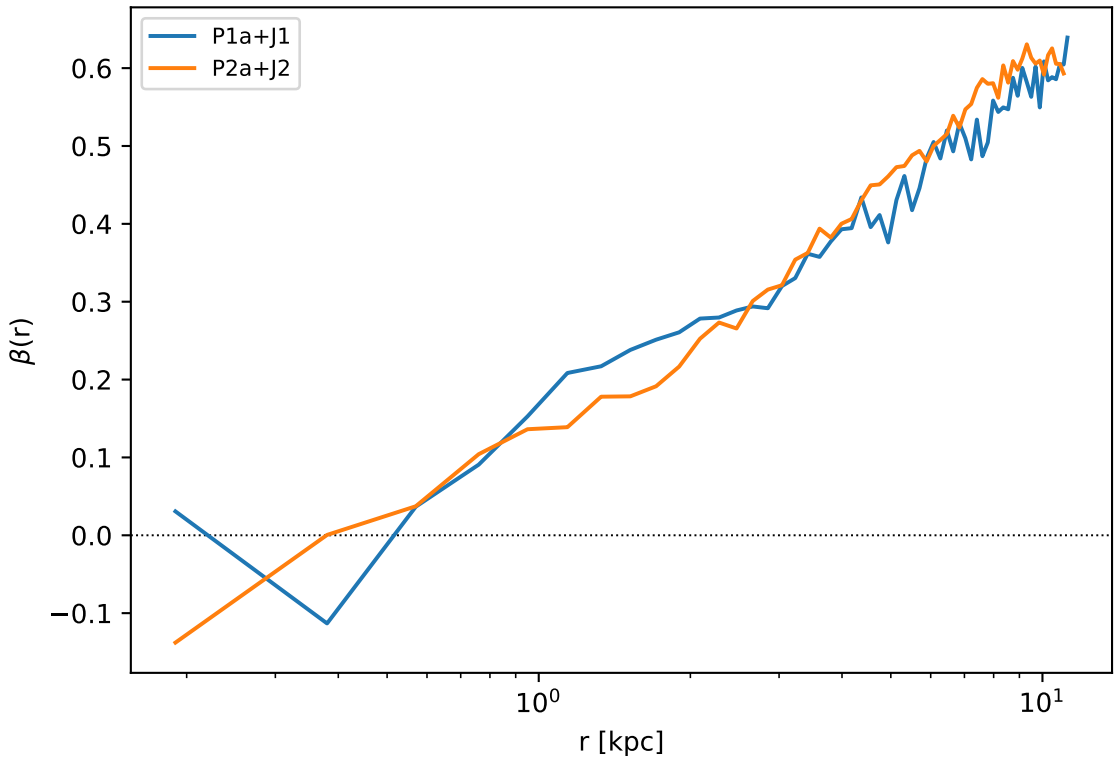

Figure 5.9: Same as Fig. 5.3, showing the $\beta(r)$ profile of galaxies in the P+J suite. All $\beta(r)$ profiles are seen to decrease towards the centre of the merger remnant.

5.8, indicate that all simulations resulted in SMBH coalescence. The time to coalescence is remarkably short: 93.6 Myr for the P1a+J1 system, and 203 Myr for the P2a+J2 system. Comparatively, the shortest time to coalescence in the P+P suite was the P2a+P2b merger, at 200 Myr. The hardening radius of the P+J suite is (4.36 ± 0.06) pc. The orbital eccentricity of the SMBH binaries in the P+J suite is consistently high, in particular P1a+J1 which maintains $e > 0.95$ for the duration of the three-body interaction phase, before the eccentricity decreases as GW emission dominates. The eccentricity of P2a+J2 gently rises to a maximum of $e \sim 0.78$: the lower eccentricity implies that the binary is able to interact with a smaller stellar population than P1a+J1, and thus the time to coalescence is increased.

The $\beta(r)$ profile of the P+J suite, shown in Fig. 5.9, indicates a central stellar population which is only mildly tangentially-biased, and becomes increasingly radially-biased at larger radii. Unlike the P+P suite which has a stellar population with little bias ($\beta(r) \simeq \pm 0.05$) for the inner 1.0 kpc, the P+J suite displays a stellar population that tends immediately to radial-bias, not dissimilar to the P+S suite. In particular the low resolution P+P simulations tend to radially-biased stellar orbits only after 3.0 kpc (see Fig. 5.3): the P1a+J1 simulation has $\beta(r = 3.0\,\mathrm{kpc}) \gtrsim 0.30$.

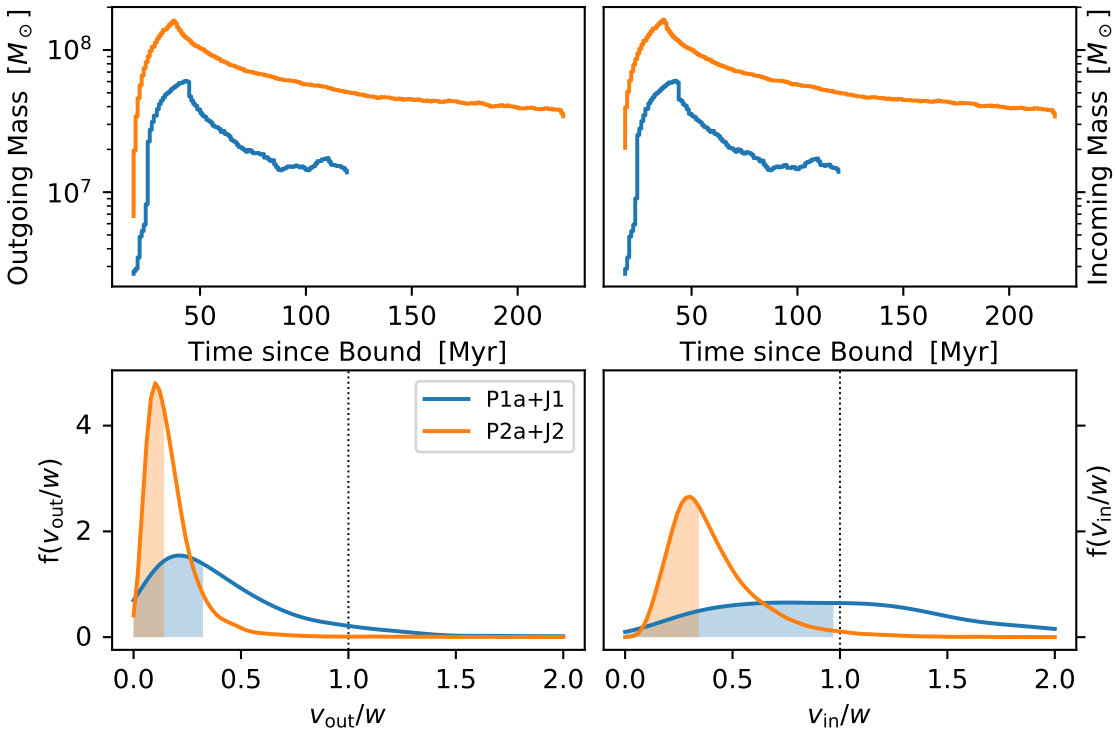

Figure 5.10: Same as Fig. 5.4, showing the velocity of stellar particles crossing a 30 pc shell about the SMBH binary in the P+J suite. Note the scale in the bottom row of the figure.

The large population of stellar orbits which are radially-biased allows for the SMBH binary to experience more three-body interactions relative to the P+P suite, with the majority of stellar interactions extracting orbital energy and angular momentum from the binary. Similar to P3+P3, P2a+J2 displays a KDC that may explain the initial increase in orbital eccentricity of the SMBH binary.

The stellar mass flow through a 30 pc shell about the SMBH binary centre of mass (top row of Fig. 5.10) indicates the flow of mass is correlated with the mass resolution, as in the P+P suite. Stellar mass first enters the shell, before a near-equal amount of mass exits the shell in the following time interval. The P2a+J2 simulation has the highest peak in stellar mass flow of all systems in the study, at $1.6 \times 10^8\,\mathrm{M}_\odot$ occurring 38 Myr after the binary becomes bound. The quantity of stellar mass passing through the shell steadily decreases with time following the peak, however remains consistently higher than the equivalent resolution simulations from the P+P suite, some $5.0 \times 10^6\,\mathrm{M}_\odot$ and $3.0 \times 10^7\,\mathrm{M}_\odot$ for the low and medium resolutions respectively.

The bottom row of Fig. 5.10 clearly shows that the majority of stellar interactions with the SMBH binary are able to extract energy from the binary. In all

simulations, the incoming velocity of stars have a median velocity (scaled to the watershed velocity) less than unity. In the case of P2a+J2, the median $v_{\rm in}/w$ is 0.362, with 97.8% of all stellar interactions able to extract energy from the SMBH binary. The P2a+J2 simulation has the greatest number of such interactions of any simulation in the study (P3+P3 had a comparable value of 97.0%). The outgoing velocity distribution of P2a+J2 is exceptionally peaked (median value 0.143), and the low resolution P1a+J1 has an outgoing velocity distribution very similar to the P1b+P1d simulation with a median outgoing scaled velocity of 0.324. From the outgoing velocity distributions, the SMBH binary is seen to strictly regulate the outgoing velocity of the stellar particles to a velocity which is some fraction of the SMBH binary orbital velocity. The magnitude of the unscaled outgoing velocity (Fig. A.9) closely mimics that of the P+P suite, with the majority of outgoing stellar particles exiting the shell with a velocity less than $1.0 \times 10^3\,\mathrm{km\,s^{-1}}$.

5.4.1 P3+J3: A Direct Collision

The high resolution realisation of the P+J simulation demonstrates exceptionally rapid SMBH coalescence that may be interpreted as a direct collision of the SMBH binary. The SMBHs in the system make five pericentre passages prior to the system becoming bound, after which coalescence occurs within 0.22 Myr. The SMBH coalescence timescale is below the nominal temporal resolution of the simulation (10 kyr), and thus to investigate the coalescence the SMBH binary system is integrated from the final simulation output with data captured 200 times per orbit. The SMBH inspiral commences at an eccentricity $e = 0.99986$. The coalescence time scale is significantly longer for the high-temporal resolution integration compared to the nominal integration, spanning 0.3 Myr (Fig. 5.11, bottom panel), owing to stellar particles being neglected from the high-temporal resolution integration. The binary motion in the centre of mass frame is presented in Fig. 5.11. Immediately apparent is the orbital precession of the binary, which pivots about the binary centre of mass for the duration of the simulation. The inverse semimajor axis has a value of $1/a = 1.0\,\mathrm{pc^{-1}}$ at 0.288 Myr after the high-temporal resolution integration commences: from this time the binary eccentricity is rapidly circularised and merger occurs within 0.054 Myr. The orbit-averaged emitted energy increases asymptotically from $4.17 \times 10^{-1}\,\mathrm{M_\odot\,kpc^2\,yr^{-2}}$ at the start of the high-temporal integration to $2.05 \times 10^4\,\mathrm{M_\odot\,kpc^2\,yr^{-2}}$ just prior to merger, which is comparable to the orbit-averaged emitted energy of less dramatic mergers (e.g. the P3+P3 system). Consequently, it may be concluded that even in the case of extreme orbital eccentricities

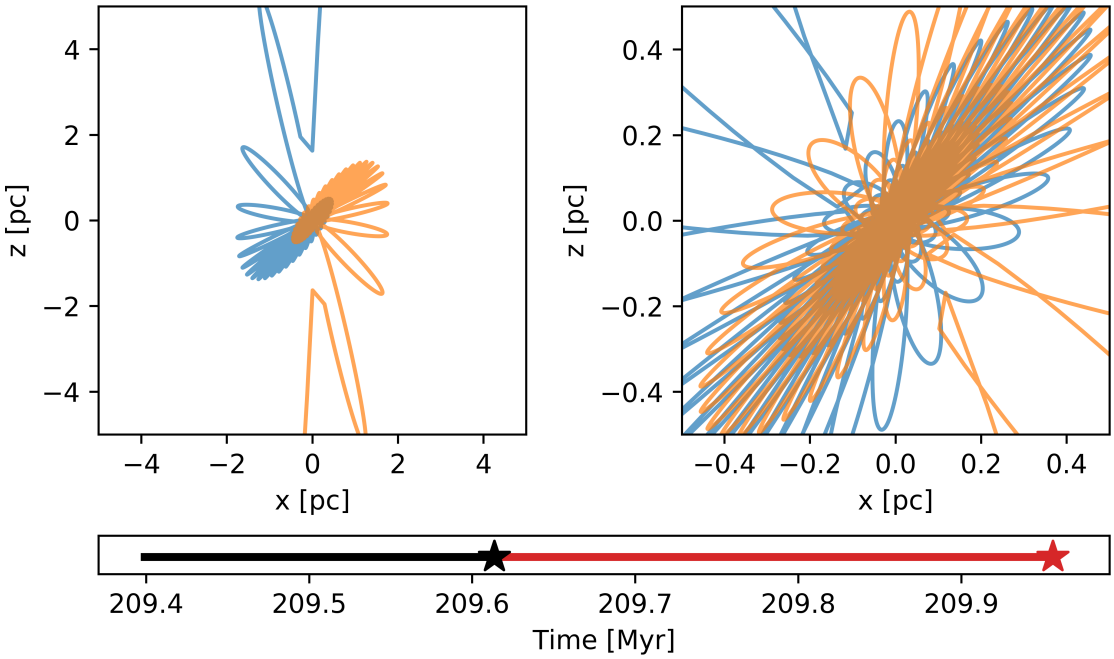

Figure 5.11: High temporal resolution integration of the P3+J3 system, occuring from 209.66 Myr to 209.96 Myr. *Top left:* Orbit of the SMBH binary (in the centre of mass frame) taken from the high temporal resolution integration. *Top right:* Again the SMBH binary orbit, however zoomed in to the central region. Note the orbital precession. *Bottom:* Time span of the bound binary. The black line segment shows from when the binary was bound to when the binary merged (indicated by a star) in the original simulation. The red line segment indicates the duration of the high-temporal resolution integration, starting from just prior to the binary merging in the original simulation.

the SMBH binary is able to emit sufficient energy to circularise the binary orbit.

The orbital evolution of a direct-collision binary is expected to be less-ordered if the spin of each SMBH is accounted for. As an example, SMBH spins misaligned with each other and to the orbital angular momentum, coupled with strong orbital precession (such as the precession demonstrated by the P3+J3 system), may cause significant 'kicks' to the SMBH velocities (Herrmann et al., 2007). These kicks, in extreme cases where the kick velocity is $v_{\rm kick} > 10^3\,{\rm km\,s^{-1}}$, may eject the merged SMBH from the galaxy (e.g. Poisson & Will, 2014).

5.5 Unequal Mass, Unequal Density Mergers

The unequal mass, unequal density merger simulations form the J+S simulation suite. Owing to the computational cost (as was the case for the P+J suite), only one simulation per mass resolution was performed. The high resolution realisation (J3+S3) exceeded the computational time before forming a bound binary; it is

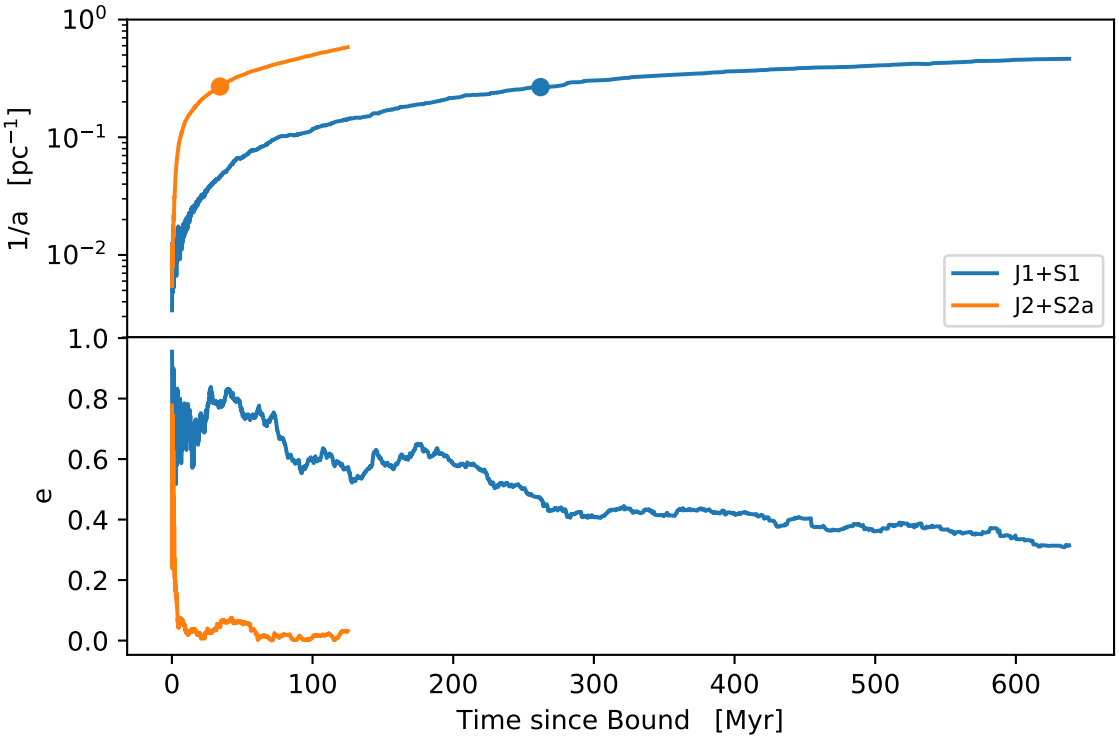

Figure 5.12: Same as Fig. 5.2, showing the inverse semimajor axis and orbital eccentricity of simulations in the J+S suite.

excluded from the analysis.

From the SMBH orbital parameters shown in Fig. 5.12, no simulation in the J+S suite resulted in SMBH coalescence. The hardening radius was found to be $a_\mathrm{h} = (3.73 \pm 0.02)\,\mathrm{pc}$, almost identical to the value found for the P+S suite. No simulation was able to achieve a sub-parsec semimajor axis, with J1+S1 stalling at 2.16 pc and J2+S2a stalling at 1.72 pc. The eccentricities of the SMBH orbit in the J+S suite are driven to low values following the binary becoming bound, as seen in particular for J2+S2a. The eccentricity for J2+S2a falls to $e = 0.06$ a mere 4 Myr after becoming bound; the low resolution J1+S1 eccentricity decreases gently to 0.32 after the binary has been bound for 638 Myr. The simulations were stopped in both cases, as the low eccentricities prevent the binaries from being able to interact with stellar particles that remove orbital energy from the system.

Similar to the P+S suite, the J+S suite has a $\beta(r)$ that indicates a tangentially-biased central stellar population, with the inner 0.19 kpc displaying a value between -0.1 and -0.2 (see Fig. 5.13). The stellar population rapidly becomes radially-biased at larger radii, with all J+S simulations having $\beta(r) = 0.4$ at 7.0 kpc, again similar to the P+S suite. Collating the $\beta(r)$ profiles of both P+S and J+S suites, the

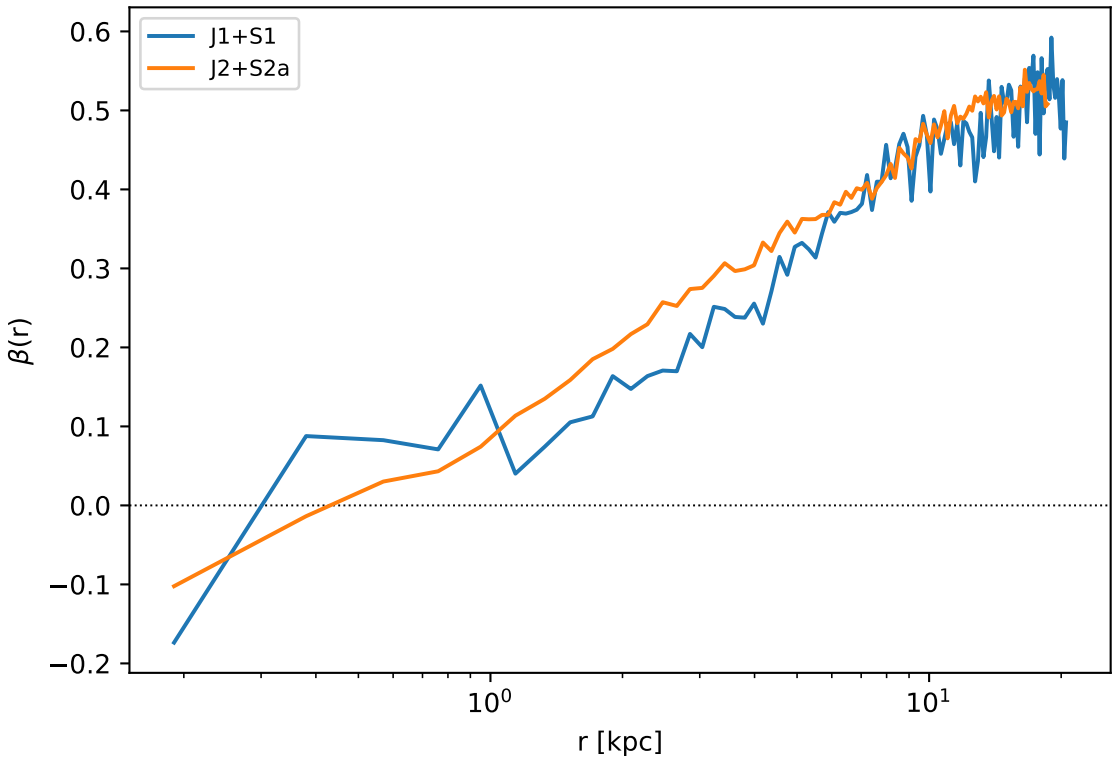

Figure 5.13: Same as Fig. 5.3, showing the $\beta(r)$ profile of galaxies in the J+S suite. All $\beta(r)$ profiles are seen to increase with radius.

results suggest that unequal mass mergers form a merger remnant with an increased tendency to central regions with more pronounced tangentially-biased stellar populations than equal mass mergers. No simulation in either the P+S or J+S suites demonstrate a central velocity anisotropy as tangentially-biased as those found in the lower-density progenitors of Rantala et al. (2018).

The stellar mass flowing through a 30 pc shell in the J+S suite (Fig. 5.14) peaks at a comparable time to the P+S suite, however with a peak value that is more similar to the P+P suite. The J1+S1 simulation peaks at $1.8 \times 10^7\,\mathrm{M}_\odot$, whereas the J2+S2a simulation peaks at $7.0 \times 10^7\,\mathrm{M}_\odot$. As with the other simulation suites, stellar mass in the J+S suite first enters the shell before a comparable mass exits the shell during the next time interval. The stellar mass flow through the shell approaches a value comparable to the P+S suite after the peak.

Similar to the P+S suite, the velocity distribution of the J+S suite scaled to the watershed velocity w shows that the majority of stellar interactions with the SMBH binary are unable to remove orbital energy from the binary. The median incoming scaled velocity v_{in}/w is 1.97 for J1+S1 and 1.28 for J2+S2a: both in excess of unity. Consequently, the majority of stellar particles entering through the shell

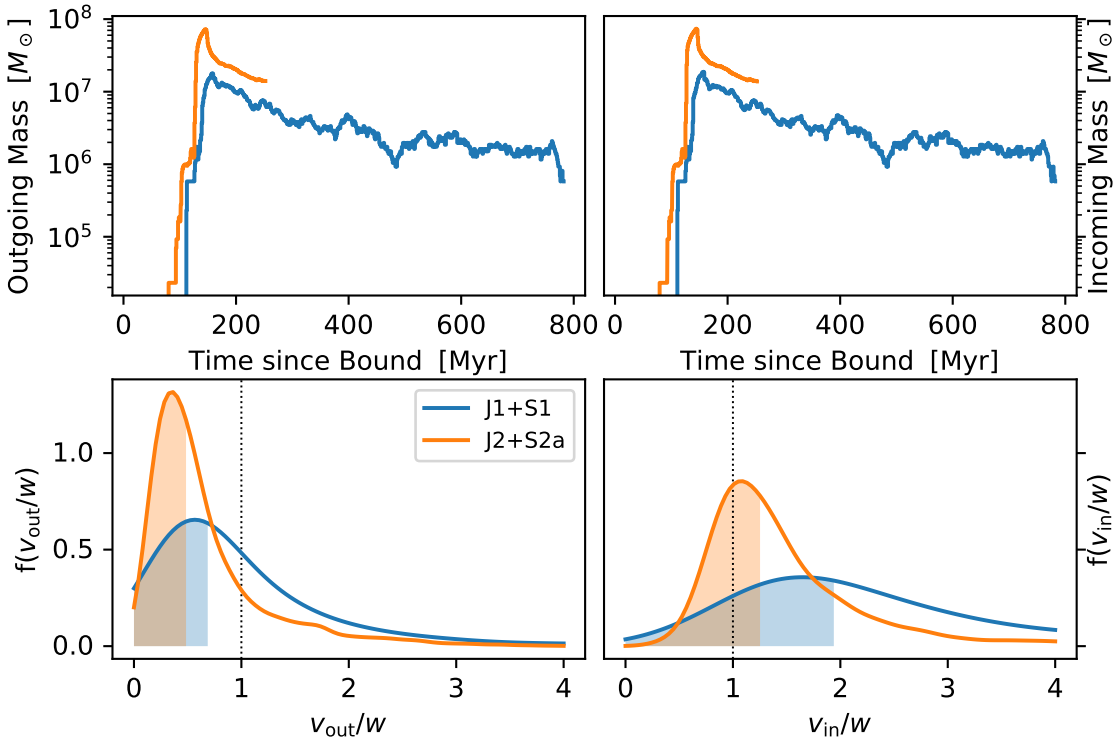

Figure 5.14: Same as Fig. 5.4, showing the velocity of stellar particles crossing a 30 pc shell about the SMBH binary in the J+S suite. Note the scale in the bottom row of the figure.

impart energy to the SMBH binary, preventing the binary from efficiently hardening. Consistent with the other simulation suites, the SMBH binary regulates the outgoing stellar velocity distribution such that 66.9% of exiting stars in J1+S1 and 82.7% of exiting stars in J2+S2a have a velocity less than the watershed velocity. The typical resolution dependence is also present in the exiting stellar velocity distribution of Fig. 5.14: a higher mass resolution results in a stellar velocity distribution that is more right-skewed than that of lower mass resolution. The unscaled velocity distribution of the J+S suite (Fig. A.10) follows closely that of the P+S suite, with the majority of particles exiting with a velocity $v_{\rm out} \lesssim 1.5 \times 10^3\,{\rm km\,s^{-1}}$.

5.6 Resolution Effects

The evolution of the inverse semimajor axis (the hardening rate) is investigated to determine if there exists a resolution-dependence of the hardening rate. The points comprising the inverse semimajor axis curve are divided into 800 segments, to which a linear regression line is fit to each segment. To belong to the hardening phase, a line segment must satisfy the conditions:

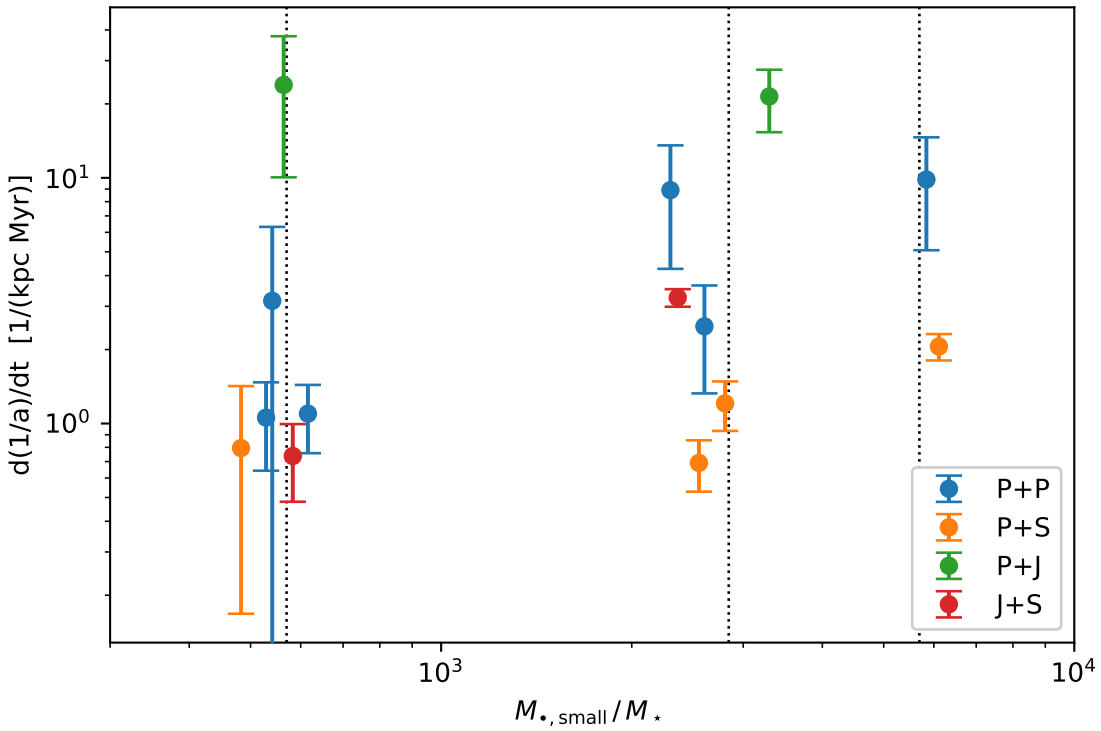

Figure 5.15: Hardening rate $\mathrm{d}(1/a)/\mathrm{d}t$ taken at a time $t > t_{a_\mathrm{h}}$ and averaged over line segments that satisfy the criteria described in the text, for all simulations in the study. Error bars indicate 1σ uncertainty. The hardening rate is plotted as a function of the mass resolution relative to the less massive of the two SMBHs, plus a small offset for visual clarity. The dotted lines correspond to the true mass resolution.

1. An R^2 value from the linear regression fit in excess of 90%, as the evolution of $1/a$ has been shown to be linear in the hardening phase (e.g. Mikkola & Valtonen, 1992; Quinlan, 1996; Merritt, 2006),

2. The segment must describe a time after $a = a_\mathrm{h}$, and

3. The magnitude of the time-averaged change in a due to GW emission, $\langle \mathrm{d}a/\mathrm{d}t \rangle$ (Eq. (2.60)), must be below a given threshold, here taken to be $10^{-14}\,\mathrm{kpc\,Myr^{-1}}$.

A figure demonstrating the regions selected for an example system is presented in Fig. A.11. The hardening rate is then determined as the mean of all line segments that satisfied the above criteria, and is shown in Fig. 5.15. Whilst scatter is present in the calculated hardening rates, there is no resolution dependence of the hardening rate for the simulations in any suite. Typically, P+S hardening rates are the lowest at $\mathrm{d}(1/a)/\mathrm{d}t = 1.19\,\mathrm{kpc^{-1}\,Myr^{-1}}$, and P+J hardening rates the highest at $\mathrm{d}(1/a)/\mathrm{d}t = 22.6\,\mathrm{kpc^{-1}\,Myr^{-1}}$. The presented P+J hardening rates are higher than those found

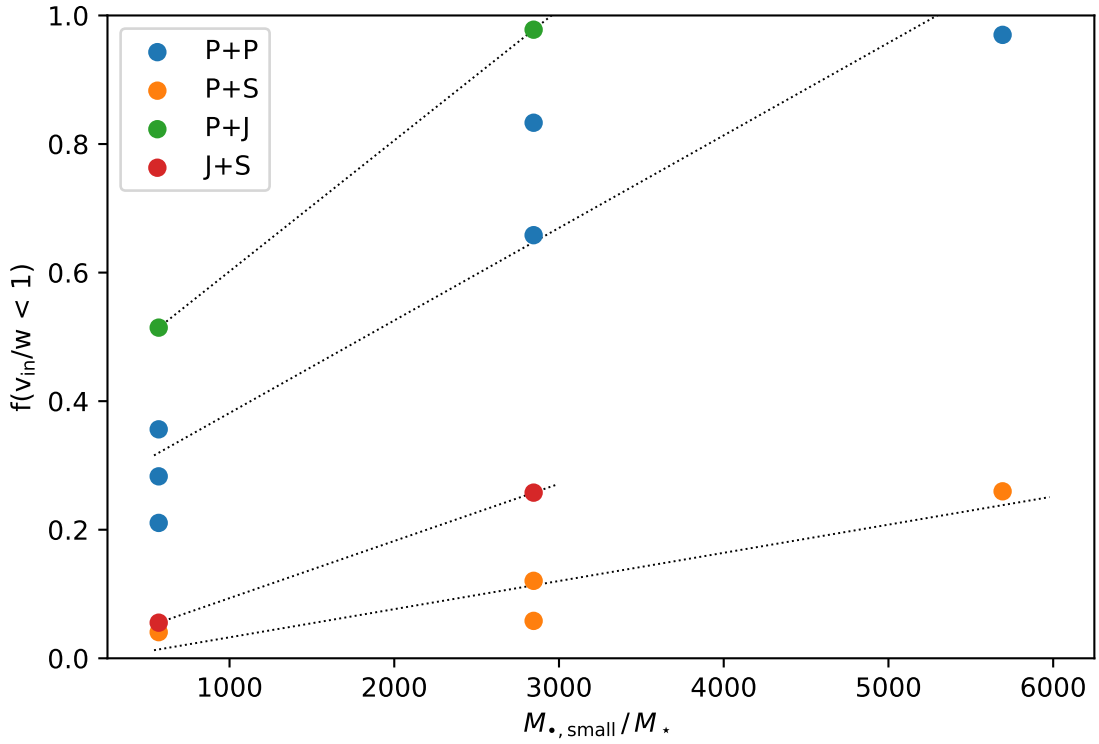

Figure 5.16: Percentile within which the scaled incoming stellar velocity $v_{\rm in}/w$ is less than unity as a function of mass resolution. The mass resolution is taken to be the ratio of the smaller SMBH mass $M_{\bullet,\rm small}$ to the stellar particle mass $m_\star$. Unequal mass mergers typically result in a lower proportion of stellar particles able to interact with the binary ($v_{\rm in}/w < 1$ than equal mass mergers). Additionally, steeper density progenitor density profiles typically allow for more stellar particles to interact with the SMBH binary than those progenitor galaxies with lower density profiles.

in Rantala et al. (2017) but lower than those of Khan et al. (2012) using $\gamma = 1.75$ progenitors. The P+S and J+S suites have a hardening rate that is less than those presented in Rantala et al. (2017). The P+P suite is in agreement with the findings of Rantala et al. (2017) within the 1σ error bounds. The overall trend of no resolution-dependence of the hardening rate in galactic merger simulations is consistent with the literature (e.g. Khan et al., 2011, 2012; Vasiliev et al., 2015; Rantala et al., 2017).

In addition to the effect of mass resolution on the hardening rate, the effect of mass resolution on the orbital velocity of stellar particles is explored. It was found that by increasing the mass resolution, the number of stellar particles crossing a 30 pc shell with a velocity less than or equal to the watershed velocity increased. Fig. 5.16 shows the quantile within which $v_{\rm in}/w < 1$ as a function of mass resolution for all simulations, denoted $f(v_{\rm in}/w < 1)$. The trend between increasing mass resolution and increasing $f(v_{\rm in}/w < 1)$ is seen clearly, however extrapolation beyond the plotted simulations is not possible owing to the unknown nature of $f(v_{\rm in}/w < 1)$

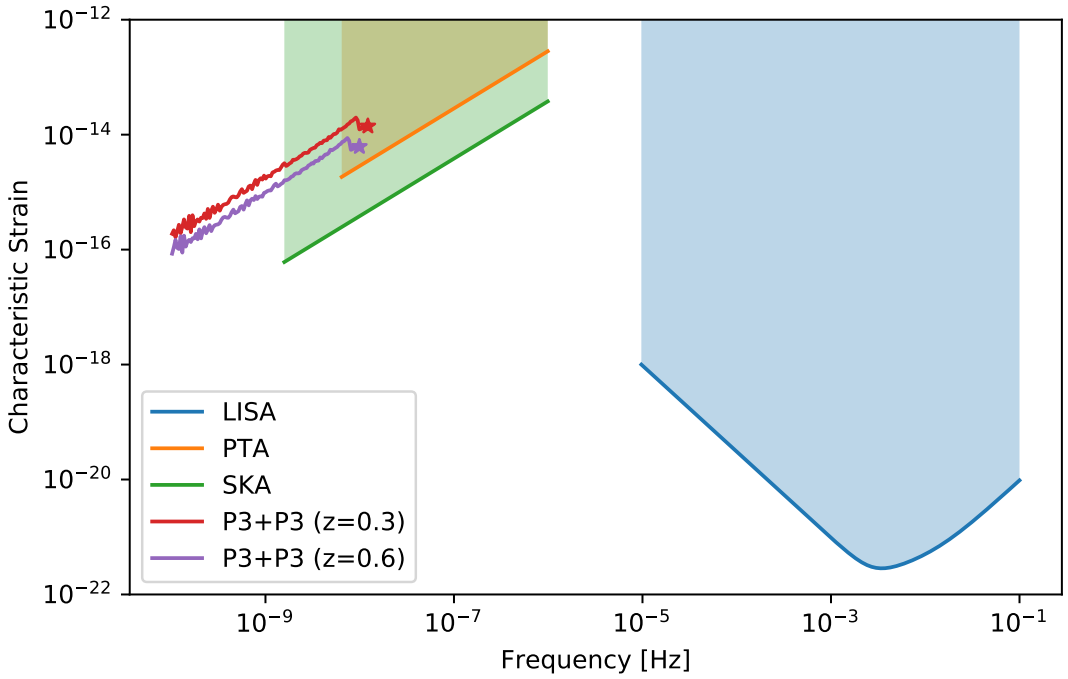

Figure 5.17: GW signal from the P3+P3 merger compared to the proposed LISA, PTA, and SKA sensitivities. The SMBH binary is evolved until twice the innermost stable circular orbit ($R_{\rm ISCO}$) before being discontinued (shown as the star) due to increased inaccuracy in the PN approximations below this radius. A full general relativistic treatment of the binary merger would be required to evolve the GW signal to times occurring after a separation $r = 2R_{\rm ISCO}$. The merger GW signal is consistent with the proposed detection sensitivities of PTAs and the SKA.

at both low and high mass resolutions. A number of low (sub-250 $M_{\bullet,\rm small}/m_\star$) simulations were run in an effort to examine the behaviour of $f(v_{\rm in}/w < 1)$ at low mass resolutions. However, the stochasticity was too great for any discernible trend to be observed. The computational cost prevented very high ($M_{\bullet,\rm small}/m_\star > 6\times10^3$) simulations from being performed.

5.7 Gravitational Wave Signal

The gravitational wave signal was determined for a single merger system, taken to be the P3+P3 system, to ascertain the likelihood of a SMBH binary merger being detected by current and upcoming observation missions. The P3+P3 merger was artificially placed at two redshifts, $z = 0.3$ and $z = 0.6$, corresponding to a luminosity distance of 1.6×10^3 Mpc and 3.7×10^3 Mpc respectively, assuming a Planck Collaboration et al. (2018) cosmology. There is negligible redshift-dependence in

the simulation owing to the stellar particle properties (e.g. metallicity) not evolving throughout the simulation, and no stars are formed due to the lack of gas in the simulation. The P3+P3 SMBH-only system was integrated for 6 kyr prior to the SMBH merger criterion ($r < 2R_{\mathrm{ISCO}}$, §3.4.6). The GW signal for both redshifts is shown in Fig. 5.17. Prior to the merger criterion from being satisfied, the $z = 0.3$ realisation has a characteristic strain of $h_c = 1.41 \times 10^{-14}$ at 1.22×10^{-8} Hz, and the $z = 0.6$ realisation has a characteristic strain of $h_c = 6.20 \times 10^{-15}$ at 9.92×10^{-9} Hz. As expected, increasing the redshift of the merger event decreases the characteristic strain measured. The simulation is not continued for binary separations below $2R_{\mathrm{ISCO}}$ owing to the increasing inaccuracy of the PN corrections at such small separations (e.g. Poisson & Will, 2014). The PTA sensitivity in Fig. 5.17 is determined following Sesana et al. (2008), and assumes 20 pulsars are observed for five years with 100 ns RMS error in the timing residual. Similarly, the SKA sensitivity is determined following Moore et al. (2015), and assumes 50 pulsars are observed for 20 years with 30 ns RMS error in the timing residual. The LISA sensitivity is computed assuming the merger-event duration is larger than the observation window of LISA (Robson et al., 2019).

The P3+P3 signal, at both arbitrary redshifts $z = 0.3$ and $z = 0.6$, is seen to be a prime candidate for the Square Kilometre Array (SKA) for the majority of the inspiral, and a candidate for pulsar timing arrays (PTAs) with present-day constraints on the sensitivity and pulsar count (refer to §2.2.7). As previously discussed, the upcoming LISA mission will not be sensitive to the GW emission from the coalescence of $M_\bullet \gtrsim 10^8\,\mathrm{M}_\odot$ SMBH binaries, with systems such as P3+P3 emitting GW radiation at frequencies some three orders of magnitude below the frequency range of LISA.

5.8 Integral-Field Unit Spectroscopy

Finally, mock integral-field unit spectroscopy maps were created for the highest resolution realisation of each simulation suite to compare the large scale stellar kinematics of the merger remnant to observed galaxies. Each galaxy is aligned with the stellar angular momentum within one half-mass radius of the galaxy centred on the stellar centre of mass. The stellar particles are then binned using the Voronoi binning technique (Cappellari & Copin, 2003; Frigo et al., 2019) to achieve a minimum of 2000 particles per bin. From the Voronoi maps, the LOS kinematics are determined.

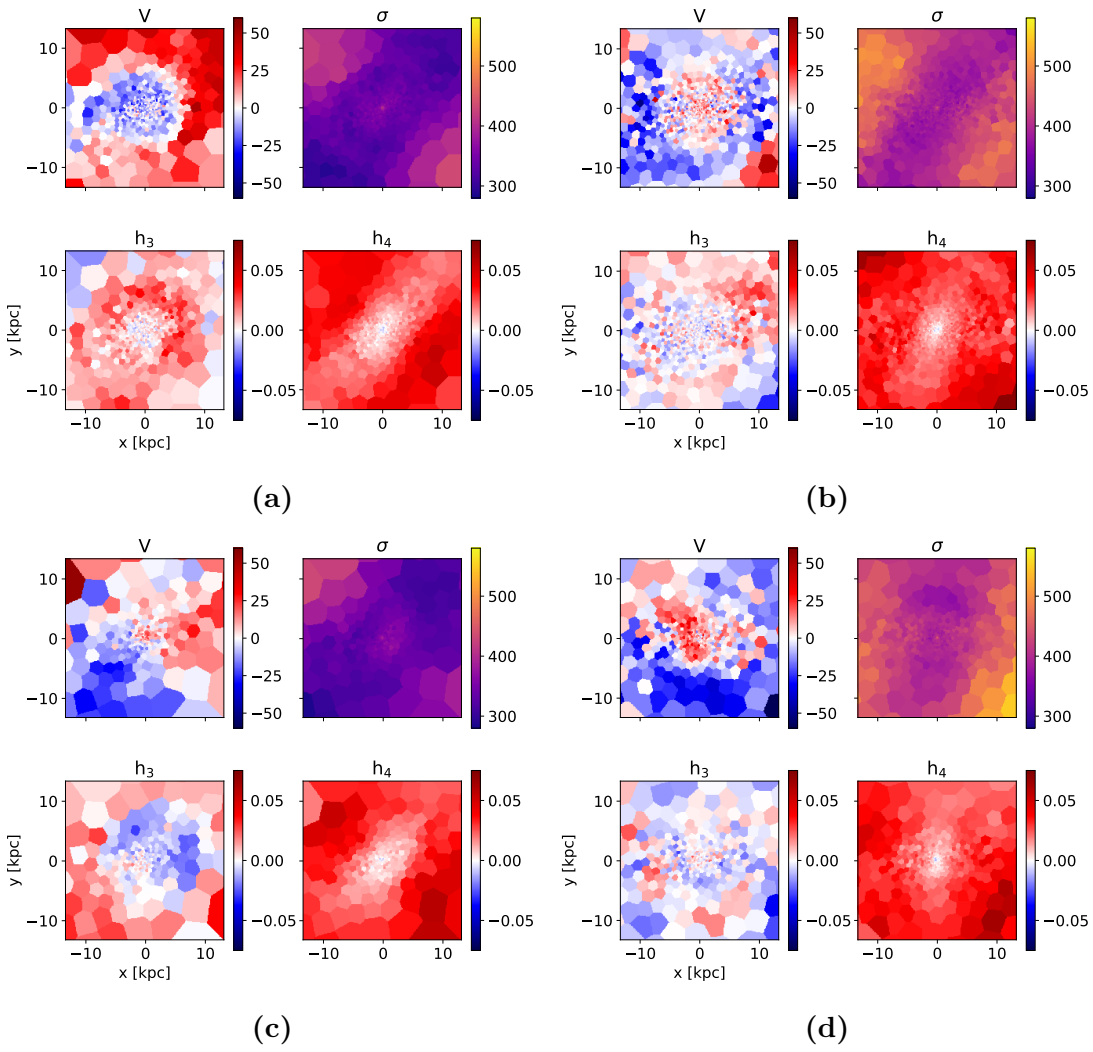

Figure 5.18: Voronoi maps of the highest resolution merger remnant from each suite. **(a):** The P+P remnant at $t = 591\,\mathrm{Myr}$. **(b):** The P+S remnant at $t = 498\,\mathrm{Myr}$. **(c):** The P+J remnant at $t = 481\,\mathrm{Myr}$. **(d):** The J+S remnant at $t = 458\,\mathrm{Myr}$. Each subfigure displays (left to right, top to bottom): the mean LOS velocity V ($\mathrm{km\,s^{-1}}$), the velocity dispersion σ($\mathrm{km\,s^{-1}}$), and the h_3 and h_4 Gauss-Hermite moments.

5.8.1 Line-of-Sight Kinematics

As shown in Fig. 5.18, the LOS mean velocity clearly depicts the merger remnant of each suite to be a slow-rotating galaxy, with rotation peaking at $V \sim \pm 50\,\mathrm{km\,s^{-1}}$. The mean velocity magnitude increases with radius in all simulation suites. Clear rotation is seen in the case of the P+J merger (63 Myr after SMBH coalescence), though the apparent misalignment of the rotation is due to stellar particles beyond the half-mass radius not being included in the alignment of the angular momentum vector. A centrally-rotating region is hinted at in the case of the J+S remnant; the

rotating structure does not appear to extend beyond the nominal 10 kpc radius. In the case of the P+P and P+S remnants, no ordered rotation is visible.

Unequal-mass galactic mergers (P+S and J+S) demonstrate the greatest velocity dispersions, in support of the $M_\bullet$–$\sigma_\star$ relation (e.g. Ferrarese & Merritt, 2000; Gebhardt et al., 2000). The mean velocity dispersions in P+S and J+S are measured as $424\,\mathrm{km\,s^{-1}}$ and $449\,\mathrm{km\,s^{-1}}$, respectively. The central region of each merger remnant displays a peak in velocity dispersion, with a value in excess of $430\,\mathrm{km\,s^{-1}}$ in all suites except the P+J suite, which peaks at a more modest $401\,\mathrm{km\,s^{-1}}$. The P+P and P+S merger remnants in Figs. 5.18a and 5.18b display evidence of a double-peaked velocity dispersion structure, with a pair of symmetric, off-centre, significant rises in the velocity dispersion (e.g. Alabi et al., 2015). Such galaxies, termed 2-sigma galaxies, possess a pair of counter-rotating structures within the central galactic regions (Krajnović et al., 2011; Foster et al., 2013). The mean velocity fields of the P+P and P+S merger remnants do not support the hypothesis of these galaxies being 2-sigma galaxies; the curious velocity dispersion pattern is most likely a result of the merger remnant not being relaxed. Additionally, without defined rotation, a symmetry axis is not easily distinguished from the kinematic maps.

As discussed in §2.1.3, the h_3 and h_4 Gauss-Hermite moments give a measure of the asymmetric and symmetric deviation of the fitted profile from the best-fit Gaussian profile, respectively. The magnitude of the deviation in each merger remnant is seen to not exceed 0.055 for both h_3 and h_4. The P+S and J+S merger remnants do not display any systematic asymmetric deviation, as evidenced by the relatively even distribution of positive and negative values of h_3. Conversely, the P+P and P+J merger remnants display a positive bias and negative bias, respectively, in the asymmetric deviation. In particular, the P+J merger remnant has a h_3 deviation that is approximately anti-correlated with the mean LOS velocity V, in agreement with the galaxy being either a fast-rotator (see §5.8.2) or containing a counter-rotating core (Krajnović et al., 2011). Though P2a+J2 displayed a KDC shortly after the SMBH binary became bound, the KDC is not apparent in Fig. 5.18c. The h_3 values of each merger remnant in Fig. 5.18 is in agreement with the mode of the h_3 value distribution of ATLAS^{3D} galaxies, as presented in Krajnović et al. (2011).

As discussed in e.g. Gerhard (1993) and Gerhard et al. (1998), there exists a tight correlation between the measure of symmetric deviation h_4 and the velocity anisotropy profile $\beta(r)$. A radially-biased stellar population exhibits a positive value

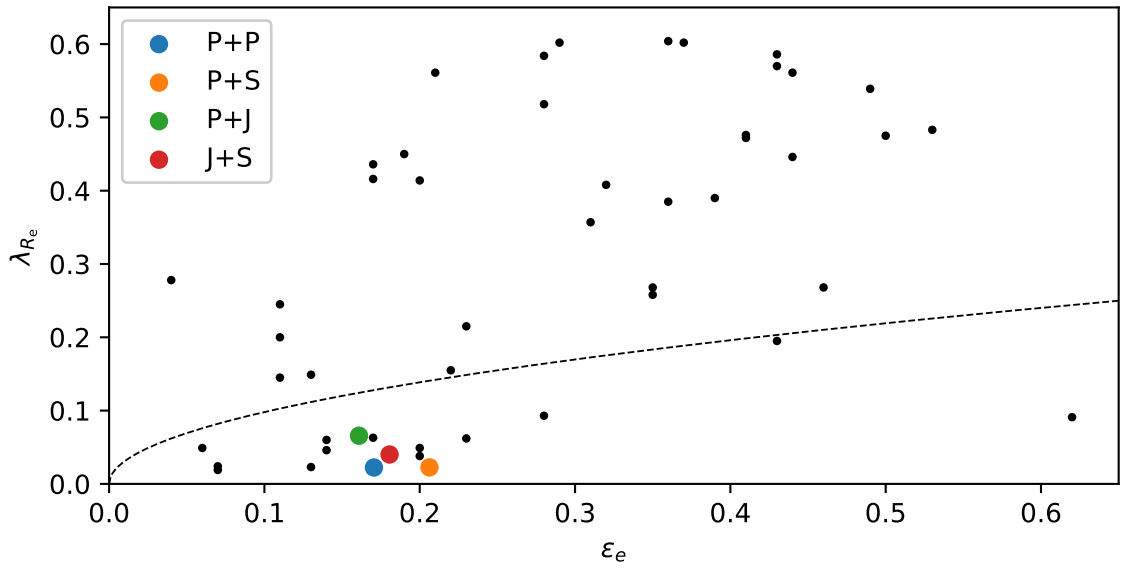

Figure 5.19: Spin-ellipticity plot for the merger remnants in Fig. 5.18, compared to ETGs in the ATLAS^{3D} survey (Emsellem et al., 2011). The dotted line corresponds to the division between slow- and fast-rotators as in Eq. (5.3). The merger remnant of each simulation suite is seen to be a slow-rotator.

for $\beta(r)$ and a similarly positive h_4 value; the converse is also true. Referring to §5.2-§5.5, the $\beta(r)$ profiles of each suite were found to possess central regions with a tangentially-biased stellar population, which became increasingly radially-biased at larger radii. The same trend is seen in the plots of h_4 for each merger remnant. Central regions display a h_4 value that is either 0 or slightly negative (~ -0.01), indicating the central regions of the merger remnants display a tangentially-biased stellar population. Similarly, the outer regions have h_4 in excess of 0.04, indicating a radially-biased stellar population. As with the h_3 distribution, the measured h_4 values of the merger remnants in Fig. 5.18 is in agreement with galaxies in the ATLAS^{3D} survey.

5.8.2 The λ_R Parameter

From the mock IFU maps of Fig. 5.18, the spin parameter λ_R may be determined as in Eq. (2.20). By plotting λ_R at $1\,R_e$ against the ellipticity at $1\,R_e$, the merger remnants may be classified as either slow- or fast-rotating, as in Emsellem et al. (2011). The division between slow- and fast-rotators is determined by the relation:

$$\lambda_R(r = R_e) = 0.31\sqrt{\epsilon(r = R_e)}, \tag{5.3}$$

with galaxies lying above the relation being termed fast-rotators, and those below the relation as slow-rotators. The spin-ellipticity diagram with those merger remnants in Fig. 5.18 is shown in Fig. 5.19. All merger remnants lie below the relation of Eq. (5.3), and are thus determined to be slow-rotators. The result is unsurprising, given the low LOS velocity found for each remnant. The λ_R and ϵ values found for the merger remnants are also in agreement with ETG merger simulations by Bois et al. (2011). Additionally, the merger remnants lie within the neighbourhood of the majority of slow rotators presented in Emsellem et al. (2011) as part of the ATLAS^{3D} survey, supporting the hypothesis that a primary formation pathway for slow-rotating elliptical galaxies is through major merger events (Naab et al., 2006; Bois et al., 2011).

6. Conclusions

In this work, the ability of a SMBH binary in a collisionless, galactic merger environment to coalesce has been investigated to better understand the Final Parsec Problem in massive early-type galaxies. The simulated galaxies were constructed with motivation from observations to constrain the total stellar mass and the steepness of the initial density profile, and scaling relations explored to ensure the SMBH mass, DM halo mass, half-mass radius, and line-of-sight velocity dispersions were consistent with observations. Four simulation suites were constructed, with systems belonging to one of three mass resolutions, thus totalling seventeen simulations that were studied. The ability for a SMBH binary to coalesce was assessed by investigating the evolution of the binary semimajor axis and eccentricity, the velocity anisotropy parameter $\beta(r)$, and the velocity distribution of stars within the vicinity of the SMBH binary.

In general, low mass resolution simulations displayed greater stochasticity in the evolution of the orbital parameters compared to medium and high mass resolution simulations. Orbital eccentricity in particular was found to be a critical parameter in ensuring the SMBH binary coalesced, with all systems that had SMBH coalescence maintaining a high eccentricity ($e \gtrsim 0.7$) for the majority of the three-body interaction phase. High mass resolution simulations typically lost more stellar mass from within a 30 pc shell about the SMBH binary centre of mass shortly after the binary became bound compared to low mass resolution simulations. Increasing the mass resolution was also seen to allow for an increased number of stellar particles able to extract energy from the SMBH binary, as determined through comparison to the watershed velocity of the binary.

For equal mass, equal density simulations (the P+P suite), half of the simulated mergers were able to undergo SMBH coalescence. Using the P+P suite as a reference, the effect of varying physical initial conditions was explored. It was found that unequal mass merger simulations were unable to result in SMBH coalescence, irrespective of the stellar density profile of the progenitors. Conversely, equal mass

mergers of unequal density (the P+J suite) were able to coalesce with ease, owing to the drastically increased number of stellar particles within the near-vicinity of the SMBH binary. The inability of unequal mass mergers to coalesce is at first surprising, particularly as a number of simulations displayed an orbital eccentricity that was consistently high throughout the simulation. It was found that for unequal mass mergers, the incoming stellar velocity of more than three-quarters of the stellar population was greater than the watershed velocity, and thus typically imparted energy to the SMBH binary. As a result, the SMBH binaries in unequal mass mergers were unable to remove the necessary orbital energy and orbital angular momentum to reach the small separations required for efficient emission of GW radiation.

The number of simulations within the study population is not high enough to perform rigorous statistical analysis of SMBH orbital properties, particularly for members of suites with an unequal density merger where only one simulation per mass resolution was performed. An imperative direction for future research is the investigation of the behaviour of the stellar velocity distribution at both very low ($M_\bullet/m_\star < 500$) and very high ($M_\bullet/m_\star > 6000$) mass resolutions. The results from this study indicate a link between the mass resolution and the stellar velocity distribution that is unique to each simulation suite. In physical galaxy mergers where stellar particles are individual stars of $\sim$1.0 $\mathrm{M}_\odot$, the number of stellar particles with an incoming velocity comparable to the watershed velocity is expected to be large enough to efficiently remove orbital energy from the binary. A higher mass resolution is also expected to improve the ability of unequal mass mergers to undergo SMBH coalescence.

A second direction suggested for future investigation is the inclusion of gas in the simulation. The inclusion of gas is required to recreate physically-meaningful models of large early-type galaxies which have a mass of $10^9\,\mathrm{M}_\odot$–$10^{10}\,\mathrm{M}_\odot$, and corresponding SMBH mass of $10^7\,\mathrm{M}_\odot$–$10^8\,\mathrm{M}_\odot$ (following the Magorrian et al. (1998) scaling relation). The SMBH binaries found in the merger of such galaxies are expected to be a prime target of the forthcoming LISA mission, and is thus of high priority. The inclusion of gas is expected to provide additional torques on the stellar particles, and may have a clear effect on the evolution of the SMBH orbital parameters by ensuring the SMBH loss-cone is constantly replenished.

A third direction for future study would be to vary the orbital parameters of the initial merger system. All systems in this study were initialised to follow a radial orbit, whereas in a realistic galactic setting a spectrum of orbital approaches, ranging from dominantly-radial to dominantly-tangential orbits, is expected. Whilst

increasingly tangential approaches are expected to increase the simulation time, the reduced violence of the SMBH passages might see a decrease in the quantity of stellar mass that is removed from the Ketju region following the SMBHs becoming bound. A less-violent stellar mass ejection provides two additional benefits to solving the Final Parsec Problem: more stellar particles with which the SMBH may interact, and a reduced velocity of stellar particles that may allow for more efficient removal of energy from the SMBH binary during the three-body phase.

Finally, the inclusion of SMBH spins in the simulation would allow to accurately model direct SMBH binary collisions, such as the P3+J3 system observed in this study. The strong orbital precession observed for the binary is a crucial element for the occurrence of a significant kick velocity to the coalesced SMBH, that may displace the SMBH from the region of highest stellar density. Whilst not a critical element in the understanding of the Final Parsec Problem, SMBH kick velocities nonetheless present an interesting line for future investigation.

As a result of the observed trend between increasing mass resolution and decreasing scaled incoming stellar velocity, it is concluded that the Final Parsec Problem may be attributed to numerical effects arising from an insufficient mass resolution between the SMBH and the stellar particles. The hardening rate of the SMBH binary was found to be largely independent of the mass resolution. The ability of the binary to interact with stellar particles in the three-body interaction stage, critical for SMBH coalescence, may be adversely affected by the insufficient mass resolution. The three pathways for future investigation discussed are essential for exploring the full nature of the Final Parsec Problem in early-type galaxies. Additionally, SMBH kick velocities may be further investigated for modelling of direct collision systems. The benefits offered by a regularised code, such as KETJU, have proven numerical simulations to be an indispensable tool in investigating the formation and evolution of galaxies and their supermassive black holes.

Bibliography

Aarseth S. J., 2003, Gravitational N-Body Simulations. Cambridge University Press, The Edinburgh Building Building, Cambridge CB2 8RU, UK

Abbott B. P., et al., 2016, Physical Review Letters, 116, 061102

Alabi A. B., et al., 2015, Monthly Notices of the Royal Astronomical Society, 452, 2208

Alabi A. B., et al., 2017, Monthly Notices of the Royal Astronomical Society, 468, 3949

Amaro-Seoane P., et al., 2017, arXiv e-prints, p. arXiv:1702.00786

Annibali F., Bressan A., Rampazzo R., Zeilinger W. W., Vega O., Panuzzo P., 2010, Astronomy and Astrophysics, 519, A40

Arzoumanian Z., et al., 2020, arXiv e-prints, p. arXiv:2009.04496

Baldry I. K., et al., 2018, Monthly Notices of the Royal Astronomical Society, 474, 3875

Barnes J. E., 1988, The Astrophysical Journal, 331, 699

Barnes J., Hut P., 1986, Nature, 324, 446

Begelman M. C., Blandford R. D., Rees M. J., 1980, Nature, 287, 307

Begelman M. C., Volonteri M., Rees M. J., 2006, Monthly Notices of the Royal Astronomical Society, 370, 289

Bellstedt S., Graham A. W., Forbes D. A., Romanowsky A. J., Brodie J. P., Strader J., 2017, Monthly Notices of the Royal Astronomical Society, 470, 1321

Bender R., 1988, Astronomy and Astrophysics, 202, L5

Bender R., Möllenhoff C., 1987, Astronomy and Astrophysics, 177, 71

Bendo G. J., Barnes J. E., 2000, Monthly Notices of the Royal Astronomical Society, 316, 315

Berczik P., Merritt D., Spurzem R., Bischof H.-P., 2006, The Astrophysical Journal Letters, 642, L21

Berentzen I., Preto M., Berczik P., Merritt D., Spurzem R., 2009, The Astrophysical Journal, 695, 455

Bernardi M., et al., 2003, The Astronomical Journal, 125, 1882

Bernardi M., Meert A., Vikram V., Huertas-Company M., Mei S., Shankar F., Sheth R. K., 2012, arXiv e-prints, p. arXiv:1211.6122

Bertola F., Capaccioli M., 1975, The Astrophysical Journal, 200, 439

Binney J., Tremaine S., 2008, Galactic Dynamics: Second Edition. Princeton University Press, 41 William Street, Princeton, NJ 08540, USA

Bois M., et al., 2011, Monthly Notices of the Royal Astronomical Society, 416, 1654

Bortolas E., Gualandris A., Dotti M., Spera M., Mapelli M., 2016, Monthly Notices of the Royal Astronomical Society, 461, 1023

Bryant J. J., et al., 2015, Monthly Notices of the Royal Astronomical Society, 447, 2857

Bulirsch R., Stoer J., 1966, Numerische Mathematik, 8, 1

Burke-Spolaor S., et al., 2019, Astronomy and Astrophysics Reviews, 27, 5

Cappellari M., Copin Y., 2003, Monthly Notices of the Royal Astronomical Society, 342, 345

Cappellari M., et al., 2011, Monthly Notices of the Royal Astronomical Society, 416, 1680

Carmeli M., Hartnett J. G., Oliveira F. J., 2006, Foundations of Physics Letters, 19, 277

Carroll S. M., 2004, Spacetime and geometry. An introduction to general relativity. Cambridge University Press, The Edinburgh Building Building, Cambridge CB2 8RU, UK

Carroll B., Ostlie D., 2017, An Introduction to Modern Astrophysics, 2 edn. Cambridge University Press, Shaftesbury Road, Cambridge CB2 8BS, UK

Chandrasekhar S., 1943, Reviews of Modern Physics, 15, 1

Cordes J. M., Kramer M., Lazio T. J. W., Stappers B. W., Backer D. C., Johnston S., 2004, New Astronomy Review, 48, 1413

Cuadra J., Armitage P. J., Alexander R. D., Begelman M. C., 2009, Monthly Notices of the Royal Astronomical Society, 393, 1423

Davies R. L., Efstathiou G., Fall S. M., Illingworth G., Schechter P. L., 1983, The Astrophysical Journal, 266, 41

Dehnen W., 1993, Monthly Notices of the Royal Astronomical Society, 265, 250

Detweiler S., 1979, The Astrophysical Journal, 234, 1100

Di Matteo T., Colberg J., Springel V., Hernquist L., Sijacki D., 2008, The Astrophysical Journal, 676, 33

Dolag K., Komatsu E., Sunyaev R., 2016, Monthly Notices of the Royal Astronomical Society, 463, 1797

Dressler A., 1980, The Astrophysical Journal, 236, 351

Dressler A., Lynden-Bell D., Burstein D., Davies R. L., Faber S. M., Terlevich R., Wegner G., 1987, The Astrophysical Journal, 313, 42

Edwards R. T., Hobbs G. B., Manchester R. N., 2006, Monthly Notices of the Royal Astronomical Society, 372, 1549

Emsellem E., et al., 2007, Monthly Notices of the Royal Astronomical Society, 379, 401

Emsellem E., et al., 2011, Monthly Notices of the Royal Astronomical Society, 414, 888

Erickson L. K., Gottesman S. T., Hunter J. H. J., 1987, Nature, 325, 779

Escala A., Larson R. B., Coppi P. S., Mardones D., 2004, The Astrophysical Journal, 607, 765

Faber S. M., Jackson R. E., 1976, The Astrophysical Journal, 204, 668

Ferrarese L., Merritt D., 2000, The Astrophysical Journal Letters, 539, L9

Ferrarese L., van den Bosch F. C., Ford H. C., Jaffe W., O'Connell R. W., 1994, The Astronomical Journal, 108, 1598

Forman W., Jones C., Tucker W., 1985, The Astrophysical Journal, 293, 102

Foster C., Arnold J. A., Forbes D. A., Pastorello N., Romanowsky A. J., Spitler L. R., Strader J., Brodie J. P., 2013, Monthly Notices of the Royal Astronomical Society, 435, 3587

Frigo M., Naab T., Hirschmann M., Choi E., Somerville R. S., Krajnovic D., Davé R., Cappellari M., 2019, Monthly Notices of the Royal Astronomical Society, 489, 2702

Gebhardt K., Thomas J., 2009, The Astrophysical Journal, 700, 1690

Gebhardt K., et al., 1996, The Astronomical Journal, 112, 105

Gebhardt K., et al., 2000, The Astrophysical Journal, 539, L13

Genzel R., Eckart A., Ott T., Eisenhauer F., 1997, Monthly Notices of the Royal Astronomical Society, 291, 219

Gerhard O. E., 1993, Monthly Notices of the Royal Astronomical Society, 265, 213

Gerhard O., Jeske G., Saglia R. P., Bender R., 1998, Monthly Notices of the Royal Astronomical Society, 295, 197

Ghez A. M., Klein B. L., Morris M., Becklin E. E., 1998, The Astrophysical Journal, 509, 678

Goulding A. D., Pardo K., Greene J. E., Mingarelli C. M. F., Nyland K., Strauss M. A., 2019, The Astrophysical Journal Letters, 879, L21

Gragg W. B., 1965, SIAM Journal on Numerical Analysis, 2, 384

Graham A. W., 2019, Monthly Notices of the Royal Astronomical Society, 487, 4995

Graham A. W., Onken C. A., Athanassoula E., Combes F., 2011, Monthly Notices of the Royal Astronomical Society, 412, 2211

Gualandris A., Read J. I., Dehnen W., Bortolas E., 2017, Monthly Notices of the Royal Astronomical Society, 464, 2301

Harary F., 1969, Graph theory. Addison-Wesley, Reading, MA, USA

Häring N., Rix H.-W., 2004, The Astrophysical Journal Letters, 604, L89

Herrmann F., Hinder I., Shoemaker D., Laguna P., Matzner R. A., 2007, The Astrophysical Journal, 661, 430

Hills J. G., Fullerton L. W., 1980, The Astronomical Journal, 85, 1281

Hilz M., Naab T., Ostriker J. P., Thomas J., Burkert A., Jesseit R., 2012, Monthly Notices of the Royal Astronomical Society, 425, 3119

Hubble E. P., 1926, The Astrophysical Journal, 64, 321

Hubble E. P., 1936, Realm of the Nebulae. Yale University Press, 100 Maple Ridge Drive, Cumberland, RI 02864-1769, USA

Hubble E., Humason M. L., 1931, The Astrophysical Journal, 74, 43

Humphrey P. J., Buote D. A., 2010, Monthly Notices of the Royal Astronomical Society, 403, 2143

Jeans J. H., 1928, Astronomy and cosmogony. Cambridge University Press, The Edinburgh Building Building, Cambridge CB2 8RU, UK

Jenet F. A., Hobbs G. B., Lee K. J., Manchester R. N., 2005, The Astrophysical Journal Letters, 625, L123

Johansson P. H., Naab T., Burkert A., 2009a, The Astrophysical Journal, 690, 802

Johansson P. H., Burkert A., Naab T., 2009b, The Astrophysical Journal Letters, 707, L184

Kapteyn J. C., 1922, The Astrophysical Journal, 55, 302

Khan F. M., Just A., Merritt D., 2011, The Astrophysical Journal, 732, 89

Khan F. M., Preto M., Berczik P., Berentzen I., Just A., Spurzem R., 2012, The Astrophysical Journal, 749, 147

Khan F. M., Fiacconi D., Mayer L., Berczik P., Just A., 2016, The Astrophysical Journal, 828, 73

Khochfar S., Burkert A., 2006, Astronomy and Astrophysics, 445, 403

Kidder L. E., 1995, Physical Review, 52, 821

Koleva M., Prugniel P., De Rijcke S., Zeilinger W. W., 2011, Monthly Notices of the Royal Astronomical Society, 417, 1643

Kormendy J., 1980, in Crane P., Kjär K., eds, Two Dimensional Photometry. p. 191

Kormendy J., 1982, Saas-Fee Advanced Course, 12, 115

Kormendy J., 1988, The Astrophysical Journal, 325, 128

Kormendy J., Bender R., 1996, The Astrophysical Journal Letters, 464, L119

Kormendy J., Djorgovski S., 1989, Annual Review of Astronomy and Astrophysics, 27, 235

Kormendy J., Ho L. C., 2013, Annual Review of Astronomy and Astrophysics, 51, 511

Kormendy J., Richstone D., 1995, Annual Review of Astronomy and Astrophysics, 33, 581

Krajnović D., et al., 2011, Monthly Notices of the Royal Astronomical Society, 414, 2923

Kravtsov A. V., 2013, The Astrophysical Journal Letters, 764, L31

Kulier A., Ostriker J. P., Natarajan P., Lackner C. N., Cen R., 2015, The Astrophysical Journal, 799, 178

Lahén N., Johansson P. H., Rantala A., Naab T., Frigo M., 2018, Monthly Notices of the Royal Astronomical Society, 475, 3934

Lintott C. J., et al., 2008, Monthly Notices of the Royal Astronomical Society, 389, 1179

Magorrian J., et al., 1998, The Astronomical Journal, 115, 2285

Makino J., Funato Y., 2004, The Astrophysical Journal, 602, 93

Mannerkoski M., Johansson P. H., Pihajoki P., Rantala A., Naab T., 2019, The Astrophysical Journal, 887, 35

Marconi A., Hunt L. K., 2003, The Astrophysical Journal Letters, 589, L21

Mármol-Queraltó E., et al., 2009, The Astrophysical Journal Letters, 705, L199

Mathews W. G., 1978, The Astrophysical Journal, 219, 413

Mayer L., 2013, Classical and Quantum Gravity, 30, 244008

Mayer L., Kazantzidis S., Madau P., Colpi M., Quinn T., Wadsley J., 2007, Science, 316, 1874

McConnell N. J., Ma C.-P., 2013, The Astrophysical Journal, 764, 184

Merritt D., 1985, The Astrophysical Journal, 90, 1027

Merritt D., 2001, The Astrophysical Journal, 556, 245

Merritt D., 2006, The Astrophysical Journal, 648, 976

Merritt D., 2013, Dynamics and Evolution of Galactic Nuclei. Princeton University Press, 41 William Street, Princeton, NJ 08540, USA

Merritt D., Poon M. Y., 2004, The Astrophysical Journal, 606, 788

Mikkola S., Aarseth S., 2002, Celestial Mechanics and Dynamical Astronomy, 84, 343

Mikkola S., Merritt D., 2006, Monthly Notices of the Royal Astronomical Society, 372, 219

Mikkola S., Merritt D., 2008, The Astronomical Journal, 135, 2398

Mikkola S., Tanikawa K., 1999, Monthly Notices of the Royal Astronomical Society, 310, 745

Mikkola S., Valtonen M. J., 1992, Monthly Notices of the Royal Astronomical Society, 259, 115

Milosavljević M., Merritt D., 2001, The Astrophysical Journal, 563, 34

Milosavljević M., Merritt D., 2003, in Centrella J. M., ed., American Institute of Physics Conference Series Vol. 686, The Astrophysics of Gravitational Wave Sources. pp 201–210 (arXiv:astro-ph/0212270), doi:10.1063/1.1629432

Misgeld I., Hilker M., 2011, Monthly Notices of the Royal Astronomical Society, 414, 3699

Mo H., van den Bosch F. C., White S., 2010, Galaxy Formation and Evolution. Cambridge University Press, The Edinburgh Building Building, Cambridge CB2 8RU, UK

Monaghan J. J., Lattanzio J. C., 1985, Astronomy and Astrophysics, 149, 135

Moore C. J., Cole R. H., Berry C. P. L., 2015, Classical and Quantum Gravity, 32, 015014

Mora T., Will C. M., 2004, Physical Review, 69, 104021

Mosleh M., Williams R. J., Franx M., 2013, The Astrophysical Journal, 777, 117

Moster B. P., Somerville R. S., Maulbetsch C., van den Bosch F. C., Macciò A. V., Naab T., Oser L., 2010, The Astrophysical Journal, 710, 903

Mulder W. A., 1983, Astronomy and Astrophysics, 117, 9

Naab T., Burkert A., 2003, The Astrophysical Journal, 597, 893

Naab T., Burkert A., Hernquist L., 1999, The Astrophysical Journal Letters, 523, L133

Naab T., Khochfar S., Burkert A., 2006, The Astrophysical Journal Letters, 636, L81

Nasim I., Gualandris A., Read J., Dehnen W., Delorme M., Antonini F., 2020, Monthly Notices of the Royal Astronomical Society, 497, 739

O'Sullivan E., Vrtilek J. M., Kempner J. C., David L. P., Houck J. C., 2005, Monthly Notices of the Royal Astronomical Society, 357, 1134

Oser L., Naab T., Ostriker J. P., Johansson P. H., 2012, The Astrophysical Journal, 744, 63

Pahre M. A., Djorgovski S. G., de Carvalho R. R., 1998, The Astronomical Journal, 116, 1591

Peletier R. F., Davies R. L., Illingworth G. D., Davis L. E., Cawson M., 1990, The Astronomical Journal, 100, 1091

Peters P. C., 1964, Physical Review, 136, 1224

Peters P. C., Mathews J., 1963, Physical Review, 131, 435

Planck Collaboration et al., 2018, arXiv e-prints, p. arXiv:1807.06209

Poisson E., Will C. M., 2014, Gravity. Cambridge University Press, The Edinburgh Building Building, Cambridge CB2 8RU, UK

Press W. H., Teukolsky S. A., Vetterling W. T., Flannery B. P., 2007, Numerical Recipes 3rd Edition: The Art of Scientific Computing, 3 edn. Cambridge University Press, The Edinburgh Building Building, Cambridge CB2 8RU, UK

Prim R. C., 1957, Bell System Technical Journal, 36, 1389

Quinlan G. D., 1996, New Astronomy, 1, 35

Quinn T., Katz N., Stadel J., Lake G., 1997, arXiv e-prints, pp astro–ph/9710043

Rantala A., Pihajoki P., Johansson P. H., Naab T., Lahén N., Sawala T., 2017, The Astrophysical Journal, 840, 53

Rantala A., Johansson P. H., Naab T., Thomas J., Frigo M., 2018, The Astrophysical Journal, 864, 113

Rantala A., Johansson P. H., Naab T., Thomas J., Frigo M., 2019, The Astrophysical Journal Letters, 872, L17

Rantala A., Pihajoki P., Mannerkoski M., Johansson P. H., Naab T., 2020, Monthly Notices of the Royal Astronomical Society, 492, 4131

Rawlings A., et al., 2020, Monthly Notices of the Royal Astronomical Society, 491, 324

Regan J. A., Visbal E., Wise J. H., Haiman Z., Johansson P. H., Bryan G. L., 2017, Nature Astronomy, 1, 0075

Remus R.-S., Dolag K., Naab T., Burkert A., Hirschmann M., Hoffmann T. L., Johansson P. H., 2017, Monthly Notices of the Royal Astronomical Society, 464, 3742

Roberts M. S., Haynes M. P., 1994, Annual Review of Astronomy and Astrophysics, 32, 115

Robson T., Cornish N. J., Liu C., 2019, Classical and Quantum Gravity, 36, 105011

Rubin V. C., Ford W. Kent J., 1970, The Astrophysical Journal, 159, 379

Ryu T., Perna R., Haiman Z., Ostriker J. P., Stone N. C., 2018, Monthly Notices of the Royal Astronomical Society, 473, 3410

Samir R. M., Reda F. M., Shaker A. A., Osman A. M. I., Amin M. Y., 2016, NRIAG Journal of Astronomy and Geophysics, 5, 277

Sandage A., Visvanathan N., 1978, The Astrophysical Journal, 223, 707

Sazhin M. V., 1978, Soviet Astronomy, 22, 36

Schombert J. M., 1986, The Astrophysical Journal Supplement Series, 60, 603

Scorza C., Bender R., 1995, Astronomy and Astrophysics, 293, 20

Sérsic J. L., 1963, Boletin de la Asociacion Argentina de Astronomia La Plata Argentina, 6, 41

Sesana A., 2010, The Astrophysical Journal, 719, 851

Sesana A., Vecchio A., Colacino C. N., 2008, Monthly Notices of the Royal Astronomical Society, 390, 192

Sesana A., Gualandris A., Dotti M., 2011, Monthly Notices of the Royal Astronomical Society, 415, L35

Shen S., Mo H. J., White S. D. M., Blanton M. R., Kauffmann G., Voges W., Brinkmann J., Csabai I., 2003, Monthly Notices of the Royal Astronomical Society, 343, 978

Springel V., 2005, Monthly Notices of the Royal Astronomical Society, 364, 1105

Springel V., 2016, Saas-Fee Advanced Course, 43, 251

Springel V., Hernquist L., 2003, Monthly Notices of the Royal Astronomical Society, 339, 289

Springel V., Yoshida N., White S. D. M., 2001, New Astronomy, 6, 79

Suess K. A., Kriek M., Price S. H., Barro G., 2019, The Astrophysical Journal, 877, 103

Teyssier R., 2002, Astronomy and Astrophysics, 385, 337

Theis C., 1998, Astronomy and Astrophysics, 330, 1180

Thomas J., Saglia R. P., Bender R., Thomas D., Gebhardt K., Magorrian J., Corsini E. M., Wegner G., 2007, Monthly Notices of the Royal Astronomical Society, 382, 657

Thomas J., Ma C.-P., McConnell N. J., Greene J. E., Blakeslee J. P., Janish R., 2016, Nature, 532, 340

Tortora C., La Barbera F., Napolitano N. R., Romanowsky A. J., Ferreras I., de Carvalho R. R., 2014, Monthly Notices of the Royal Astronomical Society, 445, 115

Tremaine S., et al., 2002, The Astrophysical Journal, 574, 740

Valtonen M., Mikkola S., 1991, Annual Review of Astronomy and Astrophysics, 29, 9

Vasiliev E., Antonini F., Merritt D., 2014, The Astrophysical Journal, 785, 163

Vasiliev E., Antonini F., Merritt D., 2015, The Astrophysical Journal, 810, 49

Wang L., Spurzem R., Aarseth S., Nitadori K., Berczik P., Kouwenhoven M. B. N., Naab T., 2015, Monthly Notices of the Royal Astronomical Society, 450, 4070

White S. D. M., 1976, Monthly Notices of the Royal Astronomical Society, 174, 19

Xu C. K., Zhao Y., Scoville N., Capak P., Drory N., Gao Y., 2012, The Astrophysical Journal, 747, 85

Yang X., Mo H. J., van den Bosch F. C., 2003, Monthly Notices of the Royal Astronomical Society, 339, 1057

Yu Q., 2002, Monthly Notices of the Royal Astronomical Society, 331, 935

Zwicky F., 1933, Helvetica Physica Acta, 6, 110

de Vaucouleurs G., 1948, Annales d'Astrophysique, 11, 247

de Vaucouleurs G., 1959, Handbuch der Physik, 53, 275

dell'Antonio I. P., Geller M. J., Fabricant D. G., 1995, The Astronomical Journal, 110, 502

van de Sande J., et al., 2017, The Astrophysical Journal, 835, 104

van der Marel R. P., 1994, Monthly Notices of the Royal Astronomical Society, 270, 271

van der Marel R. P., Franx M., 1993, The Astrophysical Journal, 407, 525

A. Supplementary Figures

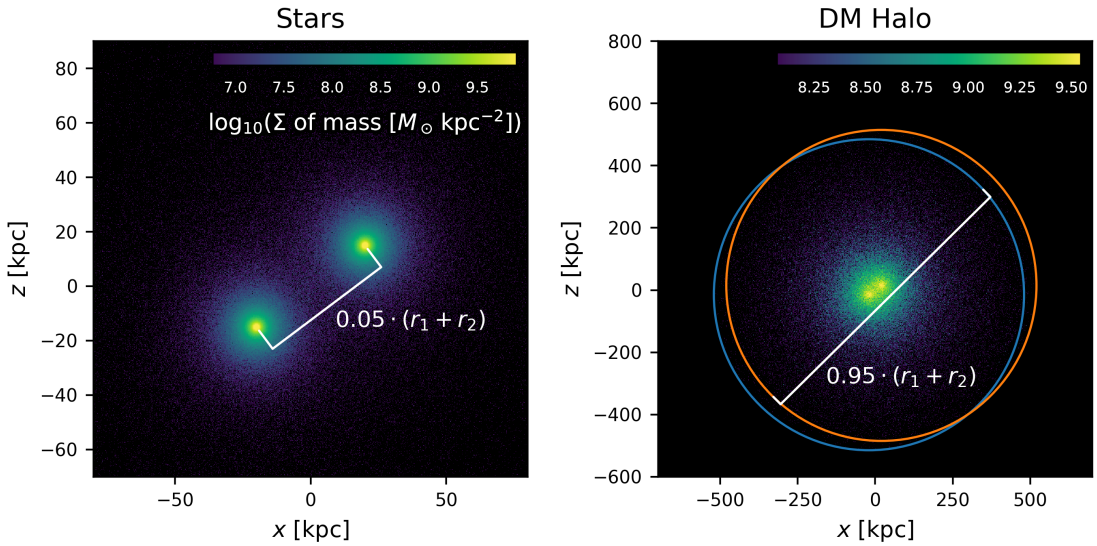

Figure A.1: Initial orbital configuration of the simulations (here shown is the P+P configuration). The maximum radius of each progenitor galaxy is labelled r_1 and r_2 respectively. *Left:* SMBHs are separated by a distance $0.05 \cdot (r_1 + r_2)$, corresponding to 50 kpc for equal mass systems and 75 kpc for unequal mass systems. Minimal overlap of the stellar structure is present. *Right:* The DM halos of the progenitor galaxies (extent given by the coloured ring) are separated by $0.95 \cdot (r_1 + r_2)$, and demonstrate significant overlap. As discussed in §4.7, overlapping DM halos do not significantly decrease the mean nearest-neighbour distance of DM particles.

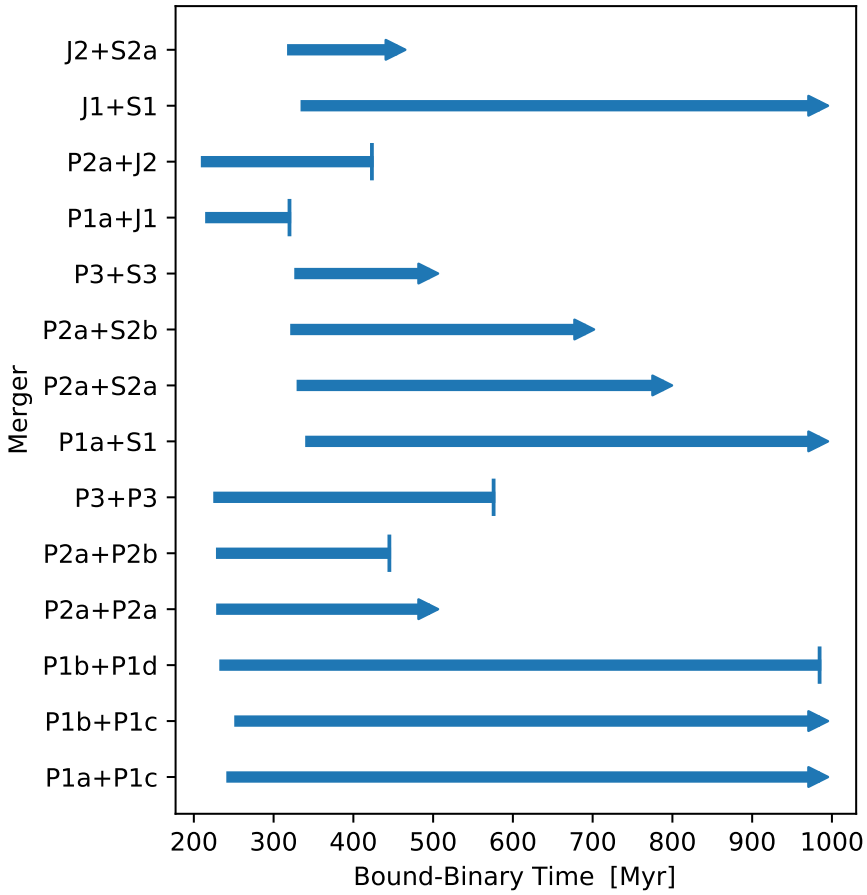

Figure A.2: Relation between the physical time and the time from which the SMBH binaries became bound. Those binaries which coalesced have a line terminating in a vertical bar, and those binaries which did not coalesce have a line terminating with an arrowhead.

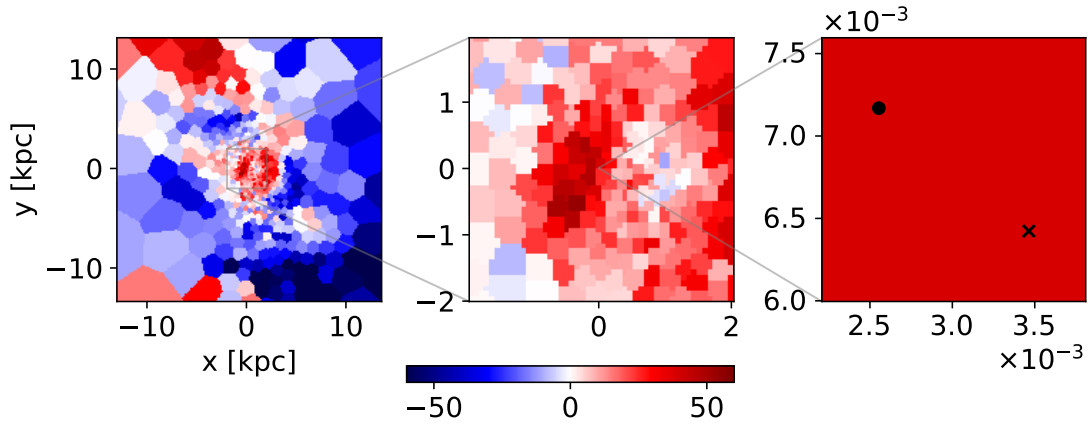

Figure A.3: Mean velocity map of the P3+P3 simulation at $t = 245\,\mathrm{Myr}$, corresponding to 14 Myr after the SMBH binary became bound. The counter-rotating stellar structure in the central region is shown in the left panel, and is zoomed in to the SMBH binary in the right panel. SMBH binary velocity is indicated by a '×' for $v_z > 0\,\mathrm{km\,s^{-1}}$, and a '•' for $v_z < 0\,\mathrm{km\,s^{-1}}$. The KDC is hypothesised to cause an initial increase in the binary eccentricity following the system becoming bound.

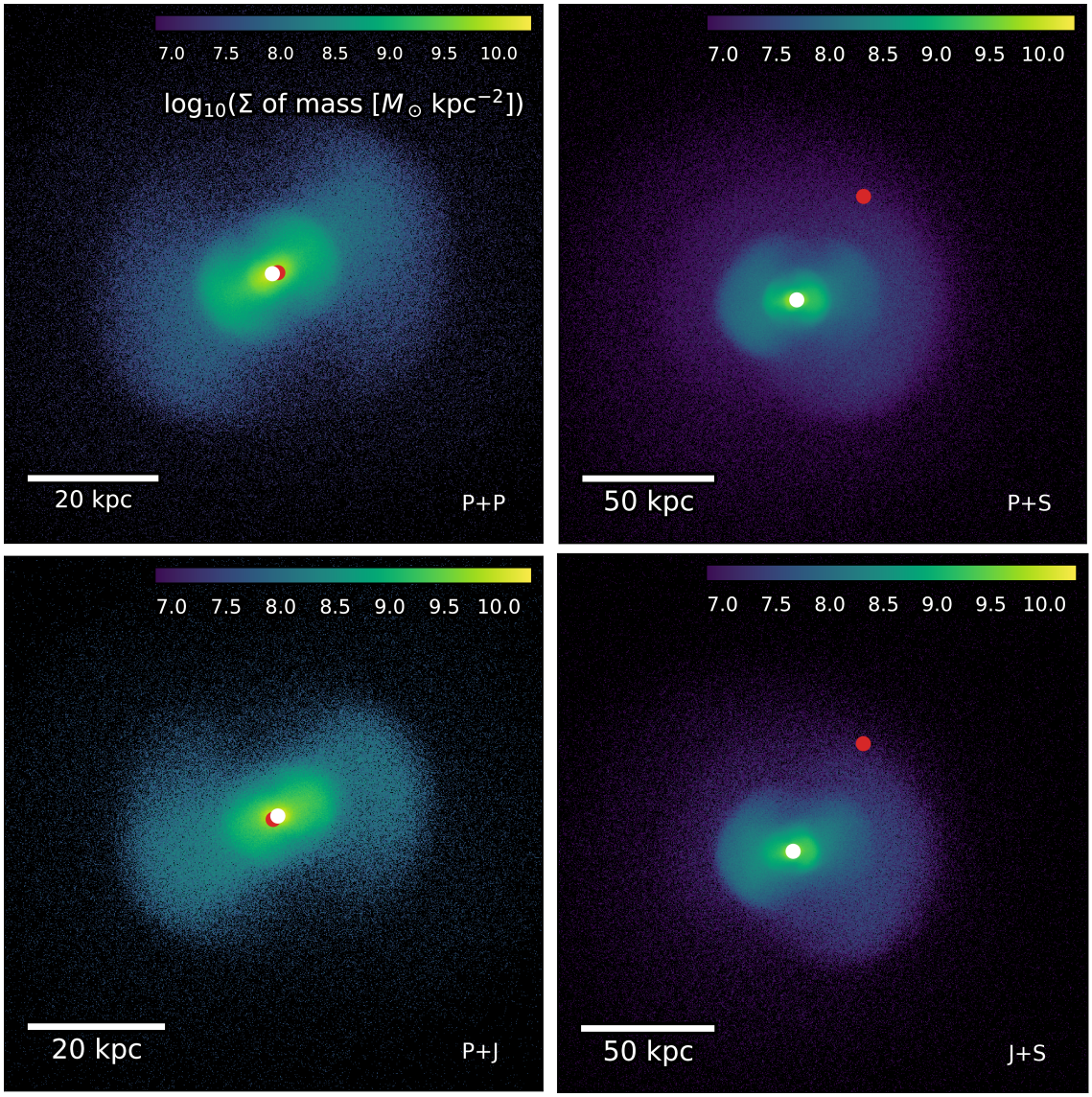

Figure A.4: Centre of mass as determined by all simulation particles (red point) and solely the SMBH binary (white point) superimposed on the stellar mass surface density. For unequal mass mergers, the centre of mass as determined by all particles lies far from the region of the highest stellar density, indicating that outlying DM particles have skewed the centre of mass calculation. Consequently, for all calculations performed, the centre of mass of the SMBH binary is used. The mass scaling is consistent between all plots, but note the differing distance scales between the columns of the figure. *Top left:* The P3+P3 system at 236 Myr. *Top right:* The P3+S3 system at 340 Myr. *Bottom left:* The P2a+J2 system at 220 Myr. *Bottom right:* The J2+S2a system at 331 Myr.

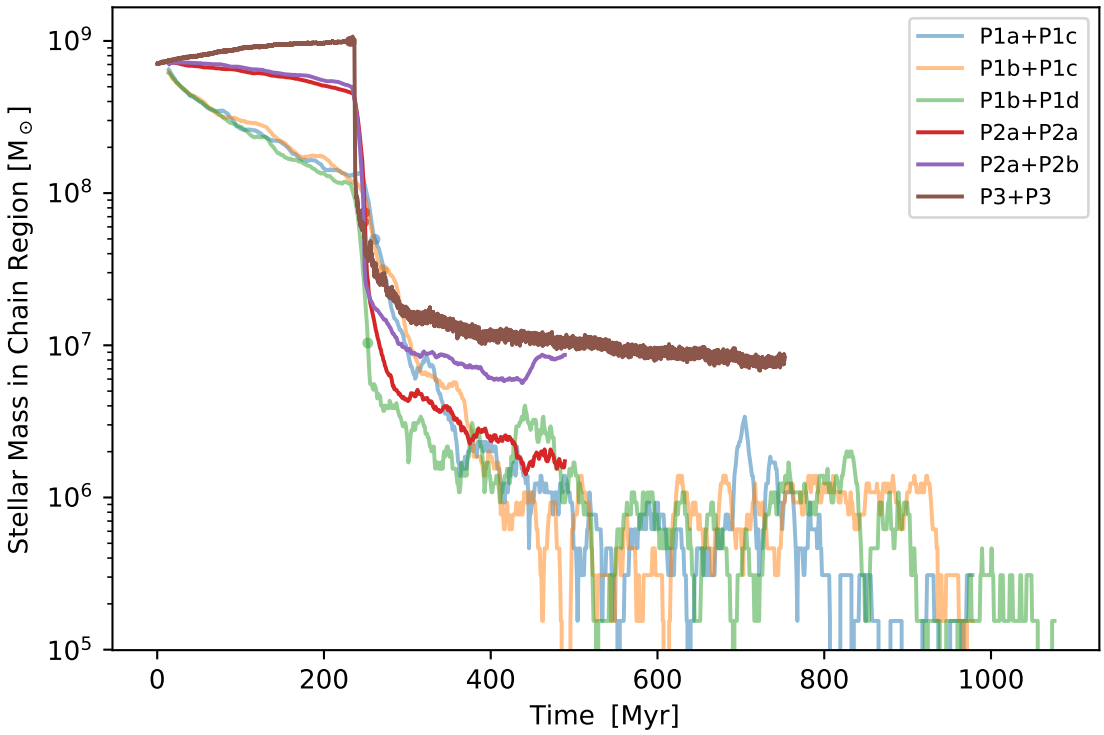

Figure A.5: Stellar mass within the Ketju region for the P+P simulation suite. Low resolution simulations are faded for clarity. The sudden evacuation of mass from the Ketju region approximately coincides with the time the SMBH binary becomes bound. Low resolution simulations typically fluctuate more than the medium and high resolution simulations. Increasing mass resolution is seen to increase the amount of stellar mass lost from the Ketju region.

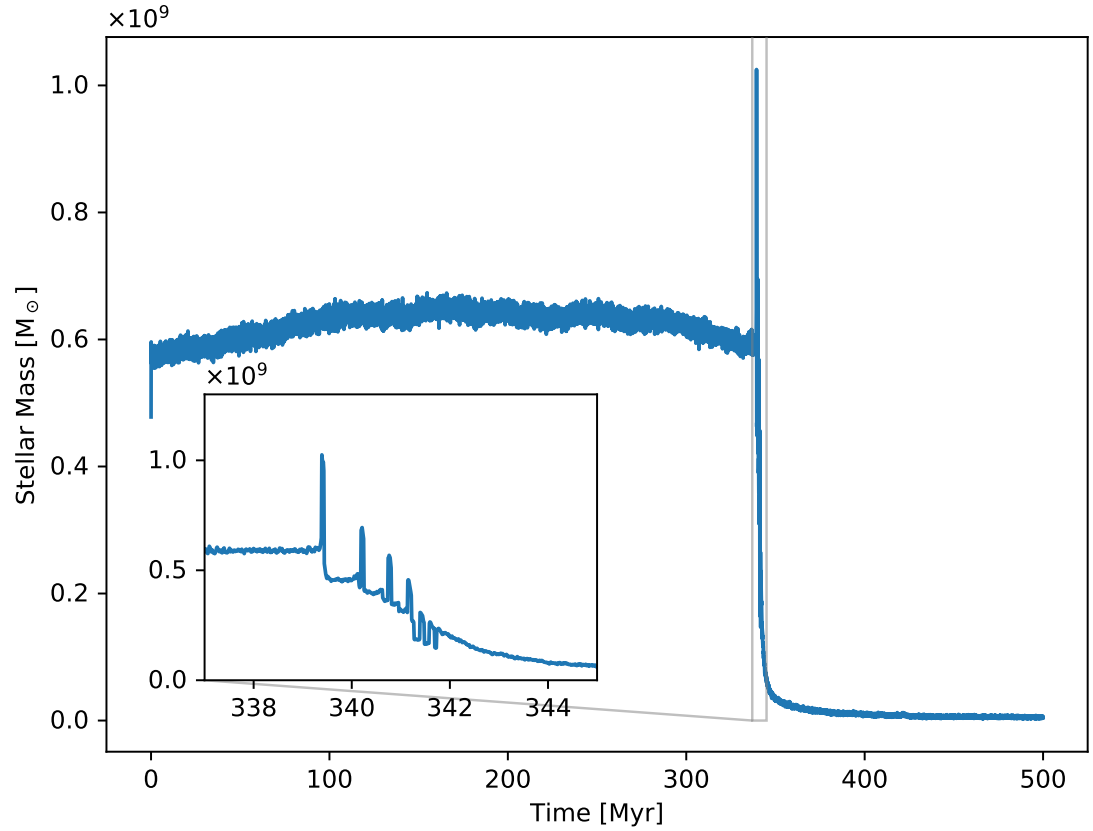

Figure A.6: Stellar mass within the Ketju region for the P3+S3 simulation, with focus on the period of the sudden drop in stellar mass. Critically, a series of local peaks is seen to occur during the overall sudden decrease in stellar mass. The peaks can be understood as evidence for the 'sloshing' of stellar mass within the central region as the merging galactic systems relax to an equilibrium state.

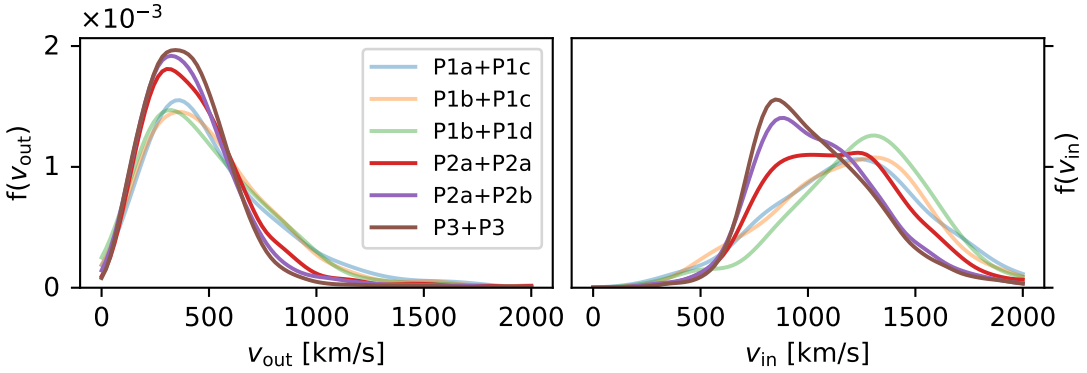

Figure A.7: Unscaled stellar velocities crossing a 30 pc shell about the SMBH binary in the P+P simulation suite. *Left:* The velocity distribution of the outgoing stellar mass. *Right:* The velocity distribution of the incoming stellar mass. Both distributions are shown on equal scales. Low resolution simulations typically enter the shell at a higher velocity than medium and high resolution simulations

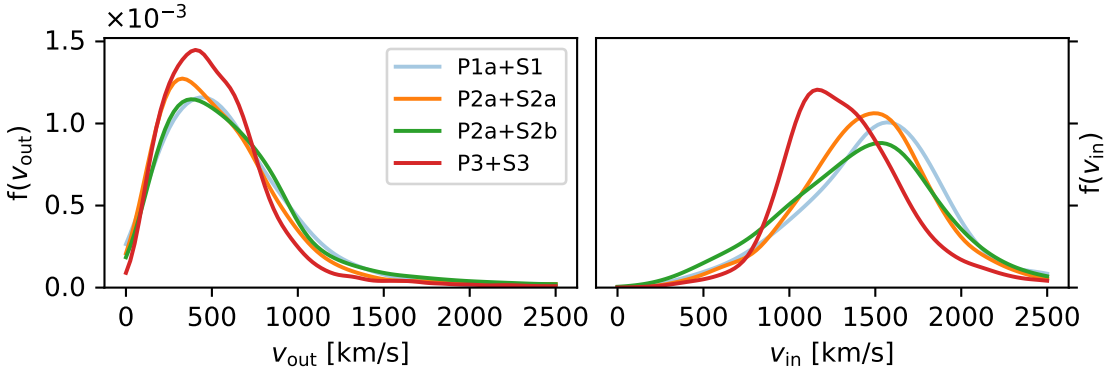

Figure A.8: Same as Fig. A.7, but for the P+S simulation suite. Note the differing scales.

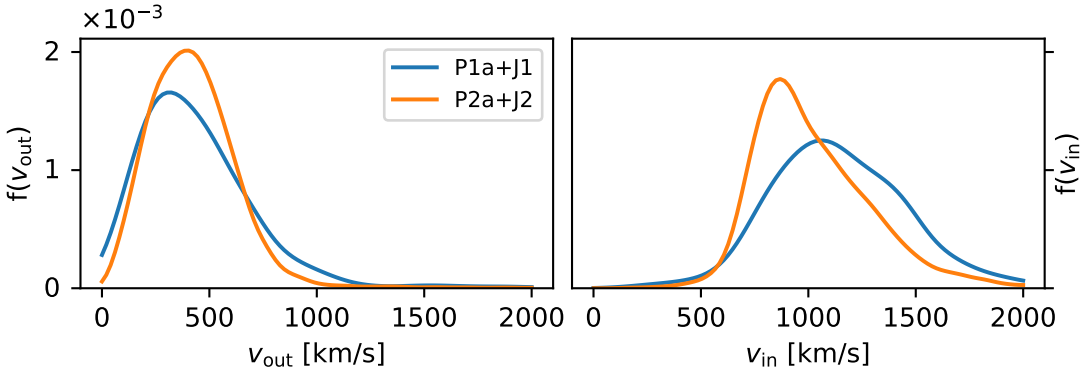

Figure A.9: Same as Fig. A.7, but for the P+J simulation suite. Note the differing scales.

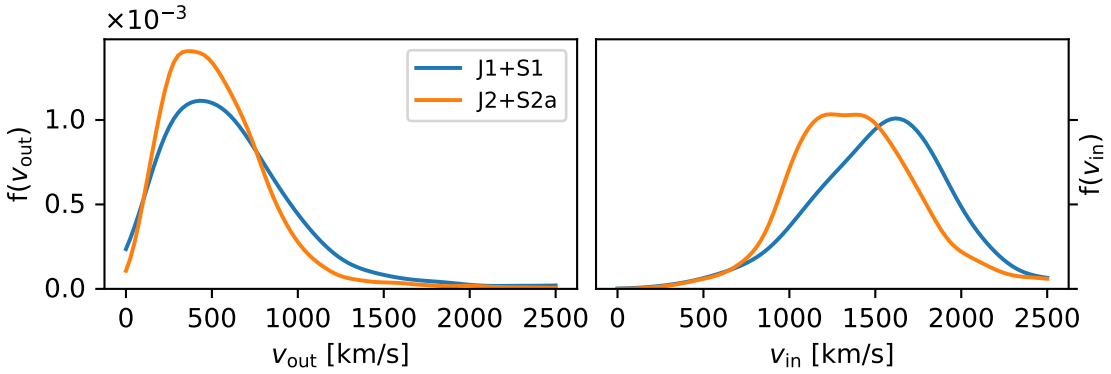

Figure A.10: Same as Fig. A.7, but for the J+S simulation suite. Note the differing scales.

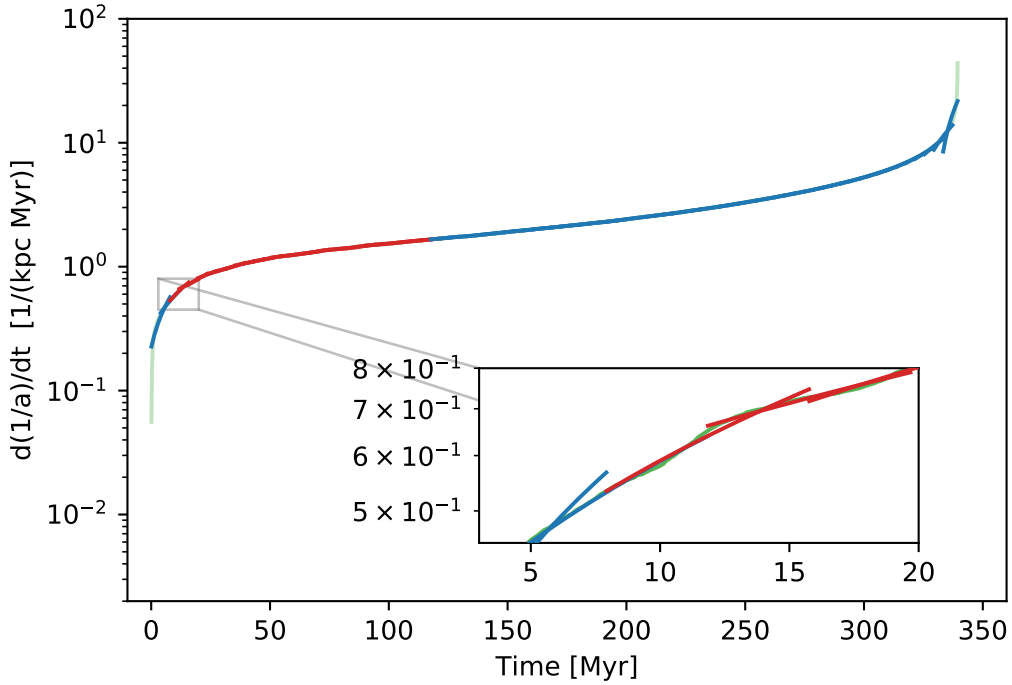

Figure A.11: Example plot demonstrating the selection of line segments used for determining the hardening rate of each simulation. Those segments which are used in calculating the hardening rate are shown in red, and those which are not used are shown in blue. The selection criteria are described in the text (see §5.6). The green line in the inset figure indicates the data to which the linear regression is fit.